

3083
TR 3085

3083
TR 3085

FREQUENCY-DEPENDENT WAVE
PROPAGATION
IN WATER-SATURATED POROUS MEDIA

**FREQUENCY-DEPENDENT WAVE
PROPAGATION
IN WATER-SATURATED POROUS MEDIA**

PROEFSCHRIFT

ter verkrijging van de graad van doctor
aan de Technische Universiteit Delft,
op gezag van de Rector Magnificus,
Prof.ir. K.F. Wakker,
in het openbaar te verdedigen ten overstaan van een commissie,
door het College voor Promoties aangewezen,
op maandag 9 februari 1998 te 13.30 uur

door

Oscar KELDER

mijnningenieur

geboren te Uerkheim (Zwitserland)

Dit proefschrift is goedgekeurd door de promotor:

Prof.ir. M. Peeters

Samenstelling promotiecommissie:

Rector Magnificus, voorzitter

Prof.ir. M. Peeters, Technische Universiteit Delft, promotor

Prof.dr.ir. M.E.H. van Dongen, Universiteit Twente

Prof.dr.ir. A. Verruijt, Technische Universiteit Delft

Prof.dr.ir. J.T. Fokkema, Technische Universiteit Delft

Prof.dr. P.K. Currie, Technische Universiteit Delft

Dr.rer.nat. B.C. Lehr, Shell, Rijswijk

Dr.ir. D.M.J. Smeulders heeft als begeleider in belangrijke mate aan het totstandkomen van het proefschrift bijgedragen.

Printed by:

Drukkerij Technische Universiteit Delft

English corrector: Hansa Krijgsman

ISBN 90-9011360-6

Copyright © 1997 by O.Kelder, Delft University of Technology

All rights reserved.

No part of the material protected by this copyright notice may be reproduced or utilized in any form or by any means, electronic or mechanical, including photocopying, recording or by any information storage and retrieval system, without permission from the publisher.

Printed in The Netherlands

Aan mijn ouders en Anita.

The experiments described in this thesis were performed at the Dietz Laboratory, Faculty of Applied Earth Sciences, Delft University of Technology, Mijnbouwstraat 120, 2628 RX Delft, The Netherlands.

This research was funded by Delft University of Technology, Grant No. DMB33.3070 from The Netherlands Technology Foundation (STW), Shell IEP RTS Rijswijk, and Western Atlas. This support is gratefully acknowledged.

Contents

Abstract	10
1 Introduction	12
1.1 Background	12
1.2 Problem statement	13
1.3 Literature survey	15
1.4 Approach and thesis outline	19
2 Basic field equations for fluid-saturated porous media	22
2.1 Introduction	22
2.2 Mechanical description of a porous medium	23
2.3 Continuity and constitutive relations	26
2.3.1 ‘Gedanken’ experiments	27
2.3.2 Relations to measurable quantities	30
2.4 Momentum equations	32
3 Dynamic interaction	36
3.1 Introduction	36
3.2 Dynamic permeability for a fluid-filled rigid porous medium .	37
3.3 Dynamic behaviour for a model porous medium	41
3.4 Acoustics in deformable porous media	46

4	Acoustic bulk properties of fluid-saturated porous media	47
4.1	Introduction	47
4.2	On potentials	47
4.3	Compressional wave velocities	50
4.4	Shear wave velocity	56
4.5	Effect of grain compressibility	57
5	Waves and interfaces	60
5.1	Introduction	60
5.2	Solutions of the field quantities	60
5.3	Reflection and transmission coefficients	64
5.4	Numerical results	67
6	Sample properties and description	73
6.1	Introduction	73
6.2	Description of porous materials	73
6.3	Dynamic permeability	77
6.4	Porosity and grain density	82
6.5	Tortuosity	83
6.6	Steady-state permeability	85
6.7	Elastic properties	86
7	Measurements of acoustic bulk properties	90
7.1	Introduction	90
7.2	Experimental set-up	90
7.3	Water measurements	93
7.4	Microseismograms	94
7.5	Spectral ratio technique	101

7.6	Phase speed and attenuation measurements	104
7.7	Discussion and conclusions	113
8	Conclusions	115
A	De Vries-Geerits approach for non-viscous fluid	117
A.1	Similarity to Biot formulation	122
A.2	Energy considerations	123
	Bibliography	127
	Samenvatting	134
	Dankwoord	137
	Curriculum vitae	139

Abstract

Rock and fluid properties can be derived from acoustic signals generated by surface seismic or wireline tools in boreholes. Direct hydrocarbon indicators receive much attention but they are mainly based on empirical relations between acoustic wave train attributes and rock parameters. This thesis is a contribution to the effort to formulate a more fundamental basis for the derivation of rock and fluid properties from acoustic waves. A two-pronged approach was followed. First, theories on wave propagation in porous media were reviewed and extended, and second, calculations based on these theories were verified independently by means of experiments.

The theoretical work was based on the wave propagation equations developed by Biot (1956, 1962) for homogeneous and isotropic porous material. From straightforward continuity and constitutive equations we showed that the generalized elastic coefficients appearing in the Biot theory can be directly related to porosity and rock and fluid bulk moduli. An alternative derivation of Biot's coupled momentum equations demonstrated that viscous forces are dominant for low frequencies, while inertia forces prevail at high frequencies. The viscous effects are characterized by the steady-state permeability and the inertial effects by the tortuosity parameter. The transition at intermediate frequencies was described by the dynamic permeability model of Johnson et al. (1987). The scaling function for the dynamic permeability of a porous medium only depends on the rollover frequency and a similarity parameter M . By modelling, we demonstrated that under normal conditions M has values close to 1, as originally suggested by Johnson et al.

Solving the Biot equations leads to a shear wave, and a fast and slow compressional wave. The fast wave is characterized by in-phase pore fluid and solid matrix movements, and the slow wave by opposite phase movements. The out-of-phase motion explains the high attenuation of the slow wave. Whereas the phase speed of the slow wave is influenced by the frequency-

dependent dynamic permeability, the phase speed of the fast wave and the shear wave are frequency independent. For the attenuation of all three bulk waves the influence of the dynamic permeability becomes significant at higher frequencies. Evidently, in the lower frequency range the dynamic permeability tends to behave like the steady-state permeability. The grain compressibility effects on the compressional wave velocities in the high frequency limit were investigated. We found that for relevant ratios of grain/matrix moduli, the two compressional wave velocities, normalized by the corresponding velocities for incompressible grains, vary less than 10%. We also determined the frequency-dependent reflection and transmission coefficients of plane waves at oblique incidence on an interface between a fluid and a fluid-saturated porous medium. Clear angular dependence and critical angle phenomena were observed for all three wave types.

For the experimental verification of these statements we used two laboratory set-ups and various artificial and natural porous samples. All input parameters for the theoretical predictions of the experimental results were measured separately on the samples. The first set-up was specifically designed to measure dynamic permeability. In this so-called Dynamic Darcy Cell transmission of low-frequency oscillating pressure gradients (20-200 Hz) was obtained with a vibration exciter on one side and pressure transducers on both sides of a rigidly mounted artificial sample. All results demonstrated that the ratio of dynamic over steady-state permeability can be adequately described by the rollover frequency and a similarity parameter close to 1. In the second set-up, ultrasonic transmission experiments between 0.1 and 1 MHz were carried out with piezo-electric transducers placed on each side of a slab of porous material submerged in water. We found that the Biot theory gave a very accurate description of all three phase-speed measurements both for artificial samples and for samples cut from natural Nivelsteiner and Bentheimer sandstone. Moreover, we measured the Biot slow wave for the first time on a natural rock (Nivelsteiner sandstone). The Biot theory correctly predicted the attenuation of the slow wave in almost all samples but it failed to predict the fast wave and shear wave attenuation. Scattering, micro-cracks, and clay-related damping were assumed to account for the difference between measured attenuation and Biot predictions. We also found that the unconsolidated Nivelsteiner sandstone samples show much higher attenuation values than the consolidated samples. Future work should concentrate on quantifying the non-Biot type attenuation mechanisms, and on the influence of small-scale inhomogeneities and thin-layered media.

Chapter 1

Introduction

1.1 Background

Acoustic signals are used extensively in the oil and gas industry to delineate geological structures down to a few kilometres and to obtain lithology information on sedimentary rocks. They are also used for gathering knowledge of the deeper part of the crust, down to 45 kilometres, which is an important source for earthquake prediction. Acoustic techniques comprise surface seismics, vertical seismic profiling, cross-well tomography, sonic wireline logging, and ultrasonic logging measurements.

All these techniques use a source which emits acoustic waves. These waves propagate through the rock and are subsequently detected by one or more receivers. The detected waves contain information about the rock along the wave path and the objective of all techniques is to extract this information in terms of geological structures and rock properties.

In the past, seismic methods used by the oil industry were mainly applied to delineate structures which might contain hydrocarbons. For this, conventional surface seismic reflection methods make use of sources and detectors placed near or on the surface (operating frequencies between 10 and 100 Hz). Seismic waves travelling down reflect from layer boundaries back to the surface, where they are recorded. From these recorded signals, velocities and depth profiles of the subsurface are extracted by means of dedicated seismic processing techniques. Besides the arrival times of the seismic waves, changes in signal amplitude are also studied. Seismic stratigraphy uses the fact that a given geological sequence corresponds to a given signature on the

seismic signal, which makes it possible to obtain qualitative lithologic data on the various layers. Furthermore, the presence of gas sometimes causes high energy reflections in the form of local amplitude anomalies known as bright spots. Recently, a range of seismic attributes has been used to indicate the presence of hydrocarbons (direct hydrocarbon indicators or DHI's).

Borehole logging techniques are used to obtain more detailed information about potential reservoirs. In vertical seismic profiling (VSP) the source remains located on the surface, but the receiver is placed in a borehole. This configuration allows for higher frequencies to be used (up to 500 Hz). In areas with more than one borehole, the source can be placed in one borehole, and the receiver in the other. This is called cross-well seismology. A maximum frequency of several kHz is feasible. In this way details in the order of 1 to 5 m can be detected, whereas for the surface seismic method the highest resolution is about 20 m.

Finally, the sonic (10-100 kHz) and ultrasonic (up to 10 MHz) borehole logging techniques enable us investigating the reservoir at the pore scale. Conventional acoustic logging measurements started out as a companion to surface seismic measurements. This led to the well-known Wyllie time-average equation to estimate porosity from velocities. Subsequently, newer acoustic devices and improved signal processing techniques provided borehole measurements which allow applications beyond the conventional estimation of porosity. These applications include determination of lithology and fluid type, detection of overpressured zones, fracture density and estimation of formation strength. The ultrasonic devices operating in the MHz ranges have opened the door to acoustic borehole imaging.

1.2 Problem statement

Because of the increasing value of undepleted reservoir rock, remaining oil, and the higher complexity of new oil fields, a major shift in the use of acoustic signals occurred. One of the central aspects of this shift involves the need to establish and understand the relations between the acoustic responses of reservoir rock, and their production and lithological properties, such as porosity, permeability, and saturation. So far, practical interpretation procedures have been based on empirical relationships between the transit time and amplitude of acoustic signals to the various rock properties. To understand the influence of the rock properties on the recorded wavetrain better,

we are not only interested in velocity and amplitude variations but also in the damping of the wave and the frequency-dependent behaviour of the acoustic signal.

To fulfil this requirement, we need a comprehensive theory of frequency-dependent wave propagation in poro-elastic media to offset the higher complexity and sub-seismic size of many newly discovered reservoirs. Moreover, this understanding is expected to contribute to locating the remaining oil in developed reservoirs. In this study we concentrate on the experimental verification of such a theory.

A suitable approach for this verification is found in the scientific model depicted in Figure (1.1). We start by measuring the production and litholog-

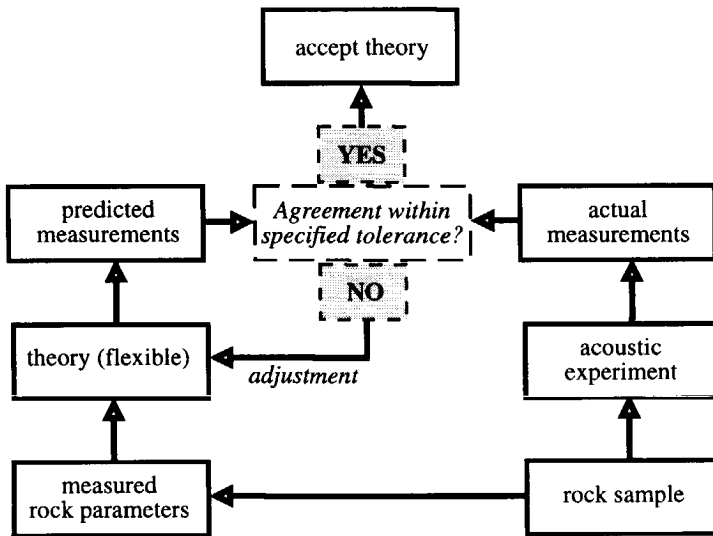


Figure 1.1: *Scientific model*

ical parameters of one specific rock sample separately. Next, we formulate a theory which describes the propagation of acoustic waves in space and time through a medium which is representative of the rock sample. After substituting the rock and fluid parameters in this theory, we can calculate a synthetic seismogram for this specific sample, called the "predicted measurement". Next, we subject this rock sample to an acoustic experiment and compare these "actual measurements" with the predicted measurements. If the difference between these measurements is within a specified tolerance,

the theory is accepted. If not, the theory needs to be adjusted, because both the input parameters and the actual measurements are considered to be correct. In the end, the resulting theoretical model can be used as a fixed part in an inversion process to determine unknown rock parameters. This is beyond the scope of this study, but it is shown in Figure (1.2) for the sake of completeness. In the inversion process the rock parameters are adjusted

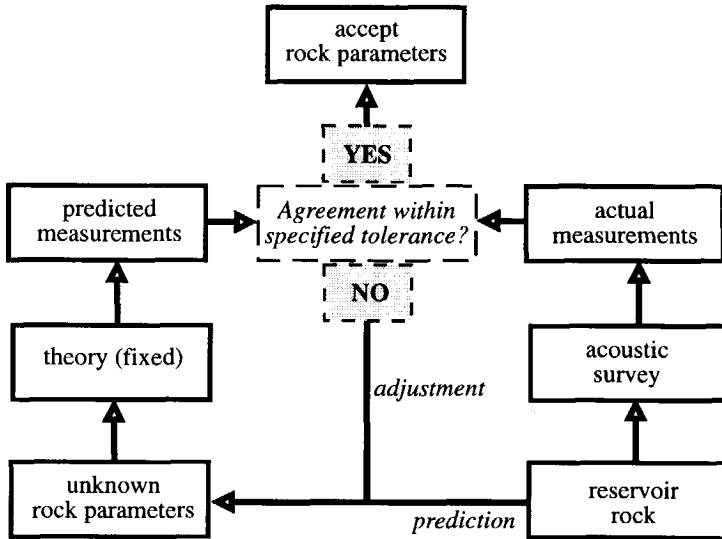


Figure 1.2: *Inversion process*

until the best fit between predicted and actual measurements is obtained. In practice the inversion process is used as a starting point to extract the rock parameters from the actual measurements. The remarkable resemblance between scientific work to find new theories and the practical work done to find rock parameters is noteworthy.

1.3 Literature survey

Theory

A theoretical description of wave propagation and damping in saturated poro-elastic material was already developed in 1956 both by Biot and by De Josselin de Jong. Biot (1956, 1962) derived a straightforward and effective two-phase theory in which the averaged motions of both the solid and

fluid parts of the porous medium were described. A fundamental feature of the Biot theory is the existence of three types of bulk waves: a fast compressional wave, a slow compressional wave, and a shear wave. For the fast compressional wave, the pore fluid and the porous material are compressed simultaneously, but for the slow compressional wave the porous material relaxes when the pore fluid is compressed. These two wave types are therefore often denoted as the 'in-phase' and the 'out-of-phase' wave types, respectively. Independently of Biot, De Josselin de Jong (1956) described acoustic wave propagation through sandstone saturated with water, and he also predicted the occurrence of two compressional waves and a shear wave.

The classical Biot theory contains two limits: the low-frequency and high-frequency limit.

- Low-frequency limit. In this low-frequency limit the frequency is low enough for viscous effects in the fluid to dominate the inertia effects. In this case the viscosity of the fluid causes the fluid motion to 'lock-on' to the solid motion, and consequently the slow wave becomes diffusive instead of propagatory. This low-frequency limit is often called the Biot-Gassmann result (Gassmann, 1951).
- High-frequency limit. In the high-frequency limit the inertial forces are much larger than the viscous forces between the fluid and solid movements. This means that in this case we may ignore any viscosity effects and the only coupling mechanism left between the fluid and solid movements is determined by the tortuosity of the porous material, which is an inertial coupling mechanism.

The frequency-dependent combined effect of inertial forces and viscous drag forces is described by the so-called complex viscosity correction function (Biot, 1956b). This function was evaluated for the flow of a viscous fluid under an oscillatory pressure gradient in a circular tube.

In 1987, Johnson et al. described this complete frequency-dependent interaction between the fluid and solid movement by introducing the dynamic permeability of a rigid fluid-saturated porous medium. This behaviour was reformulated by Smeulders et al. in 1992 using a microstructural approach. Both papers showed that the permeability depends on the frequency of the oscillating flow through the rocks. The dynamic permeability over the entire frequency range can be described by a scaling function. Similar to

Biot's complex viscosity correction function, this scaling function exhibits a transition from the low-frequency behaviour, viscosity-dominated part, to a high-frequency inertia-dominated part. It was also found that the normalized permeability, defined as the dynamic permeability divided by the steady-state permeability, in most practical cases does not depend on the microstructural geometry of the rocks. Numerical calculations of the dynamic permeability for a variety of microstructures were presented by Sheng and Zhou (1988), Yavari and Bedford (1990), and Chapman and Higdon (1992). Experimental data was obtained by Charlaix et al. (1988), Smeulders et al. (1992), Johnson et al. (1994), and Kelder and Smeulders (1996b). Despite the fact that the dynamic permeability does not depend on the microstructural geometry of the rocks, numerical computations indicated that this is probably not the case for microscopically sharp-edged pore geometries (Smeulders et al., 1994).

Biot derived his macroscopic equations for wave propagation in saturated poro-elastic material by postulating definite positive energy density functions. In contrast to Biot's approach, Burridge and Keller (1981), Whitaker (1986), Pride et al. (1992), De Vries (1989), and Geerits (1996) derived the macroscopic equations rigorously from the microscopic equations of the constituents of the fluid-saturated porous medium. To this end, they introduced averaging techniques to translate the microscopic behaviour to a scale much larger than the characteristic pore diameter (macroscopic level). For example, De Vries (1989) developed a linear acoustic theory for wave propagation in a porous medium with the aid of a spatial volume-averaging technique. The resulting macroscopic field equations of this theory have the same appearance as Biot's high frequency-limit equations. In 1996, Geerits extended this theory for the case in which damping of the interface-type is incorporated.

The reflection and transmission of acoustic waves from an interface between a fluid and a fluid-saturated porous medium is another subject of our study with widespread applications. We mention for instance ultrasonic non-destructive evaluation, underwater acoustics, seismology, and acoustic imaging in fluid-filled boreholes. Over the years, many authors have investigated the influence of such an interface on the propagation and reflection characteristics of the three different bulk waves (Allard, 1993). Already in 1960, Deresiewicz (1960) calculated reflection coefficients for these bulk waves generated in a non-dissipative case semi-infinite fluid-saturated porous medium incident at oblique angle upon a free surface. This was extended to

the general case, taking account of the dissipation, by Deresiewicz and Rice (1962). Subsequently, Deresiewicz and Levy (1967) and Chin et al. (1985) successfully derived expressions for both reflection and transmission coefficients at normal incidence. Other authors (Hajra and Mukhopadhyay, 1982; Wu et al., 1990) discussed these coefficients for waves incident at oblique angles, neglecting however dissipation effects.

Experiments

In recent years it has become clear that the acoustic bulk properties (phase speed and bulk attenuation) of artificial porous material saturated with Newtonian fluids are well described by the Biot theory. Extensive quantitative experimental research on porous materials of this type showed the strong predictive power of the Biot theory, and confirmed the attenuation mechanism involved (Hovem and Ingram, 1979; Berryman, 1980; Johnson and Plona, 1982). Moreover, Johnson et al. (1994) and Kelder and Smeulders (1995, 1996a) showed for the same type of samples that all observed phase speeds and the attenuation of the Biot slow wave can be explained by introducing the dynamic permeability in acoustic wave models. The attenuation mechanism for the propagating bulk waves in porous material as proposed by Biot in 1956 is based on viscous dissipation. For the slow wave this results in strong, frequency-dependent attenuation, which makes this wave very difficult to observe. The first clear observation of a propagating slow wave was reported by Plona (1980) for water-saturated sintered glass beads. Following Plona's observation, considerable effort has been expended in trying to detect this slow wave in natural sandstones. Although the slow wave was already detected in thin slabs of air-filled sandstone (Nagy et al., 1990), and in water-saturated, unconsolidated sand (Boyle and Chotiros, 1992), the first measurement of slow wave propagation in natural water-saturated sandstones was reported only recently by Kelder and Smeulders (1997).

Many natural sandstones show much more velocity dispersion and attenuation than is predicted by the Biot theory. Several review articles have been published on this specific subject (Johnston et al., 1979; Gist, 1994; Winkler and Murphy III, 1995). It was suggested that there are important pore structures in natural sandstones that produce additional attenuation relative to the Biot prediction. In this respect, we mention two major non-Biot attenuation mechanisms from literature which cause a significant additional attenuation of waves in natural sandstones, and which might be able to

account for the difficulty to observe the Biot slow wave. The first is the so-called 'local flow' mechanism, which is based on small aspect-ratio microcracks along grain boundaries, generating local fluid flow at the grain scale. Viscous dissipation driven by this local flow increases the wave attenuation (O'Connell and Budiansky, 1977; Murphy et al., 1986). A second mechanism was demonstrated by experimental data from Klimentos and McCann (1988) in artificial rocks made of cemented sand grains. They observed that clay increases the attenuation of the slow wave (relative to the Biot theory prediction) by increasing the pore wall surface area. According to Gist (1994), these two attenuation mechanisms are not present in synthetic porous material because it lacks both the microcracks responsible for local flow, and small-scale pore wall roughness resulting from the growth of clay particles on the surface of the sand grains.

1.4 Approach and thesis outline

In this thesis we investigate both theoretically and experimentally to what extent the frequency-dependent propagation, reflection and damping of acoustic waves is influenced by formation rock properties like porosity, permeability and lithology of the porous material.

On the theoretical side, we investigate the mechanisms of frequency-dependent wave propagation and damping. As was mentioned before, this dynamic behaviour is a result of the relative fluid to solid motion which takes place when a wave propagates through saturated porous rock. We extend the description of existing theoretical models by presenting alternative derivations and we discuss the behaviour of wave propagation in the low and high frequency limit. Besides the influence of the bulk material on wave propagation and damping, we also investigate the frequency-dependent transmission and reflection coefficients of plane waves with oblique incidence on a plane interface between a non-viscous fluid and a dissipative fluid-saturated porous medium.

On the experimental side, we present new and more accurate measurements of acoustic bulk properties of water-saturated porous media. This includes measurements of phase speed, attenuation, and specific attenuation ($1/Q$), for all three types of bulk waves, covering an ultrasonic frequency range from 100 kHz to 1 MHz. A fluid/rock/fluid transmission configuration was chosen, because such a configuration is the most suitable for measuring

the fast compressional wave, slow compressional wave and shear wave. By comparing measurements on two different slab thicknesses of the same material we were able to separate the reflection/transmission effects from the bulk effects and to measure the bulk properties independently. Experimental results are compared with synthetic results, based on the Biot theory. The dynamic permeability is used to describe the frequency-dependent characteristics. It should be noted that all parameters relevant to the Biot theory were measured independently, allowing us to calculate the measured bulk properties. The latter is expected to make an important contribution to the constrained inversion of seismic signals to find rock properties, which is very topical in seismic interpretation.

For test materials we used both artificial sandstone samples and samples cut from Nivelsteiner and Bentheimer sandstone outcrops. The latter sandstone is a reservoir rock in other places. As far as we know, the experimental observation of the Biot slow wave in the natural water-saturated Nivelsteiner sandstone is the first time this wave is observed in such a medium. It enabled us to investigate the viscous damping in natural sandstone more precisely, and to find out quantitatively whether additional mechanisms should be incorporated in the theory. It also allowed us to measure accurately the attenuation of the slow compressional wave, as well as the fast compressional wave and the shear wave.

The thesis outline is as follows:

- Chapter 2 discusses in some detail the basic field equations which govern the elastic wave propagation in fluid-saturated porous media. The equations are based on the Biot theory (1956, 1962) for wave propagation through homogeneous, isotropic porous material. For a better understanding of these field equations we show some alternative derivations.
- Chapter 3 introduces the concept of dynamic permeability (Johnson et al., 1987) in a fluid-saturated rigid porous medium. We also derive a new analytical relationship between the dynamic permeability and rock properties for a model porous medium. This model clearly shows the influence of pore texture on the production parameters.
- Chapter 4 gives the expressions for the acoustic bulk properties of a fluid-saturated porous medium. These theoretical values, based on the

Biot theory, are verified experimentally in Chapter 7. A new aspect in this chapter is the effect of grain compressibility on the high-frequency velocities of both the fast and slow compressional wave.

- Chapter 5 discusses a two-dimensional numerical model from which we obtain frequency-dependent and angle-dependent transmission and reflection coefficients at the interface between a non-viscous fluid and a fluid-saturated porous medium. Results are used to calculate the total transmission coefficients through a fluid-saturated porous layer immersed in fluid.
- Chapter 6 provides a description of the artificial and natural sandstone used for the acoustic experiments. Furthermore, we discuss the experimental determination of the rock parameters of these types of sandstone. Finally, we show the experimental verification in rigid porous media of the scaling function for the dynamic permeability over the full frequency range.
- Chapter 7 shows the ultrasonic wave propagation experiments through disks of water-saturated sandstone placed in a water-filled tank. Results of phase speed, attenuation and specific attenuation ($1/Q$) for all bulk waves are given. Measurements of these bulk properties are compared with theoretical predictions calculated with the Biot theory.

Chapter 2

Basic field equations for fluid-saturated porous media

2.1 Introduction

This chapter discusses the basic field equations which govern elastic wave propagation in fluid-saturated porous media. We use the linearized equations formulated by Biot in 1956 and 1962. In these equations the averaged motions of the solid and fluid parts of the fluid-saturated porous media were considered separately. For the derivation of constitutive relations the generalized Hooke's law was followed. In describing the dynamics in such a medium, he introduced the concept of dynamic coupling between the solid matrix material and the saturating fluid. To describe the macroscopic Biot parameters in terms of microscopic properties of the porous structure, rigorous averaging techniques were applied by authors such as Burridge and Keller (1981), Whitaker (1986), Pride et al. (1992), De Vries (1989), and Geerits (1996).

We start with a general description of poro-elastic material. Next, constitutive relations are discussed within the framework of the Biot theory for poroelasticity (Biot, 1941, 1955). A new aspect is to relate the parameters used in the Biot theory to measurable quantities of the porous aggregate using 'gedanken' experiments and continuity equations. Finally, equations of motion for both the fluid and solid phases are reviewed including the dynamic coupling between these phases.

2.2 Mechanical description of a porous medium

The original Biot theory was developed using a semi-phenomenological, macroscopic approach, based on a set of physically realistic assumptions. This approach means that the microscopic dimensions of the individual constituents of the saturated porous medium are not considered. The following assumptions were made:

- The fluid-filled porous material is constituted in such a way that the fluid phase is fully interconnected. Any sealed void space is considered a part of the solid.
- A so-called representative elementary domain D is defined, which is small compared to the relevant wavelength but large compared to the individual grains and pores of the system.
- Small displacements for both the fluid and solid phases are assumed. This means that equations are presented in their linearized form.
- The fluid neither transmits nor reacts to a shear force in the solid. This is in accordance with the assumption that the fluid has no shear strength.
- The matrix is assumed to be elastic and isotropic, and all the mechanisms of dissipation related to the matrix, such as those due to the possible presence of fluid in the sealed pores, will not be dealt with.
- The absence of thermo-elastic and chemical reaction effects is assumed.

Consider an orthogonal Cartesian reference frame with origin 0 and the three mutually perpendicular base vectors $\{i_1, i_2, i_3\}$ of unit length each (see Figure 2.1). Following the assumption of small displacements for the constituting phases, the strain components e_{ij} for the solid and ε_{ij} for the fluid, respectively, are

$$e_{ij} = 1/2(\partial_j u_i + \partial_i u_j), \quad (2.1)$$

$$\varepsilon_{ij} = 1/2(\partial_j U_i + \partial_i U_j), \quad (2.2)$$

in which the averaged fluid particle displacement U_i and the averaged solid particle displacement u_i follow from an intrinsic volume averaging procedure

$$U_i(\mathbf{x}, t) = \frac{1}{V_f} \int_{\mathbf{x}' \in D^f(\mathbf{x})} U_i^f(\mathbf{x}', t) dV, \quad (2.3a)$$

$$u_i(\mathbf{x}, t) = \frac{1}{V_s} \int_{\mathbf{x}' \in D^s(\mathbf{x})} u_i^s(\mathbf{x}', t) dV, \quad (2.3b)$$

where V_f is the fluid volume, V_s is the solid volume, U_i^f is a local displacement of the fluid, and u_i^s a local displacement of the solid. The vector \mathbf{x} denotes the location of the centroid of the representative elementary domain D within the orthogonal Cartesian reference frame, as depicted in Figure (2.1). The vector \mathbf{x}' is a position vector which denotes locations of points within the fluid or solid part of D .

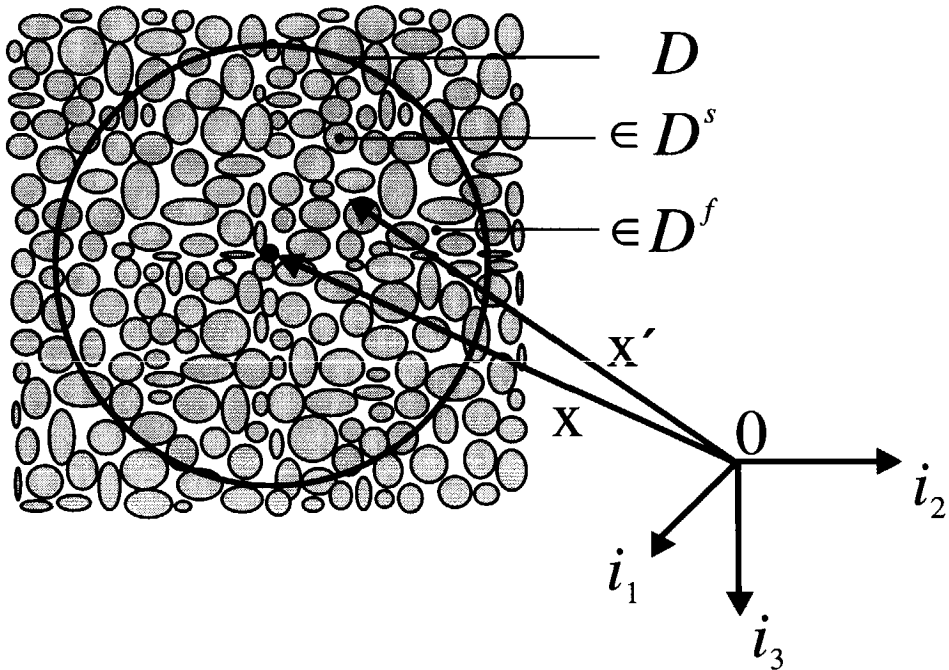


Figure 2.1: The position vector \mathbf{x}' of fluid and solid particles in the subdomains D^f and D^s inside the representative elementary domain D .

Considering a fluid-filled elastic skeleton with a statistical distribution of interconnected pores, the porosity will be denoted by:

$$\phi = \frac{V_\phi}{V_b}, \quad (2.4)$$

where V_ϕ is the volume of the pores contained in a sample of bulk volume V_b . The term 'porosity' refers to the effective porosity, thus including only the interconnected void spaces as opposed to those pores which are sealed off. The total stress tensor in the bulk material is

$$\begin{pmatrix} \tau_{11} + \tau & \tau_{12} & \tau_{13} \\ \tau_{21} & \tau_{22} + \tau & \tau_{23} \\ \tau_{31} & \tau_{32} & \tau_{33} + \tau \end{pmatrix}, \quad (2.5)$$

with the symmetry property $\tau_{ij} = \tau_{ji}$. If we consider a cube of unit size of the bulk material, τ represents the total normal tension force per unit **bulk** area A_b applied to the fluid part of the faces of the cube. Denoting by p the pressure of the fluid in the pores we may write

$$\tau = -\phi p. \quad (2.6)$$

The remaining components τ_{ij} of the total stress tensor are the forces per unit **bulk** area applied to that portion of the cube faces occupied by the solid. They are a result both of the fluid pressure p and the additional intergranular stresses σ_{ij}

$$\tau_{ij} = -\sigma_{ij} - (1 - \phi)p\delta_{ij}, \quad (2.7)$$

where the Kronecker symbol δ_{ij} is obviously introduced because the pore fluid cannot exert nor sustain any shear forces. We notice that the additional intergranular stresses σ_{ij} are defined as negative in tension. They are referred to as 'additional' because they add up to the fluid pressure-induced stresses in the solid (see Equation 2.7). We may also define the forces per unit **solid** area A_s applied to that portion of the cube faces occupied by the solid

$$p_{s,ij} = \tau_{ij}A_b/A_s = -\sigma_{ij}/(1 - \phi) - p\delta_{ij}. \quad (2.8)$$

Obviously, the total normal tension force per unit **fluid** area A_f applied to the fluid part of the faces of the cube can be written as $\tau A_b/A_f = -p$. From

Equations (2.6) and (2.7) it follows that the total stress tensor in the bulk material may also be written as:

$$\begin{pmatrix} -\sigma_{11} - p & -\sigma_{12} & -\sigma_{13} \\ -\sigma_{21} & -\sigma_{22} - p & -\sigma_{23} \\ -\sigma_{31} & -\sigma_{32} & -\sigma_{33} - p \end{pmatrix}. \quad (2.9)$$

This formulation of the total stress tensor is also given by Verruijt (1982); it must however be noted that he denotes the total stress tensor by σ_{ij} and the intergranular stress by $\bar{\sigma}_{ij}$.

2.3 Continuity and constitutive relations

Following the assumptions and definitions as mentioned above, and by a generalization of the procedure followed in the classical theory of elasticity (Love, 1944), the elastic potential energy, V , for a symmetric fluid-filled poro-elastic medium is given by Biot (1955) as:

$$2V = \tau_{11}e_{11} + \tau_{22}e_{22} + \tau_{33}e_{33} + \tau_{12}e_{12} + \tau_{13}e_{13} + \tau_{23}e_{23} + \tau\varepsilon, \quad (2.10)$$

where $\varepsilon = \varepsilon_{kk}$. Summation over repeated indices has been assumed. The form of the strain-energy function (2.10) implies the symmetry of stress, $\tau_{ij} = \tau_{ji}$, and strain, $e_{ij} = e_{ji}$. This reduces the number of independent elastic coefficients in the poro-elastic stress-strain relations, following the generalized Hooke's law, from 81 to 28. In the literature this is known as general anisotropic poro-elasticity. When the material is isotropic, i.e. when there are no preferred directions in the material which means the principal stress and strain directions coincide, this is reduced to four distinct elastic coefficients. Introducing the elastic constants G , A , Q and R , the stress-strain relations for an isotropic rock may be written as (Biot, 1955)

$$\tau_{ij} = 2Ge_{ij} + Ae_{kk}\delta_{ij} + Q\varepsilon_{kk}\delta_{ij}, \quad (2.11)$$

$$\tau = Qe_{kk} + R\varepsilon_{kk}, \quad (2.12)$$

The parameters A , Q , R and G are generalized elastic coefficients which can be related to such measurable quantities as the porosity ϕ , the fluid bulk modulus K_f , the bulk modulus of the grains K_s , the bulk modulus of the porous composite K_b , and the composite shear modulus G .

The elastic coefficients, determining the deformation properties of the fluid-solid system, were related to measurable quantities by Gassmann (1951), Biot and Willis (1957), Geertsma and Smit (1961), Stoll (1974), Brown and Korringa (1975) and Berryman (1981). Up to now these relationships were always derived from static 'gedanken' experiments on jacketed and unjacketed porous samples. However, in this study the results of these experiments are used to give an alternative derivation of the stress-strain relations from straightforward continuity and constitutive relations.

2.3.1 'Gedanken' experiments

In the 'gedanken' experiments the volume effects caused by the stresses in the porous medium are investigated. As these stresses can be expressed in terms of pore pressures and intergranular stresses, we discuss two experiments in which the influences of the two stresses are studied separately. The first experiment is the so-called unjacketed test in which the influence of pore pressure is studied.

Unjacketed test

When a porous sample is fully submerged in a watertank, while a pressure change dp' is applied, and the sample is assumed to be fully water-saturated, it is immediately clear that the fluid pressure must be continuous over the interface:

$$dp' = dp. \quad (2.13)$$

For the intergranular stresses at the interface we may write

$$d\sigma_{11} = d\sigma_{22} = d\sigma_{33} = 0. \quad (2.14)$$

As there are no changes in the intergranular stresses, the unjacketed test is used to study the volume effects caused by the pore pressure changes. Defining the matrix bulk modulus K_a , the bulk volume change $dV_b = -K_a^{-1}V_b dp$ is measured in this test. In the case of homogeneous bodies, whether or not isotropic, the application of an incremental pressure dp' means applying this increment both to the outer and inner pore surface, which leads to a linear mapping and does not change the porosity ϕ ($d\phi = 0$). Therefore we may write for the volume change of the matrix grains

$$dV_s = (1 - \phi)dV_b = -\frac{1}{K_a}V_s dp. \quad (2.15)$$

This means that for homogeneous media K_a can also be interpreted as the bulk modulus of the single grains, denoted by K_s . In the case of inhomogeneous bodies, it can no longer be argued that the porosity is not influenced by a pressure change. Instead, it seems appropriate to introduce a bulk modulus of the pore volume $K_\phi^{-1} = -(\phi V_b)^{-1} \partial(\phi V_b) / \partial p$, which leads to

$$d\phi = - \left(\frac{\phi}{K_\phi} - \frac{\phi}{K_a} \right) dp. \quad (2.16)$$

From the relation $d\phi = d[1 - V_s/V_b]$ it can be found that

$$dV_s = - \frac{1}{(1 - \phi)} \left(\frac{1}{K_a} - \frac{\phi}{K_\phi} \right) V_s dp. \quad (2.17)$$

Although it seems straightforward to determine the coefficient K_a by measuring the displacements of the sample's boundary surfaces it is not immediately clear how to determine K_ϕ . This problem was discussed by Biot and Willis (1957), who proposed measuring the increment of pore fluid content. We will not discuss this any further and will assume homogeneity from now on.

Jacketed test

The second experiment is the so-called jacketed test in which the influence of intergranular stresses is studied. In this case, a porous sample is jacketed and fully submerged in a watertank (pressure change dp') and the inside of the jacket is allowed to communicate with the atmosphere via a tube to ensure constant internal fluid pressure. We may write (cf. (2.9) and $dp = 0$)

$$dp' = d\sigma_{11} = d\sigma_{22} = d\sigma_{33}. \quad (2.18)$$

As there are no pore pressure changes, the jacketed test is used to study the volume effects caused by intergranular stresses. Defining the matrix bulk modulus K_b , the bulk volume change $dV_b = -K_b^{-1} V_b d\sigma$ is measured in this test, where σ is the isotropic component of the intergranular stress: $\sigma = \sigma_{kk}/3$. It is often assumed that a dry specimen exhibits the same properties as a fully saturated one and therefore the conventional jacketed test is usually performed on a dry specimen. Assuming that the response of the solid particles to a unit increase of the average stress induced by the intergranular forces equals the response to a unit increase of the uniform

stress induced in these particles by the fluid pressure, we may write for the volume change of the particles (cf. (2.8) and (2.15))

$$dV_s = -\frac{1}{(1-\phi)} \frac{1}{K_s} V_s d\sigma. \quad (2.19)$$

This relation between the particle volume and the intergranular stress is also described by Verruijt (1982), who initially assumes that the volume change is not described by $[K_a(1-\phi)]^{-1}$, but by a separate parameter β_p . Again using the relation $d\phi = d[1 - V_s/V_b]$, we can find for the porosity change

$$d\phi = -\left(\frac{1-\phi}{K_b} - \frac{1}{K_s}\right) d\sigma. \quad (2.20)$$

Apparently, there is always a porosity change in this type of compression test, whether or not we are discussing homogeneous samples. It can also be argued that a small increase of the intergranular stress must result in a decrease of the porosity, so $\partial\phi/\partial\sigma < 0$. From (2.20), we then find that $(1-\phi)K_s > K_b$, which was also previously stated by Verruijt (1982).

The bulk volume change can now be described as a function of both the pore pressure change and the change of the intergranular stress and thus as a summation of the effects discussed in the previous experiments:

$$dV_b = -\frac{1}{K_b} V_b d\sigma - \frac{1}{K_s} V_b dp. \quad (2.21)$$

Equation (2.21) describes the change in particle volume as a function of the change in pore pressure and intergranular stress. This relation may be rewritten as

$$-\partial_t \sigma = K_b \partial_t e + \frac{K_b}{K_s} \partial_t p, \quad (2.22)$$

where $e = e_{kk} = dV_b/V_b$. Only the intergranular stress σ can produce shear strain. So when we measure the shear modulus of a dry sample, i.e. $p = 0$, the rock shear modulus G can be incorporated following Hooke's law for an isotropic elastic solid. In this way, it can easily be seen from Equation (2.22) that the stress-strain relation for the porous skeleton may be written as (Verruijt, 1982)

$$-\sigma_{ij} = (K_b - \frac{2}{3}G)e\delta_{ij} + 2Ge_{ij} + \frac{K_b}{K_s} p\delta_{ij}. \quad (2.23)$$

In the literature, the effective stress σ'_{ij} is often introduced in such a way that the deformation of the matrix is fully determined by that stress (Verruijt, 1982):

$$-\sigma'_{ij} = -\sigma_{ij} - \frac{K_b}{K_s} p \delta_{ij} = (K_b - \frac{2}{3}G)e\delta_{ij} + 2Ge_{ij}. \quad (2.24)$$

The factor $K_b - \frac{2}{3}G$ is often referred to as λ , whereas μ is frequently used as a different notation for G . λ and μ are known as Lamé's coefficients.

2.3.2 Relations to measurable quantities

We continue with the derivation of stress-strain relations for a fluid-filled porous system by means of continuity and constitutive equations. Considering a homogeneous body, we refer to Equations (2.15) and (2.19). For the fluid, the bulk modulus K_f is introduced. The constitutive relations then become

$$\frac{1}{\rho_s} \partial_t \rho_s = \frac{1}{K_s} \partial_t p + \frac{1}{(1-\phi)} \frac{1}{K_s} \partial_t \sigma, \quad (2.25)$$

$$\frac{1}{\rho_f} \partial_t \rho_f = \frac{1}{K_f} \partial_t p. \quad (2.26)$$

The linearized continuity equations are

$$\partial_t[(1-\phi)\rho_s] + (1-\phi)\rho_s \nabla \cdot \mathbf{v} = 0, \quad (2.27)$$

$$\partial_t(\phi\rho_f) + \phi\rho_f \nabla \cdot \mathbf{w} = 0, \quad (2.28)$$

where we have defined the averaged velocities $\mathbf{w} = \partial_t \mathbf{U}$ and $\mathbf{v} = \partial_t \mathbf{u}$ of the fluid and solid parts of an arbitrary volume element. From the combination of the solid relations (2.25) and (2.27) and the fluid equations (2.26) and (2.28) respectively, we may write

$$\frac{1-\phi}{K_s} \partial_t p + \frac{1}{K_s} \partial_t \sigma - \partial_t \phi + (1-\phi) \nabla \cdot \mathbf{v} = 0, \quad (2.29)$$

$$\frac{\phi}{K_f} \partial_t p + \partial_t \phi + \phi \nabla \cdot \mathbf{w} = 0. \quad (2.30)$$

Elimination of the porosity term by adding the equations yields

$$\left(\frac{1-\phi}{K_s} + \frac{\phi}{K_f} \right) \partial_t p + \frac{1}{K_s} \partial_t \sigma + (1-\phi) \nabla \cdot \mathbf{v} + \phi \nabla \cdot \mathbf{w} = 0. \quad (2.31)$$

This relation is usually called the storage equation, which forms a basic relationship in consolidation problems (Verruijt, 1982). We may now eliminate either σ or p from the storage equation (2.31) with (2.22) and using the identity $\partial_t e = \nabla \cdot \mathbf{v}$. This yields

$$\beta \partial_t p + K_f \left(1 - \phi - \frac{K_b}{K_s} \right) \nabla \cdot \mathbf{v} + \phi K_f \nabla \cdot \mathbf{w} = 0, \quad (2.32)$$

$$\beta \partial_t \sigma + \phi K_b \nabla \cdot \mathbf{v} - \phi K_f \frac{K_b}{K_s} \nabla \cdot \mathbf{w} = 0, \quad (2.33)$$

where we have introduced $\beta = \phi + K_f/K_s(1 - \phi - K_b/K_s)$. Combining the fluid relation (2.32) and the time derivative of the solid relation (2.23) we may obtain the following set stress-strain relations for a fluid-saturated porous medium:

$$-\partial_t \sigma_{ij} - (1 - \phi) \partial_t p \delta_{ij} = G(\partial_i v_j + \partial_j v_i) + A \partial_k v_k \delta_{ij} + Q \partial_k w_k \delta_{ij}, \quad (2.34)$$

$$-\phi \partial_t p = Q \partial_k v_k + R \partial_k w_k, \quad (2.35)$$

where we have introduced the following parameters:

$$A = \frac{\phi K_b + (1 - \phi) K_f (1 - \phi - \frac{K_b}{K_s})}{\beta} - \frac{2}{3} G, \quad (2.36a)$$

$$Q = \frac{\phi K_f (1 - \phi - \frac{K_b}{K_s})}{\beta}, \quad (2.36b)$$

$$R = \frac{\phi^2 K_f}{\beta}. \quad (2.36c)$$

Again, $\beta = \phi + K_f/K_s(1 - \phi - K_b/K_s)$. If we assume that the porous rock and pore fluid are much more compressible than the grains themselves ($K_b/K_s \ll 1$ and $K_f/K_s \ll 1$), we may write

$$A = \frac{(1 - \phi)^2}{\phi} K_f + K_b - \frac{2}{3} G, \quad (2.37a)$$

$$Q = K_f (1 - \phi), \quad (2.37b)$$

$$R = \phi K_f. \quad (2.37c)$$

The parameters A , Q and R were also used by Biot (1956a), Biot and Willis (1957), Geertsma and Smit (1961), Stoll (1974), Johnson (1986) and

Smeulders et al. (1992), but up to now they were always derived from static 'gedanken' experiments on jacketed and unjacketed porous samples and not from straightforward continuity and constitutive relations. Equations (2.34) and (2.35) are the time derivatives and full equivalents of the stress-strain relations (2.11) and (2.12), describing the deformation behaviour of the solid-fluid system. For this, note the use of the identities $\partial_t e = \nabla \cdot \mathbf{v} = \partial_k v_k$, $\partial_t \varepsilon = \nabla \cdot \mathbf{w} = \partial_k w_k$, $\partial_t e_{ij} = 1/2(\partial_i v_j + \partial_j v_i)$ and the pressure-stress definitions in Equations (2.6) and (2.7)

Geerits (1996) defined the constitutive parameters κ^{ff} , κ^{sf} , κ^{fs} , Λ^{ss} , and M^{ss} . It can be shown (see Appendix A) that they can be expressed in terms of the four Biot parameters A , G , Q and R :

$$\kappa^{ff} = \frac{D\phi}{DR - Q^2}, \quad (2.38a)$$

$$\kappa^{fs} = \frac{-Q\phi}{DR - Q^2}, \quad (2.38b)$$

$$\kappa^{sf} = \frac{-Q(1-\phi)}{DR - Q^2}, \quad (2.38c)$$

$$2M^{ss} = \frac{(1-\phi)}{2G}, \quad (2.38d)$$

$$3\Lambda^{ss} = \frac{1}{3} \frac{R(1-\phi)}{DR - Q^2} - \frac{(1-\phi)}{2G}, \quad (2.38e)$$

where $3D = 2G + 3A$.

2.4 Momentum equations

Following Biot (1956a), we consider a homogeneous, isotropic fluid-filled porous medium and assume that the flow of the fluid relative to the solid through the pores is of the Poiseuille type. In this case, the microscopic flow pattern inside the pores will be a linear function of the six average velocity components of the solid and the fluid $v_i = \partial u_i / \partial t$ and $w_i = \partial U_i / \partial t$. The kinetic energy T of this system per unit volume may be expressed as

$$2T = \rho_{11} v_i v_i + 2\rho_{12} v_i w_i + \rho_{22} w_i w_i, \quad (2.39)$$

The density coefficients ρ_{11} and ρ_{22} are related to the density of the solid ρ_s and fluid ρ_f by

$$\rho_{11} = (1-\phi)\rho_s - \rho_{12}, \quad (2.40)$$

$$\rho_{22} = \phi\rho_f - \rho_{12}. \quad (2.41)$$

The coefficient ρ_{12} represents a mass coupling parameter between fluid and solid. It is always negative and proportional to the fluid density

$$\rho_{12} = -(\alpha_\infty - 1)\phi\rho_f, \quad (2.42)$$

where the parameter α_∞ is referred to as the tortuosity parameter ($\alpha_\infty \geq 1$), a purely geometrical quantity.

Similar to the case for the stress-strain relations, Geerits (1996) defined the coupling parameters m^{ff} , m^{ss} , m^{fs} , and m^{sf} . It can be shown (see Appendix A) that they can be expressed in terms of the Biot coefficients ρ_{11} , ρ_{12} , and ρ_{22} :

$$m^{ff} = \frac{\rho_{22}}{\phi}, \quad (2.43a)$$

$$m^{fs} = \frac{\rho_{12}}{(1-\phi)}, \quad (2.43b)$$

$$m^{ss} = \frac{\rho_{11}}{(1-\phi)}, \quad (2.43c)$$

$$m^{sf} = \frac{\rho_{12}}{\phi}. \quad (2.43d)$$

Dissipation energy considerations are based on the fact that dissipation only depends on the relative motion between the fluid and the solid and vanishes when this relative motion is absent. Again, the dissipation energy can be written as a quadratic function of the six average velocity components. The dissipation function D_{dis} is given by

$$2D_{dis} = b_0(v_i - w_i)(v_i - w_i), \quad (2.44)$$

in which $(v_i - w_i)$ is the relative velocity of the fluid with respect to the solid, and b_0 is the dissipation coefficient related to Darcy's coefficient of steady-state permeability k_0 by

$$b_0 = \frac{\eta\phi^2}{k_0}, \quad (2.45)$$

where η is the fluid viscosity. According to Biot (1956a), the Lagrange's momentum equations incorporating dissipation are stated as

$$\partial_t \left(\frac{\partial T}{\partial v_i} \right) + \frac{\partial D_{dis}}{\partial v_i} = -\partial_j \sigma_{ji} - (1-\phi)\partial_i p, \quad (2.46)$$

$$\partial_t \left(\frac{\partial T}{\partial w_i} \right) + \frac{\partial D_{dis}}{\partial w_i} = -\phi \partial_i p, \quad (2.47)$$

where use has been made of the stress definitions in Equations (2.6) and (2.7). The L.H.S. of Equations (2.46) and (2.47) denotes the acceleration of the phase, and the R.H.S. denotes the total force acting on the phase under consideration per unit volume. Substituting the kinetic energy equation (2.39) and the dissipation function equation (2.44) in the Lagrange's equations (2.46) and (2.47) results in

$$-\partial_j \sigma_{ji} - (1 - \phi) \partial_i p = \partial_t^2 (\rho_{11} u_i + \rho_{12} U_i) + b_0 \partial_t (u_i - U_i), \quad (2.48)$$

$$-\phi \partial_i p = \partial_t^2 (\rho_{12} u_i + \rho_{22} U_i) - b_0 \partial_t (u_i - U_i). \quad (2.49)$$

These are the Biot equations in the most general form.

For a better understanding of these momentum equations it is useful to discuss a number of limiting cases. We will start with the low-frequency limit by neglecting inertia forces and making use of Darcy's law for low Reynolds-number fluid flow in rigid porous media. In this case, the pressure gradient is balanced by viscous forces according to Darcy's law

$$0 = -\partial_i p - \frac{\eta \phi}{k_0} w_i, \quad (2.50)$$

where $w_i = \partial_t U_i$ is the velocity component of the fluid in direction i . When oscillating fluid motion is involved, Darcy's law only holds in the low-frequency limit. At higher frequencies unsteady terms have to be added

$$\phi \rho_f \partial_t w_i + (\alpha_\infty - 1) \phi \rho_f \partial_t w_i = -\phi \partial_i p - b_0 w_i, \quad (2.51)$$

The first term on the left side of Equation (2.51) is the inertia term. The second term on the left side describes the unsteady interaction, originating from the pore fluid acceleration in a narrow-widening micro-structural porous geometry. The direction of acceleration on a micro-scale may very well differ from the macroscopic acceleration direction. This means that $(\alpha_\infty - 1)$ describes the deviation of the arbitrary tortuosity from the tortuosity of a cylindrical duct. In the high-frequency limit ($\omega \rightarrow \infty$), the steady interaction may be ignored:

$$\alpha_\infty \phi \rho_f \partial_t w_i = -\phi \partial_i p. \quad (2.52)$$

The discussion above states that pressure gradients are either balanced by viscous forces (low-frequency limit), or by inertia forces (high-frequency limit), but generally by a combination of both.

If motion of the porous solid material is allowed, only minor modifications in the steady and unsteady interaction terms of Eq. (2.51) are required, with $v_i = \partial_t u_i$ as the solid velocity:

$$\phi \rho_f \partial_t w_i = -\phi \partial_i p + b_0 (v_i - w_i) + (\alpha_\infty - 1) \phi \rho_f \partial_t (v_i - w_i). \quad (2.53)$$

For the fluid-saturated porous material as a whole we may find an expression similar to Equation (2.53)

$$\phi \rho_f \partial_t w_i + (1 - \phi) \rho_s \partial_t v_i = -\partial_j \sigma_{ij} - \partial_i p. \quad (2.54)$$

Subtracting Equation (2.53) from Equation (2.54), and rearranging terms, we may write for the solid and fluid components respectively

$$-\partial_j \sigma_{ji} - (1 - \phi) \partial_i p = \partial_t (\rho_{11} v_i + \rho_{12} w_i) + b_0 (v_i - w_i), \quad (2.55)$$

$$-\phi \partial_i p = \partial_t (\rho_{12} v_i + \rho_{22} w_i) - b_0 (v_i - w_i), \quad (2.56)$$

with the density terms ρ_{11} , ρ_{22} , and ρ_{12} formulated in Equations (2.40), (2.41), and (2.42), respectively. By replacing the velocity terms in the R.H.S. of Equations (2.55) and (2.56) with the time derivatives of the displacement fields, we end up with the momentum equations which are exactly analogous to those formulated by Biot (1956a) and De Josselin de Jong (1956) (cf. Equations (2.48) and (2.49)).

Up to now, we assumed that the flow of the fluid relative to the solid through the pores is of the Poiseuille type. This resulted in a constant Darcy related friction between the relative fluid and solid motions in the porous system, denoted by the friction constant b_0 . Biot (1956b) extended this low frequency range wave propagation to the higher frequency range. It turns out that the Darcy related friction b_0 should be replaced by a complex-valued, frequency dependent drag coefficient, $b_0 \hat{F}(\omega)$. At low frequencies, this drag coefficient will show a Stokes-flow behaviour, whereas at higher frequencies, when the viscous skin depth $\delta = \sqrt{2\eta/\omega\rho_f}$ decreases, inertial effects will become dominant. To this end, Biot (1956b) modelled the porous medium as an ensemble of cylindrical ducts. In the next chapter we will give a thorough description of this frequency-dependent behaviour by means of the so-called dynamic permeability, introduced by Johnson et al. (1987).

Chapter 3

Dynamic interaction

3.1 Introduction

An important aspect of wave propagation in a porous medium is the frequency-dependent interaction between the pore fluid and the solid matrix. For low frequencies, a constant Darcy-related friction between the fluid and solid phases is dominant. At higher frequencies, inertial effects are dominant. These aspects were first mentioned by Zwikker and Kosten (1949) and Biot (1956b). Zwikker and Kosten derived analytical expressions for frequency-dependent friction at the wall of a gas-filled circular tube. Biot studied viscous fluid flow under an oscillatory pressure gradient either between parallel walls or in a circular tube. Biot also showed that his results could be applied to any arbitrary porous medium. In 1987, Johnson et al. described this frequency-dependent interaction between the fluid and solid by a dynamic permeability factor. Their description differed slightly from the one used by Biot, but showed the same behaviour in the low- and high-frequency limits. The approach of Johnson et al. was based on energy flux considerations on the microscale. Smeulders et al. (1992) found the same results but used a more rigorous averaging method. All papers showed that the permeability, a key property of productive rock formations, depends on the frequency of the oscillating flow through the rocks.

3.2 Dynamic permeability for a fluid-filled rigid porous medium

Johnson et al. (1987) (to be referred to as 'JKD', i.e. Johnson, Koplik, and Dashen) have provided an interesting model for the so-called dynamic permeability of a fluid-saturated porous medium fully saturated with a Newtonian fluid. It is important to note that all important features in this model refer to a rigid porous medium. Introducing an $\exp(-i\omega t)$ dependence for the fluid pressure p and the macroscopic fluid velocity \mathbf{w} , the Biot equation for the fluid part of the porous medium, cf. Equations (2.45) and (2.53), may be written as

$$\left[\frac{\eta\phi}{k_0} - i\omega\alpha_\infty\rho_f \right] \hat{\mathbf{w}} = -\nabla\hat{p}, \quad (3.1)$$

From this it follows that the dynamic fluid behaviour may be characterized on a macroscopic scale by the dynamic permeability $\hat{k}(\omega)$ or, alternatively, by the dynamic tortuosity $\hat{\alpha}(\omega)$,

$$\frac{\eta\phi}{\hat{k}(\omega)} \hat{\mathbf{w}} = -\nabla\hat{p}, \quad (3.2)$$

$$-i\omega\rho_f\hat{\alpha}(\omega)\hat{\mathbf{w}} = -\nabla\hat{p}. \quad (3.3)$$

Obviously, Equations (3.2) and (3.3) are alternative descriptions of the same physical reality, thus $\hat{k}(\omega)$ and $\hat{\alpha}(\omega)$ are related as follows

$$\hat{\alpha}(\omega) = -\frac{i\eta\phi}{\hat{k}(\omega)\omega\rho_f}. \quad (3.4)$$

In the low frequency limit the dynamic permeability approaches the (real-valued) stationary value k_0 ,

$$\lim_{\omega \rightarrow 0} \hat{k}(\omega) = k_0. \quad (3.5)$$

Consequently, we obtain for the low-frequency limit dynamic tortuosity

$$\lim_{\omega \rightarrow 0} \hat{\alpha}(\omega) = \frac{i\eta\phi}{k_0\omega\rho_f}. \quad (3.6)$$

In this limit the fluid follows a Stokes flow pattern. At higher frequencies, where the viscous skin depth $\delta = \sqrt{2\eta/\omega\rho_f}$ is small compared to the characteristic pore sizes, the fluid obeys a potential flow pattern, except within

a thin layer of size δ along the walls. However, JKD noticed that δ is arbitrarily small at high enough frequencies and that therefore the walls of the pores in the boundary region appear to be flat. Using a boundary layer approach, they were then able to describe the asymptotic behaviour of $\hat{\alpha}(\omega)$ approaching its limit α_∞ . The results for this high-frequency behaviour of $\hat{k}(\omega)$ and $\hat{\alpha}(\omega)$ are ($\omega \rightarrow \infty$):

$$\hat{k}(\omega) = -\frac{i\eta\phi}{\alpha_\infty\omega\rho_f} \left[1 - \left(\frac{i\eta}{\rho_f\omega} \right)^{1/2} \frac{2}{\Lambda} \right], \quad (3.7)$$

$$\hat{\alpha}(\omega) = \alpha_\infty \left[1 + \left(\frac{i\eta}{\rho_f\omega} \right)^{1/2} \frac{2}{\Lambda} \right], \quad (3.8)$$

where Λ is an independently measurable property of the porous material with the dimension of length, and α_∞ is the tortuosity or added mass parameter, defined by its extreme high-frequency limit

$$\lim_{\omega \rightarrow \infty} \hat{\alpha}(\omega) = \alpha_\infty. \quad (3.9)$$

Having defined how the average time-harmonic flow through a porous material behaves in the limit both of low frequencies (Darcy's law) and high frequencies (inviscid flow except for a thin viscous boundary layer near the pore walls), JKD connect the two limits for $\hat{k}(\omega)$ and $\hat{\alpha}(\omega)$ with a postulated function given by

$$\frac{\hat{k}(\omega)}{k_0} = \left[\left(1 - \frac{iM}{2} \frac{\omega}{\omega_c} \right)^{1/2} - i \frac{\omega}{\omega_c} \right]^{-1}. \quad (3.10)$$

in which ω_c is a rollover frequency from a viscosity-dominated regime to an inertia-dominated one, defined as

$$\omega_c = \frac{\eta\phi}{\rho k_0 \alpha_\infty}, \quad (3.11)$$

and M is the similarity parameter defined by JKD as

$$M = \frac{8\alpha_\infty k_0}{\phi\Lambda^2}. \quad (3.12)$$

In the same paper, JKD generalized these results by suggesting that M is equal to 1 for all porous media, at least approximately. This assumption

that only one scaling function $\hat{k}(\omega)/k_0$ exist for all porous media, as given in Equation (3.10), was validated in later years, both numerically and experimentally. Numerical calculations of the dynamic permeability for a variety of microstructures were presented by Sheng and Zhou (1988), Yavari and Bedford (1990), and Chapman and Higdon (1992). Experimental data were obtained by Charlaix et al. (1988), Smeulders et al. (1992), and Johnson et al. (1994). Other authors have discussed calculations on extreme geometries. Pride et al. (1993) showed that Equation (3.10) might be expected to break down for a model of pores with variable widths. Smeulders et al.

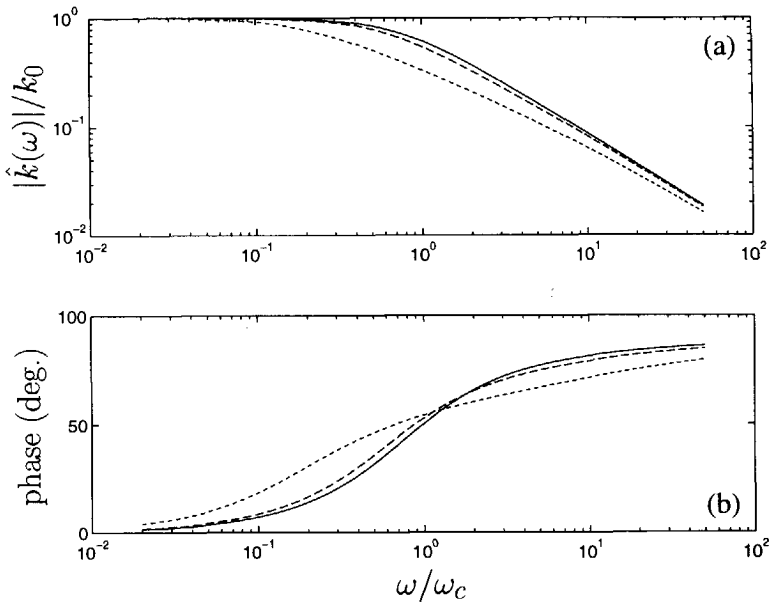


Figure 3.1: Amplitude (a) and phase values (b) of the reduced dynamic permeability for $M = 1$ (—), $M = 2$ (---), and $M = 10$ (---)

(1994) discussed that M might deviate considerably from the value 1 for sharp-edged porous media. In Figures (3.1a) and (3.1b), the amplitude and phase values of the reduced dynamic permeability, $\hat{k}(\omega)/k_0$, are plotted as a function of the reduced frequency, ω/ω_c . To show the influence of different M -values on this scaling function, results are plotted for $M = 1, 2$, and 10. Figures (3.1a) and (3.1b) show that for low frequencies $\hat{k}(\omega)$ approaches its stationary value k_0 . In this case, there is no phase shift. For higher frequencies $\hat{k}(\omega)$ shows ω^{-1} behaviour, and the phase shift tends to 90° . We

also observe that the choice of M influences the plots significantly. A study of the similarity parameter M for different sharp-edged pore structures was published by Smeulders et al. (1992, 1994). In the next section we extend that study by discussing the effects on the parameter M of narrowing and widening non-interconnected pore channels.

The conventional approach has been to treat the pore space as an ensemble of circular tubes (Biot, 1956a, 1962). In this model the dynamic dissipation coefficient $\hat{b}(\omega)/b_0 = \hat{F}(\omega)$ is described by first and zeroth order Bessel functions, where the function $\hat{F}(\omega)$ is given in Equation (3.22). The dynamic permeability model of JKD offers an alternative description for the dynamic dissipation. The scaling function for the dynamic permeability is

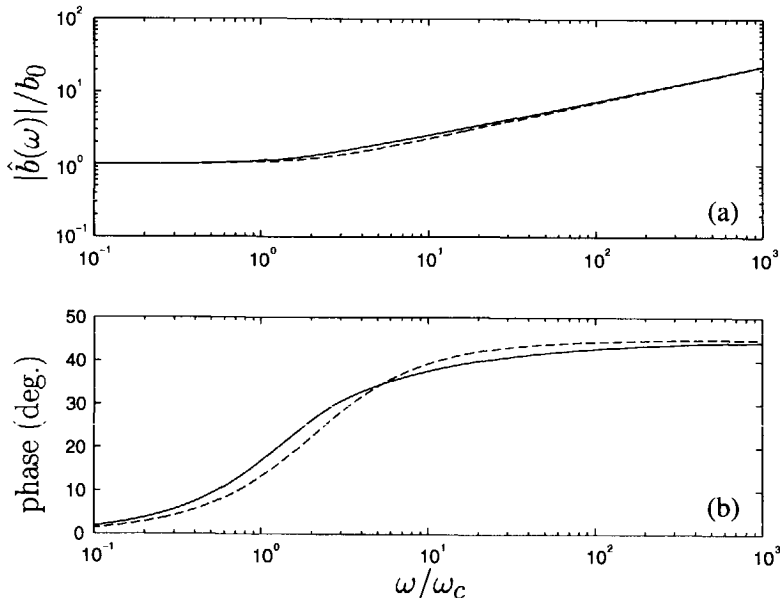


Figure 3.2: Amplitude (a) and phase values (b) of interaction force $\hat{b}(\omega)/b_0$ for tube flow (—) and the scaling function of JKD (---).

given in Equation (3.10). Using the relation

$$\frac{\hat{b}(\omega)}{b_0} = \frac{k_0}{\hat{k}(\omega)} + i \frac{\omega}{\omega_c}, \quad (3.13)$$

we find

$$\frac{\hat{b}(\omega)}{b_0} = \sqrt{1 - \frac{iM}{2} \frac{\omega}{\omega_c}}. \quad (3.14)$$

A comparison of the two models in terms of amplitude and phase values of the reduced dissipation $\hat{b}(\omega)/b_0$ as a function of the reduced frequency ω/ω_c is plotted in Figures (3.2a) and (3.2b). For the JKD model, we have used $M = 1$. From Figures (3.2a) and (3.2b) we notice that the two functions essentially display the same behaviour. One clearly observes the rollover of the absolute values of $\hat{b}(\omega)/b_0$ from the value 1 at low frequencies to an increasing friction at higher frequencies. Only minor differences occur in the behaviour of the phase values of the two cases in the limit of low and high frequencies. It is therefore plausible to say that the frequency dependence of the JKD model is similar to that of a grouping of constant-width flow channels; however, it is more elegant in its analytic form.

3.3 Dynamic behaviour for a model porous medium

We consider a cylinder consisting of N non-interconnected tubes per unit area. The tubes have different radii R_1 and R_2 over a length of L_1 and L_2 , respectively. The total length of the cylinder is L , see Figure (3.3). For this

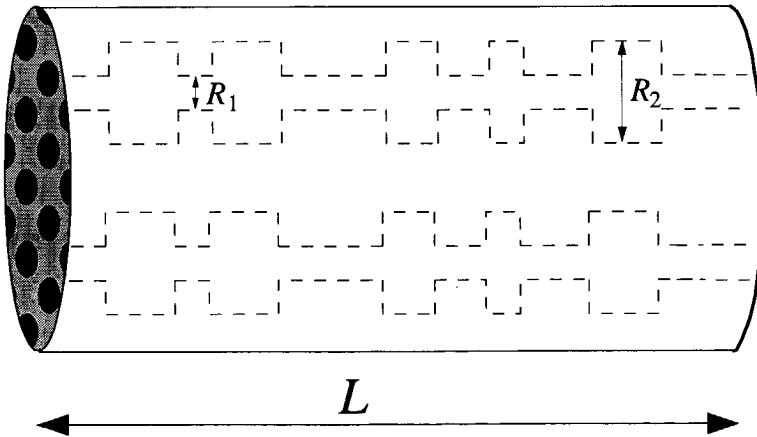


Figure 3.3: A cylinder with a bimodal pore size distribution.

model the porosity ϕ of the cylinder can be written as

$$\phi = N \left[\frac{L_1}{L} \pi R_1^2 + \frac{L_2}{L} \pi R_2^2 \right]. \quad (3.15)$$

A constant pressure gradient ∇p causes a steady-state fluid current through the cylinder's tubes. The fluid current is considered a Poiseuille current, i.e. laminar and incompressible. We will ignore transition effects caused by the narrowing and widening of the tubes. The Poiseuille current has a parabolic velocity profile and the volume flux Q_v can be written as

$$Q_v = -\frac{\pi R^4}{8\eta} \nabla p. \quad (3.16)$$

The pressure difference over the cylinder therefore is

$$\Delta p = p(0) - p(L) = \frac{8\eta Q_v}{\pi} \left[\frac{L_1}{R_1^4} + \frac{L_2}{R_2^4} \right]. \quad (3.17)$$

Using Equations (3.15), (3.17), and Darcy's law as defined in Equation (2.50), in which $w = Q_v N / \phi$ is the macroscopic fluid velocity in the cylinder, the Darcy resistance can be written as

$$\frac{1}{k_0} = \frac{8}{\phi} \left[\frac{L_1}{L} R_1^2 + \frac{L_2}{L} R_2^2 \right] \left[\frac{L_1}{L} \frac{1}{R_1^4} + \frac{L_2}{L} \frac{1}{R_2^4} \right], \quad (3.18)$$

where k_0 is the steady-state permeability. Notice that for a cylinder consisting of tubes with a constant radius R , we find $k_0 = \frac{1}{8} \phi R^2$. Adopting the notation

$$\langle R^n \rangle = \left[\frac{L_1}{L} R_1^n + \frac{L_2}{L} R_2^n \right], \quad (3.19)$$

we may write

$$\frac{1}{k_0} = \frac{8}{\phi} \langle R^2 \rangle \langle R^{-4} \rangle. \quad (3.20)$$

To describe the dynamic interaction of the fluid and the solid walls of the tubes in the cylinder, we will extend the steady-state flow to the case of an oscillatory pressure gradient. Ignoring transition effects caused by the narrowing and widening of the tubes, the pressure difference $\Delta \hat{p}$ for an oscillatory flow may be written as (Zwicker and Kosten, 1949)

$$\Delta \hat{p} = -\hat{w}_1 L_1 \left[i\omega \rho_f - \frac{8\eta}{R_1^2} F(\kappa_1) \right] - \hat{w}_2 L_2 \left[i\omega \rho_f - \frac{8\eta}{R_2^2} F(\kappa_2) \right]. \quad (3.21)$$

Here an $\exp(-i\omega t)$ dependence has been assumed for the relevant quantities. The microscopic fluid velocities in the tubes are denoted by $\hat{w}_1 = \hat{Q}_v/\pi R_1^2$ and $\hat{w}_2 = \hat{Q}_v/\pi R_2^2$. The parameter $\hat{F}(\kappa_j)$ for ($j = 1, 2$) is given by

$$\hat{F}(\kappa_j) = -\frac{i\kappa_j^2}{8} \frac{2J_1(\kappa_j\sqrt{i})}{\kappa_j\sqrt{i}J_0(\kappa_j\sqrt{i}) - 2J_1(\kappa_j\sqrt{i})}, \quad (3.22)$$

where $\kappa_j = R_j\sqrt{\omega\rho_f/\eta}$, and J_0 and J_1 are Bessel functions of zeroth and first order, respectively. Combining Equations (3.3) and (3.21) yields

$$\hat{\alpha}(\omega) = \frac{\phi}{N} \left[\frac{L_1}{L} \frac{1}{\pi R_1^2} \left(1 - \frac{8}{i\kappa_1^2} F(\kappa_1)\right) + \frac{L_2}{L} \frac{1}{\pi R_2^2} \left(1 - \frac{8}{i\kappa_2^2} F(\kappa_2)\right) \right]. \quad (3.23)$$

Substituting the porosity relation (3.15), we arrive at

$$\hat{\alpha}(\omega) = \left[\frac{L_1}{L} \pi R_1^2 + \frac{L_2}{L} \pi R_2^2 \right] \times \left[\frac{L_1}{L} \frac{1}{\pi R_1^2} \left(1 - \frac{8}{i\kappa_1^2} F(\kappa_1)\right) + \frac{L_2}{L} \frac{1}{\pi R_2^2} \left(1 - \frac{8}{i\kappa_2^2} F(\kappa_2)\right) \right]. \quad (3.24)$$

In the limit for high frequencies, it can be shown that

$$\lim_{\kappa_j \rightarrow \infty} F(\kappa_j) = \frac{1}{8} \sqrt{2} \kappa_j (1 - i). \quad (3.25)$$

Substituting Equation (3.25) into (3.24) and using notation (3.19) yields ($\omega \rightarrow \infty$):

$$\hat{\alpha}(\omega) = \langle R^2 \rangle \left[\langle R^{-2} \rangle + \langle R^{-3} \rangle \delta(\omega) + i \langle R^{-3} \rangle \delta(\omega) \right], \quad (3.26)$$

where $\delta(\omega)$ is the viscous skin depth defined by $\delta = \sqrt{2\eta/\omega\rho_f}$. Relation (3.26) can be written as

$$\hat{\alpha}(\omega) = \alpha_\infty \left[1 + (1 + i) \frac{\delta(\omega)}{\Lambda} \right], \quad (3.27)$$

where

$$\alpha_\infty = \langle R^2 \rangle \langle R^{-2} \rangle, \quad (3.28)$$

and

$$\frac{1}{\Lambda} = \frac{\langle R^{-3} \rangle}{\langle R^{-2} \rangle}. \quad (3.29)$$

In this way we have introduced the tortuosity parameter α_∞ and a characteristic length scale Λ of the porous medium. Both the definitions of α_∞ and Λ are in accordance with the ones given by JKD and Smeulders et al. (1992, 1994) for arbitrary porous media. It is now possible to plot the dimensionless

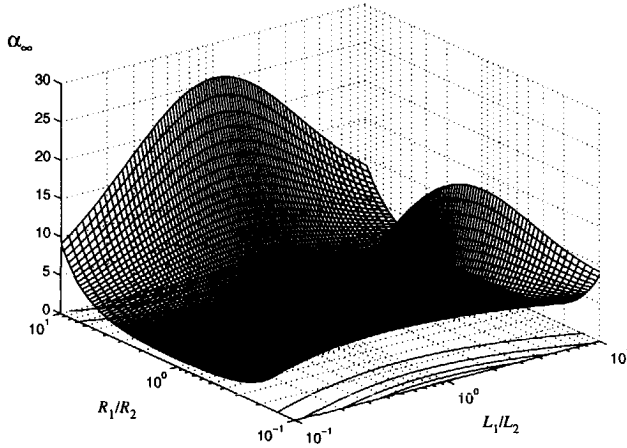


Figure 3.4: Influence of tube configuration on tortuosity α_∞

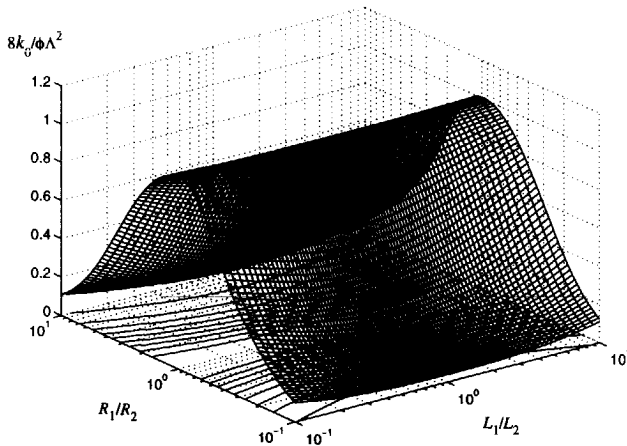


Figure 3.5: Influence of tube configuration on reduced permeability $8k_0/\phi\Lambda^2$

parameters α_∞ and $8k_0/\phi\Lambda^2$ as a function of L_1/L_2 and R_1/R_2 , where

$$\frac{8k_0}{\phi\Lambda^2} = \frac{\langle R^{-3} \rangle^2}{\langle R^{-2} \rangle^2 \langle R^2 \rangle \langle R^{-4} \rangle}. \quad (3.30)$$

The results are given in Figures (3.4) and (3.5). In both cases we observe that the tortuosity and the reduced permeability are equal to unity for $R_1/R_2 = 1$. In Figure (3.4) the tortuosity α_∞ increases for increasing inequality of R_1 and R_2 , but it decreases for increasing inequality of L_1 and L_2 . Wide pores with narrow throats therefore have a high tortuosity value. Figure (3.5) shows that the reduced permeability decreases for increasing inequality of R_1 and R_2 , but it is not influenced too much by the L_1/L_2 ratio. This means that the presence of one narrow throat already drastically reduces the permeability. Combining Equations (3.28) and (3.30) yields:

$$M = \frac{8\alpha_\infty k_0}{\phi\Lambda^2} = \frac{\langle R^{-3} \rangle^2}{\langle R^{-4} \rangle \langle R^{-2} \rangle}. \quad (3.31)$$

Note that for straight tubes ($R_1 = R_2$) $M = 1$. In Figure (3.6) we have plotted M as a function of L_1/L_2 and R_1/R_2 . We note that the similarity

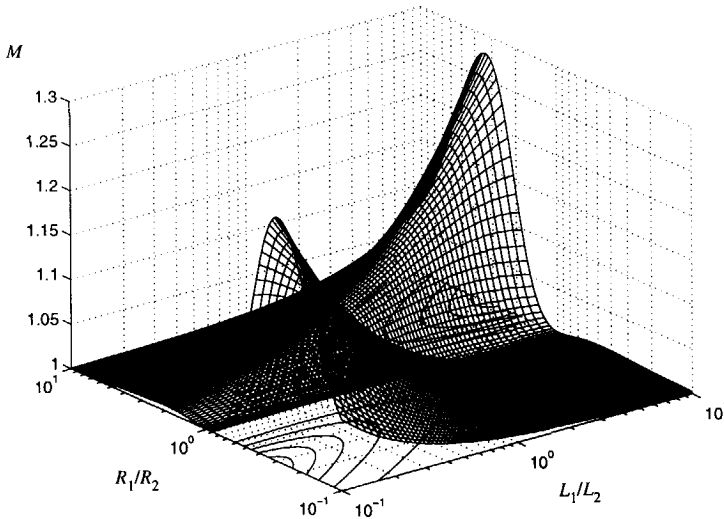


Figure 3.6: Influence of tube configuration on similarity parameter M

parameter M remains of the order 1 for a wide variety of cylinder configurations. This confirms the suggestion made by JKD that M is equal to 1 for all porous media, or at least close to this value.

3.4 Acoustics in deformable porous media

We will now briefly mention the relationship to acoustics in deformable porous media. From relation (2.53), the equation of motion for the fluid constituent may be written as

$$-i\omega\rho_f\hat{\mathbf{w}} = -\nabla\hat{p} + \frac{\phi\eta}{\hat{k}(\omega)}(\hat{\mathbf{v}} - \hat{\mathbf{w}}) + i\omega\rho_f(\hat{\mathbf{v}} - \hat{\mathbf{w}}). \quad (3.32)$$

In this relation frequency-dependence is introduced by replacing the steady-state interaction factor b_0 with the dynamic permeability parameter of JKD. The implications are that the general properties of $\hat{k}(\omega)$ in rigid porous media automatically apply to the acoustics of deformable porous media, via the Biot theory. The relationship between b_0 and $\hat{k}(\omega)$ has been made explicit in Equation (3.13). From that relation, it is obvious that by considering the Biot equations in the limit that the skeletal frame moduli are much larger than the bulk modulus of the fluid, so that the solid does not move ($\hat{\mathbf{v}} = 0$), Equation (3.32) reduces identically to Equation (3.2). By using the circular tube model of Zwikker and Kosten (1949) and Biot (1956b), Equation (3.32) was also found by Johnson and Plona (1982).

Chapter 4

Acoustic bulk properties of fluid-saturated porous media

4.1 Introduction

In this chapter we will discuss the acoustic bulk properties of fluid-saturated porous media, i.e. phase speed, attenuation, and specific attenuation $1/Q$. These parameters can be obtained by solving the Biot momentum equations and stress-strain relations as discussed in Chapter 2, including the concept of dynamic permeability as treated in Chapter 3. A new aspect in this discussion is the investigation of the grain compressibility effects on the high-frequency limit velocities of the fast and slow compressional waves.

4.2 On potentials

To investigate the frequency-dependent acoustic bulk properties of a fluid-solid system, the field equations will be transformed to the wavenumber-frequency domain. To this end, we define a temporal transformation of the function $\hat{f}(\mathbf{x}, \omega)$ to the frequency domain. With t as the integration variable, the temporal Fourier transform and its inverse follow as

$$\hat{f}(\mathbf{x}, \omega) = \int_{-\infty}^{\infty} f(\mathbf{x}, t) \exp(i\omega t) dt, \quad (4.1a)$$

$$f(\mathbf{x}, t) = \frac{1}{2\pi} \int_{-\infty}^{\infty} \hat{f}(\mathbf{x}, \omega) \exp(-i\omega t) d\omega. \quad (4.1b)$$

where $\mathbf{x} = \{x_1, x_2, x_3\}$ is the position vector in a Cartesian reference frame. We start our analysis by eliminating the pore fluid pressure p and the intergranular stress tensor σ_{ij} from the stress-strain relations (2.11)-(2.12) and the momentum equations (2.55)-(2.56). Subsequently, applying the temporal transformation (4.1) to the resulting set of equations we arrive at the following time-harmonic coupled relations:

$$-\hat{\rho}_{11}\omega^2\hat{\mathbf{u}} - \hat{\rho}_{12}\omega^2\hat{\mathbf{U}} = (P - G)\nabla(\nabla \cdot \hat{\mathbf{u}}) + Q\nabla(\nabla \cdot \hat{\mathbf{U}}) + G\nabla^2\hat{\mathbf{u}}, \quad (4.2)$$

$$-\hat{\rho}_{22}\omega^2\hat{\mathbf{U}} - \hat{\rho}_{12}\omega^2\hat{\mathbf{u}} = R\nabla(\nabla \cdot \hat{\mathbf{U}}) + Q\nabla(\nabla \cdot \hat{\mathbf{u}}), \quad (4.3)$$

in which use has been made of a newly introduced parameter $P = A + 2G$ and where

$$\hat{\rho}_{12} = \rho_{12} - i\hat{b}(\omega)/\omega, \quad (4.4)$$

$$\hat{\rho}_{11} = \rho_{11} + i\hat{b}(\omega)/\omega, \quad (4.5)$$

$$\hat{\rho}_{22} = \rho_{22} + i\hat{b}(\omega)/\omega. \quad (4.6)$$

The density terms ρ_{11} , ρ_{22} , and ρ_{12} are defined in Equations (2.40)-(2.42), respectively. Furthermore, we have introduced the frequency-dependent parameter $\hat{b}(\omega)$, as formulated in Equation (3.14), describing the dynamic interaction force between the fluid and the solid matrix. The solid displacement vector $\hat{\mathbf{u}}$ and fluid displacement vector $\hat{\mathbf{U}}$ may be decomposed into longitudinal (compressional) and transverse (shear) vector components. To this end, we may define the Lamé potentials according to

$$\hat{\mathbf{u}} = \nabla\hat{\Phi}_s + \nabla \times \hat{\Psi}_s, \quad (4.7)$$

$$\hat{\mathbf{U}} = \nabla\hat{\Phi}_f + \nabla \times \hat{\Psi}_f. \quad (4.8)$$

in which the subscripts s and f denote the solid phase and fluid phase, respectively. $\{\hat{\Phi}_f, \hat{\Phi}_s\}$ and $\{\hat{\Psi}_f, \hat{\Psi}_s\}$ are called the compressional wave and shear wave potentials of $\{\hat{\mathbf{U}}, \hat{\mathbf{u}}\}$, respectively. Note that with this definition

$$\nabla \cdot \hat{\mathbf{u}} = \nabla^2\hat{\Phi}_s, \quad (4.9)$$

$$\nabla \times \hat{\mathbf{u}} = \nabla \times (\nabla \times \hat{\Psi}_s), \quad (4.10)$$

$$\nabla \cdot \hat{\mathbf{U}} = \nabla^2\hat{\Phi}_f. \quad (4.11)$$

Upon substitution of Equations (4.7)-(4.11), Equations (4.2) and (4.3) separate into two uncoupled sets of equations, referring to the compressional

wavefield components and to the shear wavefield components. For the compressional waves we end up with

$$-\hat{\rho}_{11}\omega^2\hat{\Phi}_s - \hat{\rho}_{12}\omega^2\hat{\Phi}_f = P\nabla^2\hat{\Phi}_s + Q\nabla^2\hat{\Phi}_f, \quad (4.12a)$$

$$-\hat{\rho}_{22}\omega^2\hat{\Phi}_f - \hat{\rho}_{12}\omega^2\hat{\Phi}_s = R\nabla^2\hat{\Phi}_f + Q\nabla^2\hat{\Phi}_s, \quad (4.12b)$$

and for the shear waves we may write,

$$-\hat{\rho}_{11}\omega^2\hat{\Psi}_s - \hat{\rho}_{12}\omega^2\hat{\Psi}_f = G\nabla^2\hat{\Psi}_s, \quad (4.13a)$$

$$-\hat{\rho}_{22}\omega^2\hat{\Psi}_f - \hat{\rho}_{12}\omega^2\hat{\Psi}_s = 0. \quad (4.13b)$$

In the following we consider a two-dimensional situation in the X_1X_3 -plane in which the x_3 -axis points vertically downwards. Restricting the discussion to the propagation of in-plane compressional waves (P-waves) and vertically polarized shear waves (SV-waves), Equations (4.7) and (4.8) can be written as (Berkhout, 1987)

$$\hat{u}_1 = \partial_1\hat{\Phi}_s - \partial_3(\hat{\Psi}_s)_2, \quad (4.14a)$$

$$\hat{u}_3 = \partial_3\hat{\Phi}_s + \partial_1(\hat{\Psi}_s)_2, \quad (4.14b)$$

and

$$\hat{U}_1 = \partial_1\hat{\Phi}_f - \partial_3(\hat{\Psi}_f)_2, \quad (4.15a)$$

$$\hat{U}_3 = \partial_3\hat{\Phi}_f + \partial_1(\hat{\Psi}_f)_2, \quad (4.15b)$$

where $(\hat{\Psi}_s)_2$ and $(\hat{\Psi}_f)_2$ represent the x_2 -component of the vector potentials $\hat{\Psi}_f$ and $\hat{\Psi}_s$, respectively. In the following we shall replace these components notationally by $\hat{\Psi}_s$ and $\hat{\Psi}_f$. We will not consider the propagation of cross-plane horizontally polarized shear waves (SH-waves). The in-plane propagation of P-waves is described by Equations (4.12). The in-plane SV waves are described by Equations (4.13). The solution of these two sets of equations can be obtained by the integral transformation of the independent variable x_1 . This means that for the 2-D case, we will apply a spatial Fourier transformation of the horizontal x_1 component to the wavenumber k_1 . For this, we define the spatial transformation of the function $\hat{f}(x_1, \omega)$. With x_1 as the integration variable, the spatial Fourier transform and its inverse follow as

$$\tilde{f}(k_1, \omega) = \int_{-\infty}^{\infty} \hat{f}(x_1, \omega) \exp(-ik_1x_1) dx_1, \quad (4.16a)$$

$$\hat{f}(x_1, \omega) = \frac{1}{2\pi} \int_{-\infty}^{\infty} \tilde{f}(k_1, \omega) \exp(ik_1x_1) dk_1, \quad (4.16b)$$

where k_1 is an element of the 2-D wavenumber vector $\mathbf{k} = \{k_1, 0, k_3\}$. From the definition in Equation (4.16), the following solution for the compressional wave potentials can be proposed

$$\hat{\Phi}_{s,f}(x_1, x_3, \omega) = \tilde{\Phi}_{s,f}(k_1, x_3, \omega) \exp[ik_1 x_1]. \quad (4.17)$$

For the vertically polarized shear wave potentials we have

$$\hat{\Psi}_{s,f}(x_1, x_3, \omega) = \tilde{\Psi}_{s,f}(k_1, x_3, \omega) \exp[ik_1 x_1]. \quad (4.18)$$

This is equivalent to analyzing a type of plane wave solution. Note that according to Snell's Law the wavenumber vector component k_1 is identical for both cases. As the only dependent variable is the vertical component x_3 (Aki and Richards, 1980), an $\exp[ik_{3,p}x_3]$ and $\exp[ik_{3,s}x_3]$ dependence is proposed for the wave potentials $\tilde{\Phi}_{s,f}(k_1, x_3, \omega)$ and $\tilde{\Psi}_{s,f}(k_1, x_3, \omega)$, respectively. Here, $k_{3,p}$ is the vertical component of the compressional wavenumber vector $\mathbf{k}_p = \{k_1, 0, k_{3,p}\}$ for which we have $k_p^2 = k_1^2 + k_{3,p}^2$, with k_p the complex magnitude of the compressional wavenumber vector \mathbf{k}_p . Obviously, $k_{3,s}$ is the vertical component of the shear wavenumber vector $\mathbf{k}_s = \{k_1, 0, k_{3,s}\}$ for which we have $k_s^2 = k_1^2 + k_{3,s}^2$, with k_s the complex magnitude of the shear wavenumber vector \mathbf{k}_s . Expressions for k_p and k_s are obtained from solving the Biot equations for the compressional and shear wave velocities as discussed in the following sections. Because of the dependence of k_1 , in Chapter 5 we will discuss the angle-dependent reflection and transmission coefficients at the interface between a non-viscous fluid and a fluid-saturated porous medium.

4.3 Compressional wave velocities

By a transformation to the (k_1, ω) domain and assuming an $\exp[ik_{3,p}x_3]$ dependence, we find from relations (4.12):

$$-\tilde{\rho}_{11}\omega^2\tilde{\Phi}_s - \tilde{\rho}_{12}\omega^2\tilde{\Phi}_f = -Pk_p^2\tilde{\Phi}_s - Qk_p^2\tilde{\Phi}_f, \quad (4.19a)$$

$$-\tilde{\rho}_{22}\omega^2\tilde{\Phi}_f - \tilde{\rho}_{12}\omega^2\tilde{\Phi}_s = -Rk_p^2\tilde{\Phi}_f + Qk_p^2\tilde{\Phi}_s. \quad (4.19b)$$

From the set (4.19), and introducing the inverse squared complex wave velocity $\zeta_p = k_p^2/\omega^2$, the dispersion relation is found:

$$d_2\zeta_p^2 + d_1\zeta_p + d_0 = 0, \quad (4.20)$$

where we have used

$$\begin{aligned} d_2 &= PR - Q^2, \\ d_1 &= -(P\tilde{\rho}_{22} + R\tilde{\rho}_{11} - 2Q\tilde{\rho}_{12}), \\ d_0 &= \tilde{\rho}_{11}\tilde{\rho}_{22} - \tilde{\rho}_{12}^2. \end{aligned} \quad (4.21)$$

We note that d_2 can also be written as $\phi^2 K_f (K_b + \frac{4}{3}G)/\beta$, where $\beta = \phi + K_f/K_a(1 - \phi - K_b/K_a)$ as defined previously. Equation (4.20) has two complex roots:

$$\zeta_{\{p_1, p_2\}} = \frac{-d_1 \pm d_1 (1 - 4d_0 d_2 / d_1^2)^{1/2}}{2d_2}, \quad (4.22)$$

and therefore we have two damped compressional waves. The properties of the two waves were illustrated by Biot (1956), who showed that the fluid and skeletal velocities have the same sign for one root, and have the opposite sign for the other root. This means that there is one wave in which fluid and skeletal velocities are in phase, and another in which they are in opposite phase. In the same paper, it is also shown that the wave which propagates fastest has in-phase fluid and skeletal velocities, whereas the slower propagating wave has those velocities in opposite phases. As a matter of definition, the wave which propagates fastest will be denoted as the fast wave (denoted by subscript p_1), while the other one will be denoted as the slow wave (denoted by subscript p_2). It is conceivable that the slow wave is damped more strongly than the fast wave, because the out-of-phase character of the slow wave mode represents a highly effective dissipation mechanism.

Furthermore, it is worth noting that Equation (4.19) for $\tilde{\Phi}_f$ and $\tilde{\Phi}_s$ implies a simple linear relationship between fast and slow components of the corresponding fluid and solid displacement amplitudes, \tilde{U} and \tilde{u} . It can be seen that

$$\Gamma_{\{p_1, p_2\}} = \frac{\tilde{U}}{\tilde{u}} = \frac{Q\zeta_{\{p_1, p_2\}} - \tilde{\rho}_{12}}{-R\zeta_{\{p_1, p_2\}} + \tilde{\rho}_{22}} = \frac{-P\zeta_{\{p_1, p_2\}} + \tilde{\rho}_{11}}{Q\zeta_{\{p_1, p_2\}} - \tilde{\rho}_{12}}. \quad (4.23)$$

Low- and high-frequency limits

We will now discuss some limiting cases for the complex wave velocities as formulated in Equation (4.22). We start with the low-frequency limit for which the viscous effects in the fluid dominate the inertial effects. From the definitions in Equation (4.21) we note that the lowest order term of $(d_0 d_2)/d_1^2$ is proportional to ω . Following this, we replace the square root in Equation (4.22) by the first order term of the Taylor series expansion:

$$\sqrt{1 - \frac{4d_0 d_2}{d_1^2}} \approx 1 - \frac{2d_0 d_2}{d_1^2}. \quad (4.24)$$

In this way, we arrive at

$$\lim_{\omega \rightarrow 0} \zeta_{\{p_1, p_2\}} = \frac{-d_1 \pm d_1 (1 - 2d_0 d_2/d_1^2)}{2d_2}, \quad (4.25)$$

Now it can easily be found that $\lim_{\omega \rightarrow 0} \zeta_{p_1} = -d_0/d_1$, which means that this fast wave becomes propagatory in the low-frequency limit with a real-valued velocity equal to $\sqrt{H/\rho}$, where

$$H = P + R + 2Q = \frac{\phi K_b (1 - \frac{K_f}{K_s}) + K_f (1 - \frac{K_b}{K_s})}{\phi + \frac{K_f}{K_s} (1 - \phi - \frac{K_b}{K_s})} + \frac{4}{3}G. \quad (4.26)$$

This can also be written as

$$H = K_b + \frac{4}{3}G + \frac{K_f (1 - \frac{K_b}{K_s})^2}{\phi + \frac{K_f}{K_s} (1 - \phi - \frac{K_b}{K_s})}. \quad (4.27)$$

This effective modulus H was originally derived by Gassmann (1951) in an article which predates the Biot theory and therefore this low-frequency limit is often called the Biot-Gassmann result. In Equation (4.23) we have found the fluid-solid displacement amplitude ratio \tilde{U}/\tilde{u} . For this propagatory wave it can be seen that $\lim_{\omega \rightarrow 0} (\tilde{U}/\tilde{u}) = 1$, which implies that the fluid motion is locked-on to the solid's.

The slow wave is strongly damped at low frequencies because of the fluid viscosity, since it involves a relative motion of fluid and solid. We find that

$$\lim_{\omega \rightarrow 0} \zeta_{p_2} = -\frac{d_1}{d_2} + \frac{d_0}{d_1} = -\frac{d_1}{d_2} = -\frac{ib_0}{\omega} \frac{(P + R + 2Q)}{(PR - Q^2)}. \quad (4.28)$$

Apparently this slow wave is described by a diffusion equation rather than a wave equation in the low-frequency limit, because ζ_{p2} is the solution of the diffusion equation

$$c_D \partial_i^2 \xi = \partial_t \xi, \quad (4.29)$$

where ξ can be any relevant variable (p , ρ_f , v , etc.) and

$$c_D = \frac{PR - Q^2}{b_0(P + R + 2Q)}. \quad (4.30)$$

Substitution of ζ_2 in Equation (4.23) yields

$$\lim_{\omega \rightarrow 0} \frac{\tilde{U}}{\tilde{u}} = -\frac{Q + P}{Q + R}. \quad (4.31)$$

This diffusive behaviour in the low-frequency limit was studied previously by Chandler (1981) and Chandler and Johnson (1981). Obviously, this wave has an infinite travel time in the low-frequency limit.

In the high-frequency limit we find from relations (4.21) that

$$\begin{aligned} \lim_{\omega \rightarrow \infty} d_2 &= PR - Q^2, \\ \lim_{\omega \rightarrow \infty} d_1 &= -(P\rho_{22} + R\rho_{11} - 2Q\rho_{12}), \\ \lim_{\omega \rightarrow \infty} d_0 &= \rho_{11}\rho_{22} - \rho_{12}^2. \end{aligned} \quad (4.32)$$

The density terms all take on real values and consequently both waves become propagatory. Also for real-valued density terms the inverse squared velocities are defined in Equation (4.22).

Acoustic bulk properties

The complex wavenumbers k_j for $j = p1, p2$ are related to the acoustic bulk properties of the material, phase speed $\omega/|\Re\{k_j\}|$, attenuation $\Im m\{k_j\}$, and specific attenuation $1/Q$. We may define the specific attenuation parameter $1/Q$ as

$$\frac{1}{Q} = \frac{2|\Im m\{k_j\}|}{|\Re\{k_j\}|}. \quad (4.33)$$

The results of numerical computations for the phase speed and the (specific) attenuation of both compressional waves are given in Figures (4.1)-(4.3). Also the shear wave is plotted, but this wave is discussed in the following

section. All curves are computed with (solid lines) and without (dashed lines) dynamic permeability (see Section 3.4). The input parameters used for the calculations are listed in Table 4.1. The 'constrained modulus' K_p is defined as $K_b + 4G/3$. All these input parameters refer to Nivelsteiner sandstone which is used for our high-frequency experiments as discussed in Chapter 7. It is assumed that the sandstone is fully water-saturated.

constrained modulus	K_p	26.1	GPa
shear modulus	G	10.14	GPa
fluid bulk modulus	K_f	2.22	GPa
solid density	ρ_s	2760	kg/m ³
fluid density	ρ_f	1000	kg/m ³
porosity	ϕ	24	%
tortuosity	α_∞	2.5	
permeability	k_0	10×10^{-12}	m ²
fluid viscosity	η	0.001	Pa·s

Table 4.1: *Parameter values for water-saturated Nivelsteiner sandstone*

The following points emerge from these computations for the compressional waves:

- The fast wave speed is frequency-independent. The slow wave speed shows the transition from a low-frequency diffusion phenomenon to a high-frequency propagatory wave.
- From calculations for various sets of input parameters we found that the phase speed of the fast wave is mainly influenced by the solid phase properties (e.g. elastic moduli), whereas the production properties (e.g. permeability, tortuosity) dominate the slow wave propagation.
- The attenuation is frequency-dependent for both compressional waves and the attenuation of the slow wave is much higher than the attenuation of the fast wave. This is a result of the out-of-phase character of the slow wave which represents a highly effective dissipation mechanism.
- The influence of the dynamic permeability is largely limited to the attenuation coefficients. This is in accordance with previous results

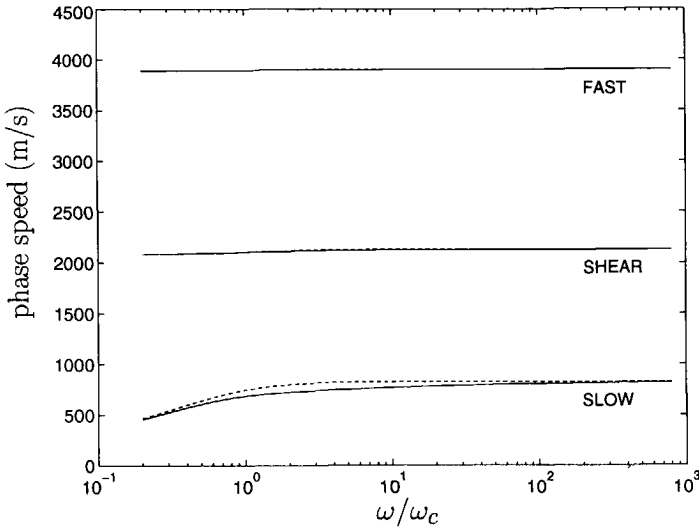


Figure 4.1: The phase speed for the fast wave, shear wave, and slow wave in the Nivelsteiner sandstone. The solid curves indicate the calculations with dynamic permeability, and the dashed curves indicate the calculations involving steady-state permeability.

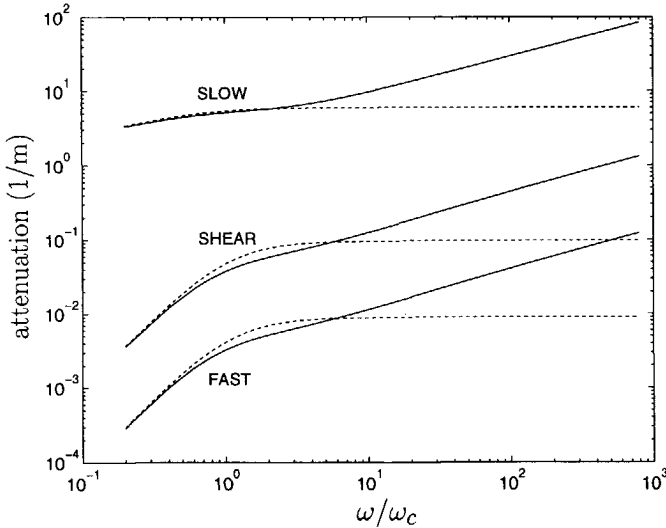


Figure 4.2: The attenuation for the fast wave, shear wave, and slow wave in the Nivelsteiner sandstone. Legend identical to Figure 4.1.

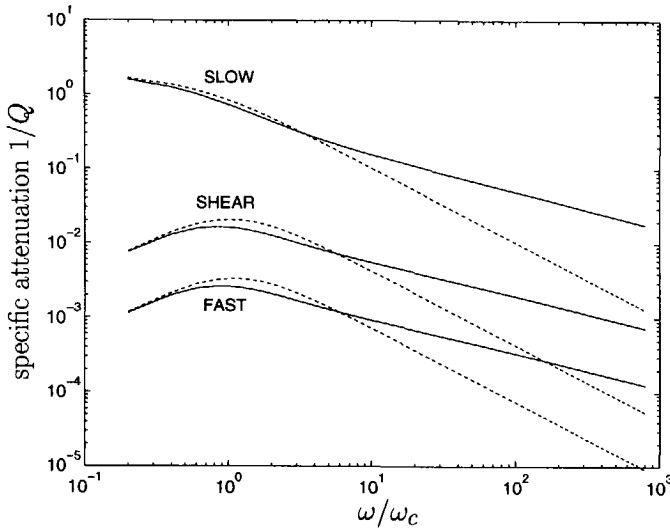


Figure 4.3: *The specific attenuation $1/Q$ for the fast wave, shear wave, and slow wave in the Nivelsteiner sandstone. Legend identical to Figure 4.1.*

by Van der Grinten et al. (1987). The dynamic permeability strongly influences the attenuation behaviour at higher frequencies.

- The specific attenuation $1/Q$ peaks in the vicinity of the crossover frequency ω_c . For this specific case, the crossover frequency ($\omega_c/2\pi$) is equal to 1.3 kHz.

4.4 Shear wave velocity

By a transformation to the (k_1, ω) domain and assuming an $\exp[ik_{3,s}x_3]$ dependence, we find from relations (4.13):

$$-\tilde{\rho}_{11}\omega^2\tilde{\Psi}_s - \tilde{\rho}_{12}\omega^2\tilde{\Psi}_f = -Gk_s^2\tilde{\Psi}_s, \quad (4.34a)$$

$$-\tilde{\rho}_{22}\omega^2\tilde{\Psi}_f - \tilde{\rho}_{12}\omega^2\tilde{\Psi}_s = 0, \quad (4.34b)$$

From the set (4.34), the inverse squared complex wave velocity $\zeta_s = k_s^2/\omega^2$ follows as

$$\zeta_s = \frac{\tilde{\rho}_{11}\tilde{\rho}_{22} - \tilde{\rho}_{12}^2}{G\tilde{\rho}_{22}}. \quad (4.35)$$

Similar to the longitudinal case, from the set (4.34) not only ζ_s can be found, but also the shear fluid-solid displacement amplitude ratio

$$\Gamma_s = \frac{\tilde{U}}{\tilde{u}} = \frac{-\tilde{\rho}_{12}}{\tilde{\rho}_{22}} = \frac{-G\zeta_s + \tilde{\rho}_{11}}{-\tilde{\rho}_{12}}. \quad (4.36)$$

Low- and high-frequency limits

From the inverse squared complex velocity of the shear wave as formulated in Equation (4.35), the low frequency limit real-valued velocity follows as $\sqrt{G/\rho}$. Furthermore, it can then be seen that $\lim_{\omega \rightarrow 0} \tilde{U}/\tilde{u} = 1$, which again implies that the fluid motion is locked-on to the solid's. For the shear wave in the high-frequency limit the density terms in Equation (4.35) take on real values. Furthermore, we have the fluid-solid displacement amplitude ratio $\lim_{\omega \rightarrow \infty} \tilde{U}/\tilde{u} = -\rho_{12}/\rho_{22}$.

Acoustic bulk properties

Finally, results for acoustic bulk property calculations of the shear wave are given in Figures (4.1)-(4.3). The almost frequency-independent phase speed values are smaller than the values for the fast wave and greater than values for the slow wave. The attenuation of the shear wave in its turn is greater than the attenuation of the fast wave but smaller than that of the slow wave. The frequency-dependence of the shear wave attenuation shows the same behaviour as the compressional wave attenuation.

4.5 Effect of grain compressibility

It is possible to investigate the grain compressibility effects on the high-frequency limit of the compressional wave velocities. The density terms in the expressions for these wave velocities are given in Equations (4.32). In general, the wave velocities are a function of the bulk moduli K_b , K_s , and K_f . Other parameters are not considered in this section. In Equations (2.36) we derived relations for the generalized elastic parameters Q , R , and P , where $P = A + 2G$, as a function of the bulk moduli. To investigate the compressional wave velocities in the high-frequency limit as a function of the grain compressibility K_s they are normalized by the velocities for the case of incompressible grains ($K_b/K_s \ll 1$ and $K_f/K_s \ll 1$). For this case,

relations for the generalized elastic parameters as a function of measurable quantities are given in Equation (2.37). The input parameter values for our calculations are given in Table 4.1. For the case of incompressible grains, the fast compressional wave velocity in this sandstone equals 3902 m/s. The slow compressional wave velocity equals 824 m/s. The normalized wave velocities for both the fast and slow compressional wave as a function of K_s/K_b are depicted in Figure (4.4). Note that the calculations are limited by the relation $(1 - \phi)K_s > K_b$ (Verruijt, 1982), which was discussed in Chapter 2. As we may expect, the normalized velocities tend to 1 in the limit for $K_s \rightarrow \infty$ (incompressible grains). For increasing compressibility of the grains (decreasing K_s) we note that the normalized fast wave velocity becomes less than 1. This is because the fast wave is mainly governed by the properties of the solid phase of the porous medium. From Figure (4.4), we also note that the normalized slow wave action is diametrically opposed to this. Finally, for relevant K_s/K_b values the normalized velocities vary by less than 10%.

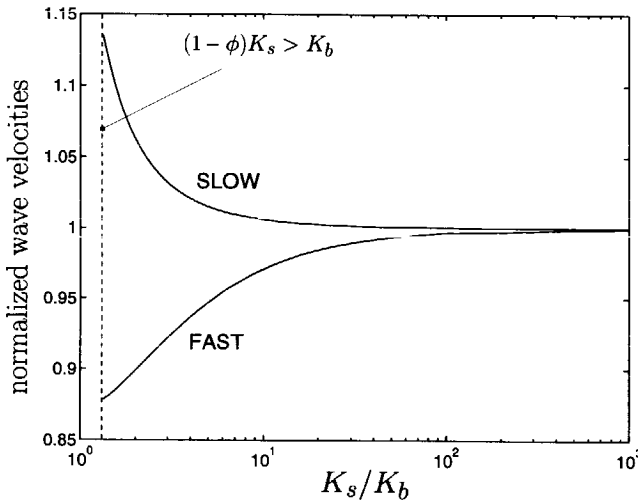


Figure 4.4: High-frequency values of the normalized fast and slow wave velocities. Parameter values are listed in Table 4.1.

Chapter 5

Waves and interfaces

5.1 Introduction

In this chapter we discuss the frequency-dependent transmission and reflection coefficients of plane waves at oblique incidence on a plane interface between two media. One of the media is a non-viscous fluid and the other is a dissipative water-saturated porous medium. Two general cases of wave type conversion are investigated: (I) The incident wave in the fluid generates one reflected compressional wave in the fluid and three transmitted bulk waves in the porous medium, and (II) an incident wave in the porous medium generates three reflected bulk waves in the porous medium and one transmitted compressional wave in the fluid. Results of both cases can be used to calculate the total transmission coefficient of all three bulk waves through a layer of porous medium immersed in fluid. Such a transmission configuration is used for our acoustic experiments through slabs of water-saturated porous material immersed in a water-filled tank (see Chapter 7).

5.2 Solutions of the field quantities

The basic equations that govern the acoustic wave motion in a fluid-saturated porous medium were described in the previous chapter. We found that in general the compressional wave potentials $\tilde{\Phi}_s$ and $\tilde{\Phi}_f$ in the solid and fluid

phase of the porous medium can be written as follows:

$$\begin{aligned} \tilde{\Phi}_s(k_1, x_3, \omega) = & \varphi_{p1}^+ \exp[ik_{3,p1}x_3] + \varphi_{p1}^- \exp[-ik_{3,p1}x_3] + \\ & \varphi_{p2}^+ \exp[ik_{3,p2}x_3] + \varphi_{p2}^- \exp[-ik_{3,p2}x_3], \end{aligned} \quad (5.1a)$$

$$\begin{aligned} \tilde{\Phi}_f(k_1, x_3, \omega) = & \Gamma_{p1}\varphi_{p1}^+ \exp[ik_{3,p1}x_3] + \Gamma_{p1}\varphi_{p1}^- \exp[-ik_{3,p1}x_3] + \\ & \Gamma_{p2}\varphi_{p2}^+ \exp[ik_{3,p2}x_3] + \Gamma_{p2}\varphi_{p2}^- \exp[-ik_{3,p2}x_3]. \end{aligned} \quad (5.1b)$$

For the shear wave potentials $\tilde{\Psi}_s$ and $\tilde{\Psi}_f$ we have

$$\tilde{\Psi}_s(k_1, x_3, \omega) = \psi_s^+ \exp[ik_{3,s}x_3] + \psi_s^- \exp[-ik_{3,s}x_3]. \quad (5.2a)$$

$$\tilde{\Psi}_f(k_1, x_3, \omega) = \Gamma_s\psi_s^+ \exp[ik_{3,s}x_3] + \Gamma_s\psi_s^- \exp[-ik_{3,s}x_3]. \quad (5.2b)$$

The fluid and solid displacement amplitude ratios Γ_{p1} for the fast wave, Γ_{p2} for the slow wave, and Γ_s for the shear wave, are given in Equation (4.23) and (4.36), respectively. The wave potentials in the solid are defined from the solid displacements in Equation (4.14), and the potentials in the fluid are defined from the fluid displacements in Equation (4.15). Combining Equations (5.1) and (5.2) means that all field quantities (pressure, stress, and particle velocities) in a porous medium consist of a fast and slow compressional wave component, and a shear wave component. All wave types may be downgoing (increasing x_3) with wave type amplitudes $\{\varphi_{p1}^+, \varphi_{p2}^+, \psi_s^+\}$, or upgoing (decreasing x_3) with wave type amplitudes $\{\varphi_{p1}^-, \varphi_{p2}^-, \psi_s^-\}$.

The field quantities $\tilde{\sigma}_{33}$, \tilde{p} , $\tilde{\sigma}_{31}$, \tilde{v}_3 , and \tilde{w}_3 are of particular interest for the study of boundary conditions between a fluid and a porous medium. They are grouped in the velocity-stress vector \mathbf{F}^p :

$$\mathbf{F}^p = \begin{pmatrix} \tilde{\sigma}_{33} \\ \tilde{p} \\ \tilde{\sigma}_{31} \\ \tilde{v}_3 \\ \tilde{w}_3 \end{pmatrix}. \quad (5.3)$$

We are now able to derive expressions for the field quantities appearing in the vector \mathbf{F}^p of the porous medium. We may write

$$\begin{aligned} F_i^p = & T_{i1}^p\varphi_{p1}^+ \exp[ik_{3,p1}x_3] + T_{i4}^p\varphi_{p1}^- \exp[-ik_{3,p1}x_3] + \\ & T_{i2}^p\varphi_{p2}^+ \exp[ik_{3,p2}x_3] + T_{i5}^p\varphi_{p2}^- \exp[-ik_{3,p2}x_3] + \\ & T_{i3}^p\psi_s^+ \exp[ik_{3,s}x_3] + T_{i6}^p\psi_s^- \exp[-ik_{3,s}x_3], \end{aligned} \quad (5.4)$$

for $i = \{1, \dots, 5\}$. The elements of the matrix \mathbf{T}^p can be calculated from the stress-strain relations:

$$-\hat{\sigma}_{33} = 2G\partial_3\hat{u}_3 + (A - \phi^*Q)(\partial_1\hat{u}_1 + \partial_3\hat{u}_3) + (Q - \phi^*R)(\partial_1\hat{U}_1 + \partial_3\hat{U}_3), \quad (5.5)$$

$$-\phi\hat{p} = Q(\partial_1\hat{u}_1 + \partial_3\hat{u}_3) + R(\partial_1\hat{U}_1 + \partial_3\hat{U}_3), \quad (5.6)$$

$$-\hat{\sigma}_{31} = G(\partial_3\hat{u}_1 + \partial_1\hat{u}_3). \quad (5.7)$$

In Equation (5.5), $\phi^* = (1 - \phi)/\phi$. Solutions for the particle velocities follow from:

$$\hat{v}_3 = -i\omega\hat{u}_3, \quad (5.8)$$

$$\hat{w}_3 = -i\omega\hat{U}_3. \quad (5.9)$$

The matrix \mathbf{T}^p can now be written as

$$\mathbf{T}^p = \omega^2 \begin{pmatrix} 2G\gamma_{p1}\gamma_{p1} + \zeta_{p1}\Sigma_{p1} & 2G\gamma_{p2}\gamma_{p2} + \zeta_{p2}\Sigma_{p2} & 2G\alpha_1\gamma_s \\ \zeta_{p1}(Q + R\Gamma_{p1})/\phi & \zeta_{p2}(Q + R\Gamma_{p2})/\phi & 0 \\ 2G\gamma_{p1}\alpha_1 & 2G\gamma_{p2}\alpha_1 & (\alpha_1\alpha_1 - \gamma_s\gamma_s)G \\ \gamma_{p1} & \gamma_{p2} & \alpha_1 \\ \gamma_{p1}\Gamma_{p1} & \gamma_{p2}\Gamma_{p2} & \alpha_1\Gamma_s \end{pmatrix} \quad (5.10)$$

$$\begin{pmatrix} 2G\gamma_{p1}\gamma_{p1} + \zeta_{p1}\Sigma_{p1} & 2G\gamma_{p2}\gamma_{p2} + \zeta_{p2}\Sigma_{p2} & -2G\alpha_1\gamma_s \\ \zeta_{p1}(Q + R\Gamma_{p1})/\phi & \zeta_{p2}(Q + R\Gamma_{p2})/\phi & 0 \\ -2G\gamma_{p1}\alpha_1 & -2G\gamma_{p2}\alpha_1 & (\alpha_1\alpha_1 - \gamma_s\gamma_s)G \\ -\gamma_{p1} & -\gamma_{p2} & \alpha_1 \\ -\gamma_{p1}\Gamma_{p1} & -\gamma_{p2}\Gamma_{p2} & \alpha_1\Gamma_s \end{pmatrix},$$

where

$$\Sigma_{p1,p2} = A - \phi^*Q + \Gamma_{p1,p2}(Q - \phi^*R). \quad (5.11)$$

Here we have introduced the horizontal slowness α_1 and the vertical slowness γ_j , defined as follows (Aki and Richards, 1980):

$$\alpha_1 = \frac{k_1}{\omega}, \quad (5.12)$$

$$\gamma_{p1} = \frac{k_{3,p1}}{\omega} = \left(\zeta_{p1} - \alpha_1^2\right)^{1/2}, \quad (5.13)$$

$$\gamma_{p2} = \frac{k_{3,p2}}{\omega} = \left(\zeta_{p2} - \alpha_1^2 \right)^{1/2}, \quad (5.14)$$

$$\gamma_s = \frac{k_{3,s}}{\omega} = \left(\zeta_s - \alpha_1^2 \right)^{1/2}, \quad (5.15)$$

in which the inverse squared velocities ζ_{p1} , ζ_{p2} and ζ_s are given by Equations (4.22) and (4.35). Due to the positioning of the elements of \mathbf{T}^p in Equation (5.4), the columns of \mathbf{T}^p represent the downgoing fast wave, slow wave, shear wave, and upgoing fast wave, slow wave and shear wave, respectively.

In a similar way, we may define a fluid potential $\tilde{\Phi}$ in the non-viscous fluid. It can be written as follows:

$$\tilde{\Phi}(k_1, x_3, \omega) = \varphi^+ \exp[ik_{3,f}x_3] + \varphi^- \exp[-ik_{3,f}x_3], \quad (5.16)$$

in which we consider a downgoing wave with amplitude φ^+ and an upgoing wave with amplitude φ^- . The fluid potential $\tilde{\Phi}$ is defined from the non-viscous fluid displacement

$$\hat{u}_3^f = \partial_3 \tilde{\Phi}. \quad (5.17)$$

For the study of boundary conditions the field quantities \tilde{p}^f and \tilde{v}_3^f , grouped in the vector $\mathbf{F}^f = (\tilde{p}^f, \tilde{v}_3^f)^T$, are of particular interest. We may write

$$F_i^f = T_{i1}^f \varphi^+ \exp[ik_{3,f}x_3] + T_{i2}^f \varphi^- \exp[-ik_{3,f}x_3]. \quad (5.18)$$

for $i = \{1, 2\}$. Using the non-viscous fluid equations as given in Equations (A.1) and (A.3), the matrix \mathbf{T}^f can be written as

$$\mathbf{T}^f = \omega^2 \begin{pmatrix} \rho_f & \rho_f \\ \gamma_f & -\gamma_f \end{pmatrix} \quad (5.19)$$

in which use has been made of $\alpha_1 = k_1/\omega$ and $\gamma_f = k_{3,f}/\omega$. The vertical slowness γ_f is given by (Aki and Richards, 1980)

$$\gamma_f = \left(\frac{1}{c_f^2} - \alpha_1^2 \right)^{1/2}, \quad (5.20)$$

with $c_f = (K_f/\rho_f)^{1/2}$, representing the non-viscous fluid wave velocity.

5.3 Reflection and transmission coefficients

We will now discuss two configurations to investigate the two general cases of wave type conversions. We consider a two-dimensional situation in the X_1X_3 -plane of an orthogonal Cartesian reference frame with origin O . We chose the interface between the external fluid and the porous medium to coincide with the horizontal axis x_1 . In this way, x_3 is chosen normal to this interface and points vertically downwards. In Figure (5.1) we have plotted the configuration for both cases I and II. For case I, a downgoing

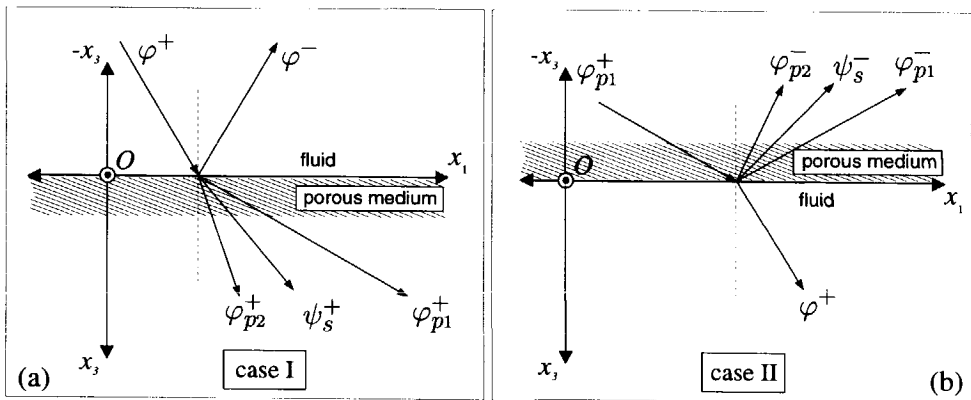


Figure 5.1: *Schematic of the two-media configurations for cases I and II wave type conversions.*

incident compressional wave in the fluid with wave amplitude φ^+ generates a reflected compressional wave at the fluid/porous medium interface with amplitude φ^- , a transmitted fast wave with amplitude φ_{p1}^+ , a transmitted shear wave with amplitude ψ_s^+ , and a transmitted slow wave with amplitude φ_{p2}^+ . Please note that we consider a semi-infinite porous sample, so there are no reflected waves within the porous sample. For case II, a downgoing incident fast wave in the porous medium generates three reflected bulk waves in the porous medium with wave amplitudes $\{\varphi_{p1}^-, \psi_s^-, \varphi_{p2}^-\}$ and one transmitted compressional wave in the fluid part of the configuration with amplitude φ^+ . We only plotted the wave type conversions of the fast wave. Evidently, similar wave type conversions appear for incident shear waves and slow waves.

Boundary conditions at the interface between the external fluid and

a fluid-saturated porous medium are in accordance with Deresiewicz and Skalak (1963). At such an interface the pore fluid pressure \tilde{p} is equal to the external fluid pressure. This means

$$\tilde{p} = \tilde{p}^f. \tag{5.21}$$

Furthermore, we have the intergranular stress boundary condition

$$\tilde{\sigma}_{33} = 0, \tag{5.22}$$

$$\tilde{\sigma}_{31} = 0. \tag{5.23}$$

Mass conservation for the fluid over a moving boundary yields:

$$(1 - \phi)\tilde{v}_3 + \phi\tilde{w}_3 = \tilde{v}_3^f. \tag{5.24}$$

For the interface boundary conditions in matrix notation for case I we find

$$\begin{pmatrix} 0 & T_{11}^p & T_{12}^p & T_{13}^p \\ -\rho_f & T_{21}^p & T_{22}^p & T_{23}^p \\ 0 & T_{31}^p & T_{32}^p & T_{33}^p \\ \gamma_f & T_{*1}^p & T_{*2}^p & T_{*3}^p \end{pmatrix} \begin{pmatrix} \varphi^- \\ \varphi_{p1}^+ \\ \varphi_{p2}^+ \\ \psi_s^+ \end{pmatrix} = \begin{pmatrix} 0 \\ \rho_f \\ 0 \\ \gamma_f \end{pmatrix} \varphi^+, \tag{5.25}$$

where

$$T_{*j}^p = (1 - \phi)T_{4j}^p + \phi T_{5j}^p, \text{ for } j = \{1..6\}. \tag{5.26}$$

From Equation (5.25), the reflection coefficient and transmission coefficients follow as

$$\begin{pmatrix} R_{p,p} \\ T_{p1,p} \\ T_{p2,p} \\ T_{s,p} \end{pmatrix} = \begin{pmatrix} \varphi^-/\varphi^+ \\ \varphi_{p1}^+/\varphi^+ \\ \varphi_{p2}^+/\varphi^+ \\ \psi_s^+/\varphi^+ \end{pmatrix} = \begin{pmatrix} 0 & T_{11}^p & T_{12}^p & T_{13}^p \\ -\rho_f & T_{21}^p & T_{22}^p & T_{23}^p \\ 0 & T_{31}^p & T_{32}^p & T_{33}^p \\ \gamma_f & T_{*1}^p & T_{*2}^p & T_{*3}^p \end{pmatrix}^{-1} \begin{pmatrix} 0 \\ \rho_f \\ 0 \\ \gamma_f \end{pmatrix} \tag{5.27}$$

The same approach can be used for the derivation of the reflection and transmission coefficients for case II. In Figure (5.1b) we only plotted the wave type conversions for the fast wave. The interface boundary conditions in matrix notation for this incident fast wave in case II are

$$\begin{pmatrix} T_{11}^p \\ T_{21}^p \\ T_{31}^p \\ T_{*1}^p \end{pmatrix} \varphi_{p1}^+ + \begin{pmatrix} 0 & T_{14}^p & T_{15}^p & T_{16}^p \\ -\rho_f & T_{24}^p & T_{25}^p & T_{26}^p \\ 0 & T_{34}^p & T_{35}^p & T_{36}^p \\ -\gamma_f & T_{*4}^p & T_{*5}^p & T_{*6}^p \end{pmatrix} \begin{pmatrix} \varphi_t^+ \\ \varphi_{p1}^- \\ \varphi_{p2}^- \\ \psi_s^- \end{pmatrix} = \mathbf{0}. \tag{5.28}$$

The same set of equations can be written for an incident shear wave and slow wave. Combining these expressions, the reflection and transmission coefficients follow as

$$\begin{pmatrix} T_{p,p1} & T_{p,p2} & T_{p,s} \\ R_{p1,p1} & R_{p1,p2} & R_{p1,s} \\ R_{p2,p1} & R_{p2,p2} & R_{p2,s} \\ R_{s,p1} & R_{s,p2} & R_{s,s} \end{pmatrix} = \begin{pmatrix} \varphi_t^+/\varphi_{p1}^+ & \varphi_t^+/\varphi_{p2}^+ & \varphi_t^+/\psi_s^+ \\ \varphi_{p1}^-/\varphi_{p1}^+ & \varphi_{p1}^-/\varphi_{p2}^+ & \varphi_{p1}^-/\psi_s^+ \\ \varphi_{p2}^-/\varphi_{p1}^+ & \varphi_{p2}^-/\varphi_{p2}^+ & \varphi_{p2}^-/\psi_s^+ \\ \psi_s^-/\varphi_{p1}^+ & \psi_s^-/\varphi_{p2}^+ & \psi_s^-/\psi_s^+ \end{pmatrix} = \quad (5.29)$$

$$- \begin{pmatrix} 0 & T_{14}^p & T_{15}^p & T_{16}^p \\ -\rho_f & T_{24}^p & T_{25}^p & T_{26}^p \\ 0 & T_{34}^p & T_{35}^p & T_{36}^p \\ -\gamma_f & T_{*4}^p & T_{*5}^p & T_{*6}^p \end{pmatrix}^{-1} \begin{pmatrix} T_{11}^p & T_{12}^p & T_{13}^p \\ T_{21}^p & T_{22}^p & T_{23}^p \\ T_{31}^p & T_{32}^p & T_{33}^p \\ T_{*1}^p & T_{*2}^p & T_{*3}^p \end{pmatrix}$$

The transmission and reflection coefficients in Equations (5.27) and (5.29) depend on the frequency and the angle of incidence. Frequency dependence follows from the definitions of the density terms ($\tilde{\rho}_{11}$, $\tilde{\rho}_{22}$, $\tilde{\rho}_{12}$, and $\tilde{\rho}$) and the inverse squared velocities (ζ_{p1} , ζ_{p2} and ζ_s) as defined in Chapter 4. The angle dependence is introduced by means of the horizontal slowness α_1 . According to Snell's Law this horizontal slowness is identical for all bulk waves under consideration. For case I, for example, we may write:

$$\alpha_1 = \sqrt{|\zeta_f|} \sin \theta_f = \sqrt{|\zeta_j|} \sin \theta_j, \quad (5.30)$$

where $\zeta_f = 1/c_f^2$ and for j referring to $\{p1, p2, s\}$. Furthermore, θ_f is the angle of incidence, and θ_j the angles of transmission for the different types of bulk waves. The vertical slownesses are not equal for the different waves. We found that, if $\alpha_1 < 1/\sqrt{|\zeta_j|}$,

$$\gamma_j = (\zeta_j - \alpha_1^2)^{1/2}, \quad (5.31)$$

for $j = \{f, p1, p2, s\}$. On the other hand, if $\alpha_1 > 1/\sqrt{|\zeta_j|}$, we cannot allow the bulk wave to grow exponentially with increasing x_3 and therefore it follows that

$$\gamma_j = i(\alpha_1^2 - \zeta_j)^{1/2}, \quad (5.32)$$

which are called inhomogeneous waves.

5.4 Numerical results

In this section we will show the numerical results of the absolute values of the complex reflection and transmission coefficients derived in Equations (5.27) and (5.29). The parameters used for the calculations are listed in Table 5.1:

constrained modulus	K_p	12	GPa
shear modulus	G	4	GPa
solid bulk modulus	K_s	36.6	GPa
fluid bulk modulus	K_f	2.22	GPa
solid density	ρ_s	2640	kg/m ³
fluid density	ρ_f	1000	kg/m ³
fluid viscosity	η	0.001	Pa·s
porosity	ϕ	30	%
tortuosity	α_∞	2.0	
permeability	k_0	10×10^{-12}	m ²

Table 5.1: *Input parameter values for a water-saturated porous medium*

All curves are plotted for the high-frequency limit (solid line) and for the rollover frequency $\omega_c = (\eta\phi)/(\rho k_0 \alpha_\infty) = 1.5 \times 10^4$ rad/s (dashed line). This corresponds to $f = 2387$ Hz.

Case I

For case I (see Figure 5.1a), we have plotted the reflection and transmission coefficients for an incident compressional wave in the fluid. The reflection coefficient $R_{p,p}$ of this compressional wave is shown in Figure (5.2). The transmission coefficients are shown in Figure (5.3). Because the fast wave velocity for the set of input parameters is greater than the incident fluid wave velocity there is a critical angle of incidence of about 29.5° . For an angle of incidence of 90° , the transmission coefficients are zero and no energy is transmitted. For normal incidence, we notice that the shear wave is not generated and that the fast wave transmission coefficient is much greater than the slow wave transmission coefficient. For increasing angles of incidence, the fast wave disappears at 29.5° , and the shear and slow wave coefficients show minimum values at this critical angle. The shear wave transmission coefficient even becomes zero for the high-frequency limit. Subsequently,

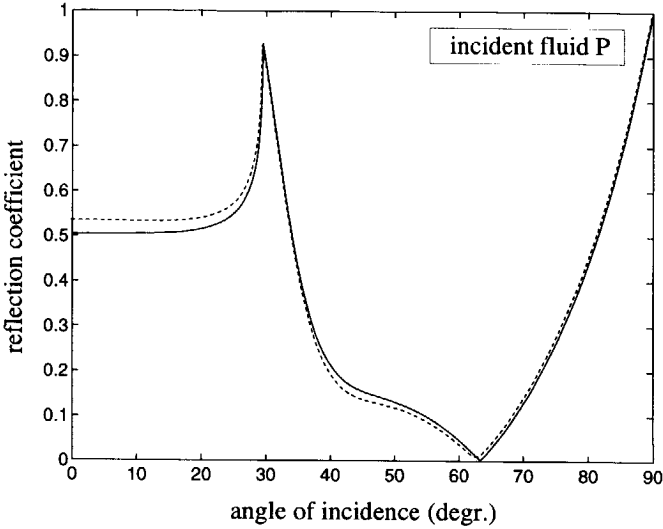


Figure 5.2: Reflection coefficient $R_{p,p}$ for an incident compressional wave in the fluid. The solid line represents the high-frequency limit and the dashed line the rollover frequency.

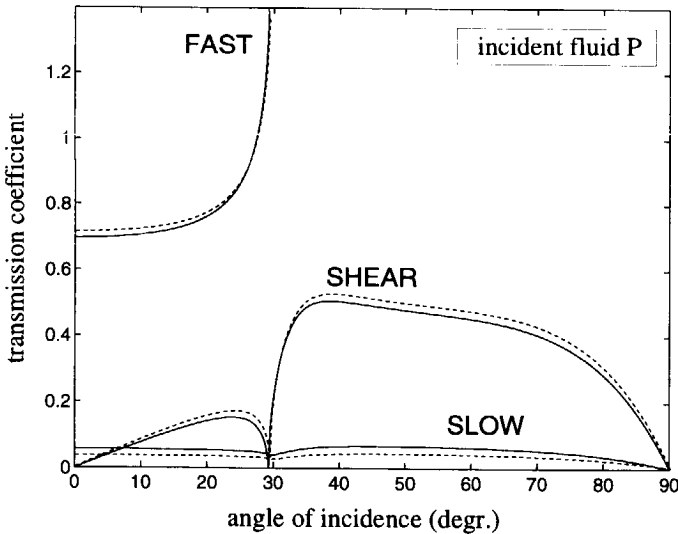


Figure 5.3: Transmission coefficients $T_{p1,p}$ (FAST), $T_{p2,p}$ (SLOW), and $T_{s,p}$ (SHEAR) for an incident compressional wave in the fluid. The solid line represents the high-frequency limit and the dashed line the rollover frequency.

both coefficients reach their highest values around 40° . For all transmission coefficients, there is only a small difference between results for the rollover frequency ω_c and the high-frequency limit values.

Case II

For case II (see Figure 5.1b), we have plotted reflection and transmission coefficients for incident bulk waves in the porous medium. For an incident fast wave the results for the reflection coefficients of the fast wave R_{p_1,p_1} , the slow wave R_{p_2,p_1} , and the shear wave R_{s,p_1} are plotted in Figure (5.4). It is

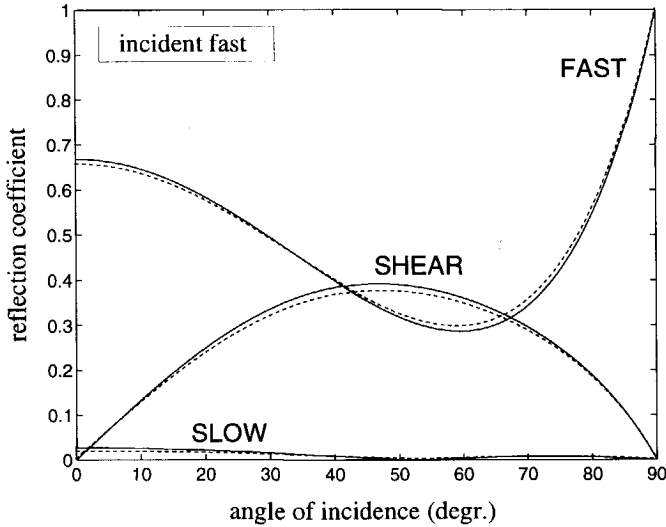


Figure 5.4: Reflection coefficients R_{p_1,p_1} (FAST), R_{p_2,p_1} (SLOW), and R_{s,p_1} (SHEAR) for an incident fast compressional wave. The solid line represents the high-frequency limit and the dashed line the rollover frequency.

clear from these curves that there is no critical angle of incidence, and the reflection coefficients vary smoothly with the angle of incidence. We observe that for an incident fast wave at 90° , the fast wave reflection coefficient is 1 and both other coefficients are 0.

In Figure (5.5) the transmission coefficients for an incident fast wave T_{p,p_1} , an incident slow wave T_{p,p_2} , and an incident shear wave $T_{p,s}$ are shown. The high value and the frequency dependence of the transmission coefficient for an incident slow wave are remarkable compared with the fast wave and

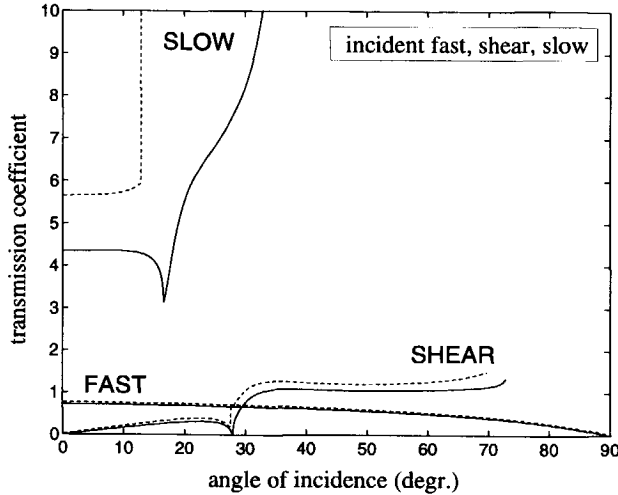


Figure 5.5: Transmission coefficients T_{p,p_1} for the incident fast compressional (FAST), T_{p,p_2} slow compressional (SLOW) and $T_{p,s}$ and shear wave (SHEAR). The solid line represents the high-frequency limit and the dashed line the rollover frequency.

shear wave. Because both the slow wave and the shear wave velocities are less than the velocity of the transmitted fluid wave, they both show a critical angle of incidence. The fast wave coefficient goes to 0 as the angle of incidence approaches 90° , and no energy is transmitted anymore.

Total transmission

The expressions for the transmission coefficients $T_{p_1,p}$, $T_{p_2,p}$, and $T_{s,p}$ of case I, and T_{p,p_1} , T_{p,p_2} , and $T_{p,s}$ of case II may now be combined to calculate the total transmission coefficients of the fast wave T_{p_1} , slow wave T_{p_2} , and shear wave T_s through a fluid-saturated porous layer immersed in fluid (see Figure 5.6). The total transmission coefficients follow as

$$T_{p_1} = T_{p_1,p} T_{p,p_1}, \quad (5.33a)$$

$$T_{p_2} = T_{p_2,p} T_{p,p_2}, \quad (5.33b)$$

$$T_s = T_{s,p} T_{p,s}. \quad (5.33c)$$

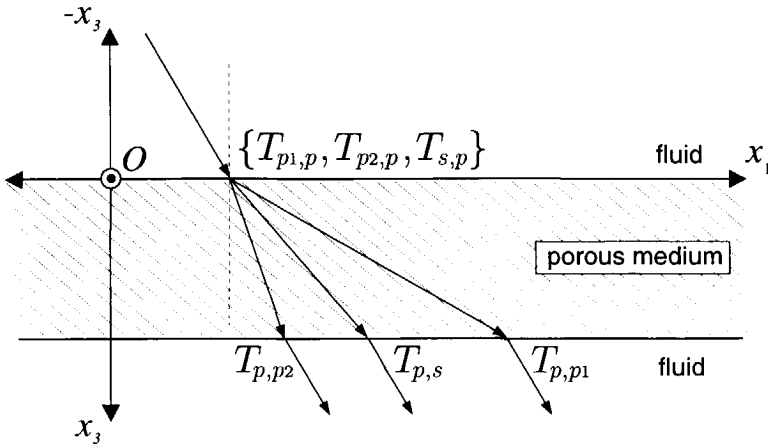


Figure 5.6: Scheme of a transmission configuration showing the various transmission coefficients at both interfaces.

This transmission configuration corresponds with the experimental set-up used for the measurements of acoustic bulk properties as described in Chapter 7. Numerical results of the total transmission coefficients can be verified experimentally in this set-up once the bulk properties in a sample are obtained (Johnson et al., 1994).

Figure (5.7) shows the calculated results. All three wave types are found to show a distinct angular and frequency dependence. At small angles of incidence the fast wave total transmission coefficient is greater than the coefficients for the shear wave and slow wave. It approaches 0 at the critical angle of incidence of about 29.5° . From that point on the shear wave and slow wave coefficients show a sharp increase with increasing angles of incidence. Both for the high-frequency limit (solid line) and for the rollover frequency (dashed line), the shear wave coefficient reaches its highest value at 35° . The slow wave coefficient peaks around 70° in the high-frequency limit and already around 35° at the rollover frequency. Furthermore, it is remarkable that the maximum total transmission values are around 0.5 for all three wave types. Evidently, the attenuation of the each wave type has to be taken into account for comparison of the total transmission coefficients with experiments. In a type of transmission configuration as depicted in Figure (5.6), a time-domain comparison of measured and calculated ultrasonic short duration pulses was done by De Gijzel (1996).

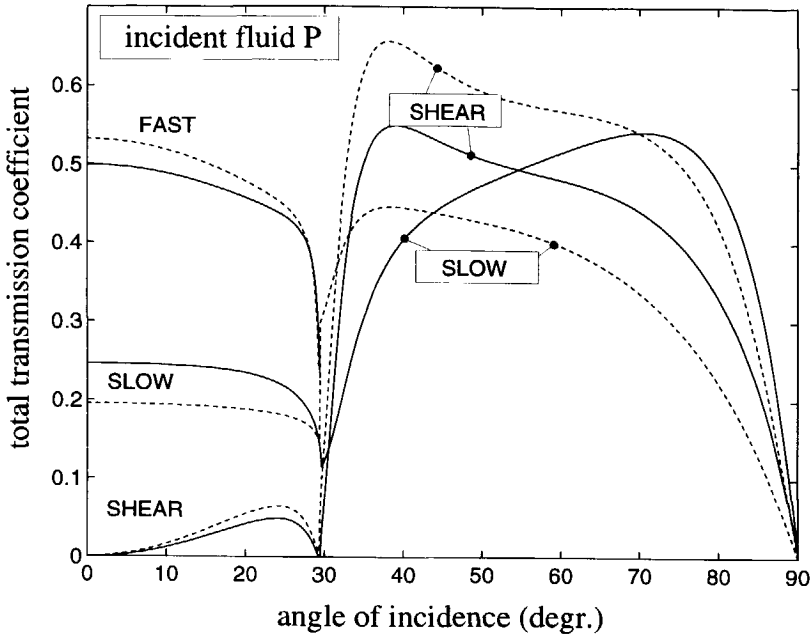


Figure 5.7: Total transmission coefficients T_{p1} (FAST), T_{p2} (SLOW) and T_s (SHEAR) through a fluid-saturated porous layer immersed in fluid. The solid line represents the high-frequency limit and the dashed line the rollover frequency.

Chapter 6

Sample properties and description

6.1 Introduction

In this chapter we will discuss the experimental determination of rock parameters. For our study, we used samples consisting of fused glass beads, permeable ceramic material, and samples cut from natural Nivelsteiner and Bentheimer sandstone. The choice of these specific natural sandstones was motivated by the homogeneity and the simple mineralogical composition of the samples (90-95% quartz). In addition, we also measured the dynamic permeability of samples of glued glass beads and permeable ceramic material. A total of 10 different rock and fluid parameters were considered. The porosity ϕ , density of the grains ρ_s , tortuosity α_∞ , steady-state permeability k_0 , bulk modulus of the permeable rock K_b , and the rock shear modulus G , were all determined by independent laboratory measurements. The fluid density ρ_f , the fluid viscosity η , the bulk modulus of the fluid K_f , and the bulk modulus of the grains K_s , were obtained from textbook values.

6.2 Description of porous materials

Artificial porous material

We used three types of commercially available artificial porous samples. A sample of fused glass beads, labelled as Asst1 (manufactured by Louwers

Hapert, The Netherlands), a permeable ceramic material, labelled as Asst2 (manufactured by Ferro Corporation, New York, USA), and a permeable ceramic material, labelled as Asst3. The first two types of samples were used for velocity and attenuation measurements as described in Chapter 7, and the third type was used for the dynamic permeability measurements. Photomicrographs of all samples are shown in Figure (6.8) at the end of this chapter. These were obtained from thin sections of the samples, which were examined with a Quantimet-570C image analyzer (Leica-Cambridge Ltd.). The grain size of the Asst1 sample is 40-100 μm , of Asst2 50-200 μm , and of Asst3 100-400 μm . The bulk modulus of the grains K_s is taken to be equal to textbook values of the dominant grain material. For the Asst1 sample we have taken that of bulk glass ($K_s = 49.9 \text{ MPa}$). For the Asst2 sample we have taken K_s to be equal to that of quartz ($K_s = 36.6 \text{ MPa}$). The K_s value of the Asst3 sample is not relevant for the dynamic permeability measurements.

Preliminary acoustic measurements on the Asst 1 sample were performed by Geerits and Kelder (1997) but these were restricted to phase velocities and qualitative assessment of frequency-dependent attenuation. Johnson et al. (1994) performed acoustic measurements on ceramic material similar to the Asst2 sample and compared results with the Biot theory. However, they were not able to measure bulk attenuation of the fast and shear wave, since the attenuation factors of these waves are very small. Therefore, we have used samples with a thickness of several centimetres, whereas Johnson et al. (1994) used samples of only 1 cm thickness.

Nivelsteiner sandstone

Nivelsteiner sandstone is found within the Miocene sediments (deposited 10 million years ago) exposed in southern Limburg, The Netherlands, as depicted in Figure (6.1a). The Miocene stratigraphy comprises thin layers of lignite (brown coal) and very pure, well sorted, high porosity quartz sands (Figure 6.1b). The Middle Miocene Nivelsteiner sandstone was deposited within a littoral to very shallow marine / tidal environment (Kuyt, 1973). The sandstone occurs as silicified homogeneous layers (up to a few decimetres in thickness) embedded in 10 to 20 metres of extremely weathered very pure white sands (see Figure 6.1b). The Nivelsteiner sandstone and the weathered unconsolidated sands exhibit a remarkable similarity in textural and mineralogical properties. Samples of this sandstone were obtained from

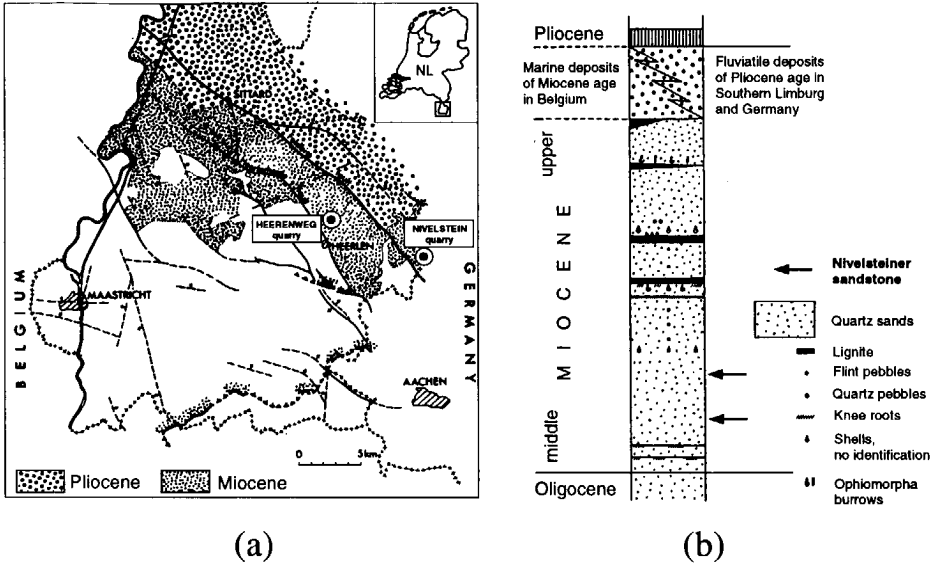


Figure 6.1: (a) Geological map of Southern Limburg, showing the distribution of Miocene and Pliocene formations; Quaternary is omitted. (b) Simple stratigraphic column of the Middle and Upper Miocene deposits (after Kuyl (1973)).

the Nivelstein and Heerenweg quarries. Because of the pureness of the quartz sand, it is still being exploited mainly to be used as a raw material for the crystal glass industry. Photomicrographs of four Nivelsteiner sandstone samples, labelled as Nsst1, Nsst2, Nsst3 and Nsst4, are depicted in Figure (6.9). All samples show a clear predominance of well-sorted quartz grains (over 95%), with a grain size of 150-250 μm . Furthermore, silicification as overgrowth and at grain contacts is a common occurrence. Obviously, the bulk modulus of the grains K_s is taken to be equal to that of quartz ($K_s = 36.6 \text{ MPa}$).

Bentheimer sandstone

Bentheimer sandstone is of the Lower Cretaceous age (deposited 135 million years ago) and crops out near the town of Bentheim in Germany. The regional distribution of this sandstone is shown in Figure (6.2a). This homogeneous sandstone is the reservoir rock of the largest onshore oil field in

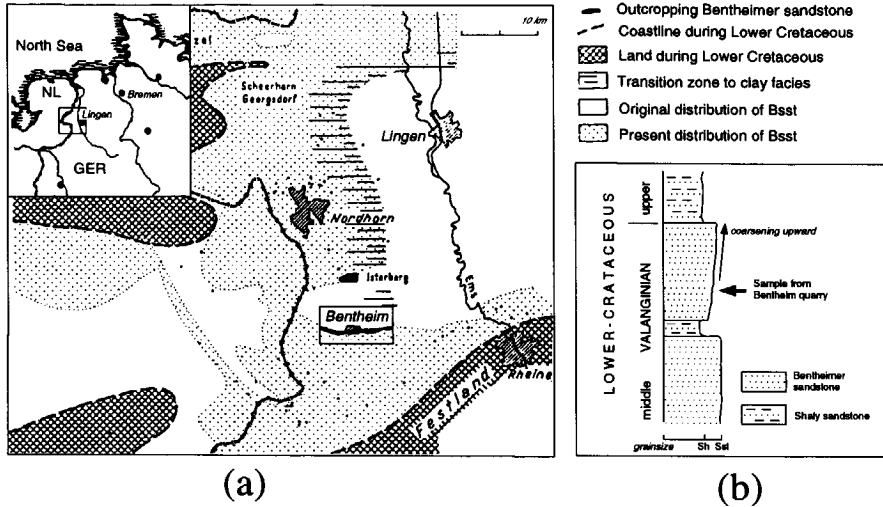


Figure 6.2: (a) Geological map of the Emsland region, showing the original and present distribution of Bsst in this region. (b) Simple stratigraphic profile of the Bsst deposits (after Kemper (1976)).

North West Europe, the Schoonebeek oil field. It is also the reservoir for the large majority of oil fields west of the river Ems in Germany. Bentheimer sandstone is characterized by a vertical coarsening upward profile. This is interpreted as a shallow marine environment of deposition, and is depicted in Figure (6.2b) (Kemper, 1976). A photomicrograph of a Bentheimer sandstone sample, labelled as Bsst, obtained from the Bentheim quarry is shown in Figure (6.8). The grain diameter of the sandstone varies from 150-300 μm . The sandstone consists mainly of quartz (90%-95%), but with a higher percentage of other minerals than the Nivelsteiner sandstone. The image analysis study showed that in addition to quartz overgrowth at the grain contacts, kaolinite (clay) is present in Bentheimer sandstone. This mineral is not present in Nivelsteiner sandstone. Nevertheless, the bulk modulus of the grains K_s is taken to be equal to that of quartz ($K_s = 36.6 \text{ MPa}$).

Before we discuss the experimental determination of the rock parameters for these artificial and natural sandstone samples, we first show the experimental verification of the dynamic permeability model.

6.3 Dynamic permeability

In Chapter 3 we discussed the scaling function for the reduced dynamic permeability of a rigid porous medium, according to Johnson et al. (1987). Charlaix et al. (1988) and Smeulders et al. (1992) took direct measurements of the dynamic permeability of fluid-saturated samples of sintered spherical beads and sintered crushed glass. Johnson et al. (1994) used the acoustic properties of superfluid He II to probe the dynamic permeability of porous media. Direct measurements of dynamic permeability are often hampered by persistent acoustic resonances in the equipment. Here we report new and more accurate experimental results of dynamic permeability measurements (Yazir, 1995). For this, we specifically designed the set-up drawn in Figure (6.3a), which is an improved version of the set-up used by Smeulders et al. (1992). It is called the Dynamic Darcy Cell. A photo of this set-up is shown in Figure (6.5) An oscillating pressure gradient was induced by a vibration

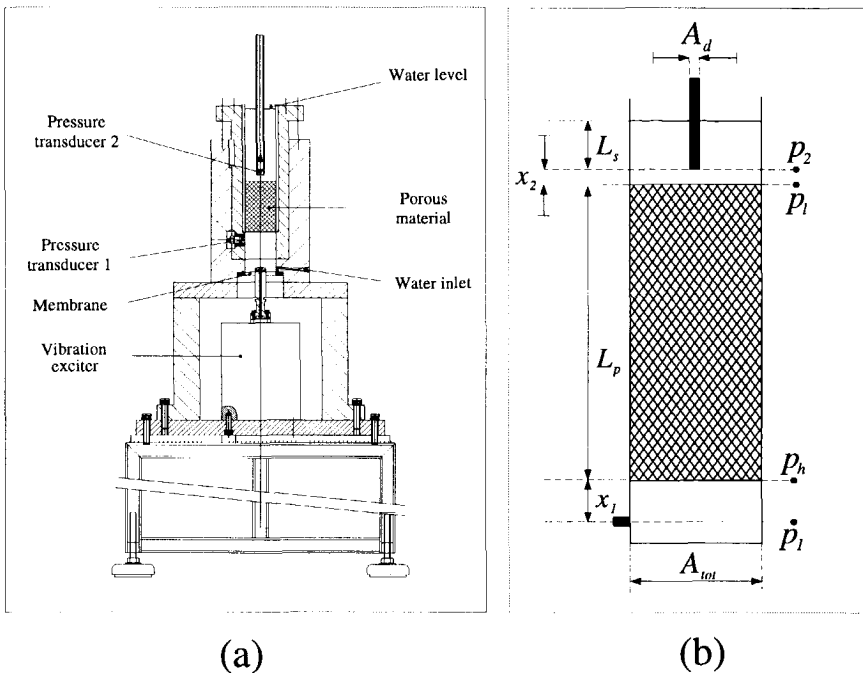


Figure 6.3: (a) *Dynamic Darcy Cell for dynamic permeability measurements.* (b) *Detailed sketch with relevant dimensions of porous material and its surroundings.*

exciter driving a rubber membrane. The vibration exciter, controlled by a power amplifier, induced an oscillating flow in a frequency band ranging from 20 to 200 Hz. Hence the wavelength is much larger than the length of the porous sample (L_p). Therefore, the fluid may be regarded as incompressible. The pressure drop across the porous sample was measured using two piezo-electric transducers. Pressure transducer PT1 (PCB) was installed in the stiff steel body of the set-up, in order to avoid resonance disturbances. Pressure transducer PT2 is identical to PT1 and was mounted on the lower end of a cylindrical Perspex shaft, fixed to a separate steel framework.

For the dynamic permeability measurements the samples were carefully saturated with degassed water. During the measurements the pressure signals of the lower and upper pressure transducers were recorded as an electric charge. The signals were converted by Kistler 5011 amplifiers, to obtain a proportional analogue voltage. This voltage was digitised by a Keithly Das-1400 data acquisition board, which was plugged into a PC. The data-acquisition board was used in combination with a external sample-and-hold unit (SSH-4/A, Keithly) for simultaneous acquisition of both signals, with a maximum delay time of 40 nsec. The software package Viewdac from Keithly controls the data-acquisition by the DAS-1400. Effective noise reduction in the recorded signals was obtained by signal averaging during processing. The phase shift was measured as well as the amplitude difference between the lower and upper transducer signals. To quantify this behaviour, the signals were transformed to the frequency domain by means of a Fast Fourier Transform algorithm.

Defining \hat{p}_2 as the Fourier transformed pressure amplitude recorded by PT2, as depicted in Figure (6.3b), the corresponding fluid velocity \hat{v}_2 can be obtained by the momentum equation over the distance L_s :

$$\frac{\hat{p}_2}{L_s} = -\rho_f i\omega \hat{v}_2. \quad (6.1)$$

Subsequently, the macroscopic fluid velocity \hat{w} within the porous sample, follows from the continuity requirement for the incompressible fluid in the system $\phi \hat{w} = \gamma v_2$, where $\gamma = (A_{tot} - A_d)/A_{tot}$. The dynamic permeability for each frequency component may now be solved by means of the dynamic equivalent of Darcy's law as defined in Equation (3.2):

$$\frac{\eta \phi}{\hat{k}(\omega)} \hat{w} = \frac{\hat{p}_h - \hat{p}_l}{L_p}, \quad (6.2)$$

where the pressure drop is determined by the fluid pressure amplitudes \hat{p}_h and \hat{p}_l , just below and above the porous sample (Figure 6.3b). Using the momentum equations over distances x_1 and x_2 , these pressure amplitudes can be expressed in terms of the pressure recordings \hat{p}_1 and \hat{p}_2 :

$$\hat{p}_h = \hat{p}_1 - \frac{\gamma x_1}{L_s} \hat{p}_2, \quad (6.3)$$

$$\hat{p}_l = \hat{p}_2 + \frac{\gamma x_2}{L_s} \hat{p}_2. \quad (6.4)$$

We used samples of glued glass beads and the Asst3 sample, all with lengths of 100 mm and diameters of 60 mm. The samples of glass beads are made of three dominant glass bead sizes, respectively, $D_{dom}=0.93, 1.39,$ and 1.98 mm. The beads were glued together and to the wall of a confining cylinder by means of a epoxy resin, so that any free motion of the porous material was avoided. The Asst3 sample was also glued into a confining cylinder. Table

Parameter values	glass 1	glass 2	glass 3	Asst3
D_{dom} mm	0.93	1.39	1.98	0.30
ϕ	0.32 ± 0.02	0.34 ± 0.02	0.32 ± 0.02	0.51 ± 0.03
α_∞	1.90 ± 0.04	1.98 ± 0.04	1.81 ± 0.04	1.44 ± 0.03
k_0 Darcy	340 ± 20	920 ± 30	1500 ± 50	99 ± 7
ω_c rad/s	492	186	117	3577

Table 6.1: *Rock parameter values for dynamic permeability measurements.*

(6.1) shows the relevant parameter values and the rollover frequency ω_c , as defined in Equation (3.11). These values followed from independent non-acoustic experimental measurements as discussed in the following sections. As was mentioned before, the properties of the water saturating the samples were obtained from textbook values. Taking into account the temperature of the water during the measurements, average values for the experiments followed as $K_f=2.22$ MPa, $\rho_f = 1000$ kg/m³, and $\eta = 0.001$ Pa · s.

Results for both absolute and phase values of dynamic permeability measurements are presented in Figure (6.4a) and (6.4b). For each porous sample, dynamic permeability $\hat{k}(\omega)$ and frequency ω are scaled by corresponding steady-state permeability k_0 and rollover frequency ω_c .

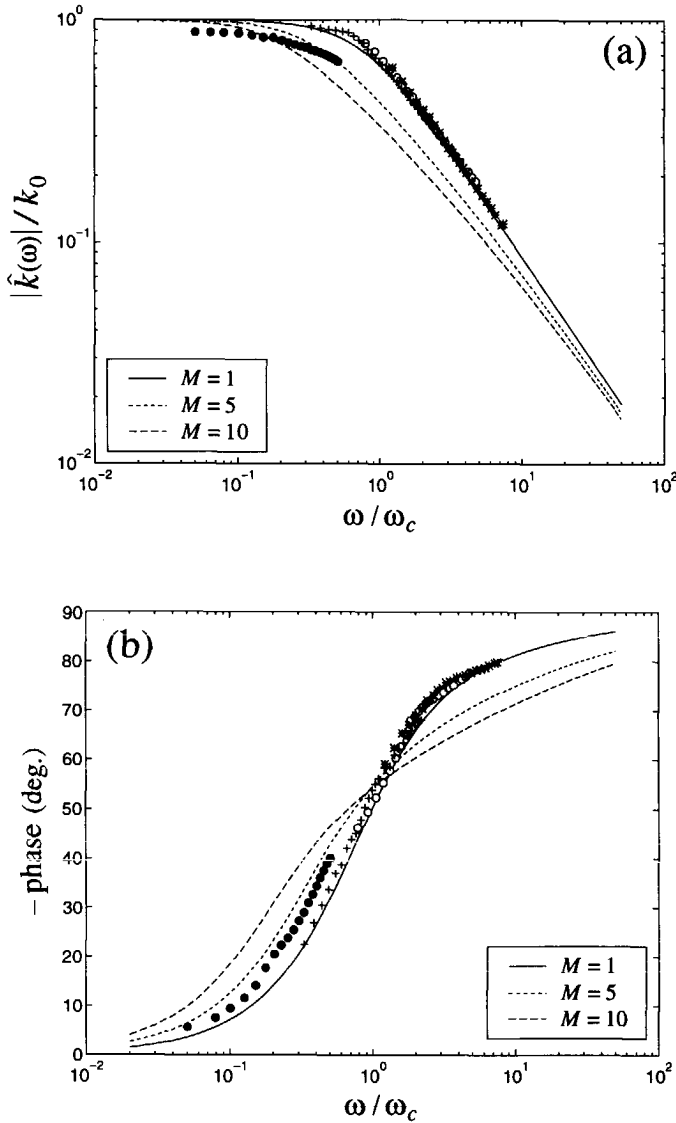


Figure 6.4: (a) Absolute and (b) negative phase values of dynamic permeability measurements. * glass beads 1.98 mm. \circ glass beads 1.39 mm. + glass beads 0.93 mm. \bullet Asst3. The drawn curves represent the scaling function for different M -values. Errors are indicated by the size of the data symbols.

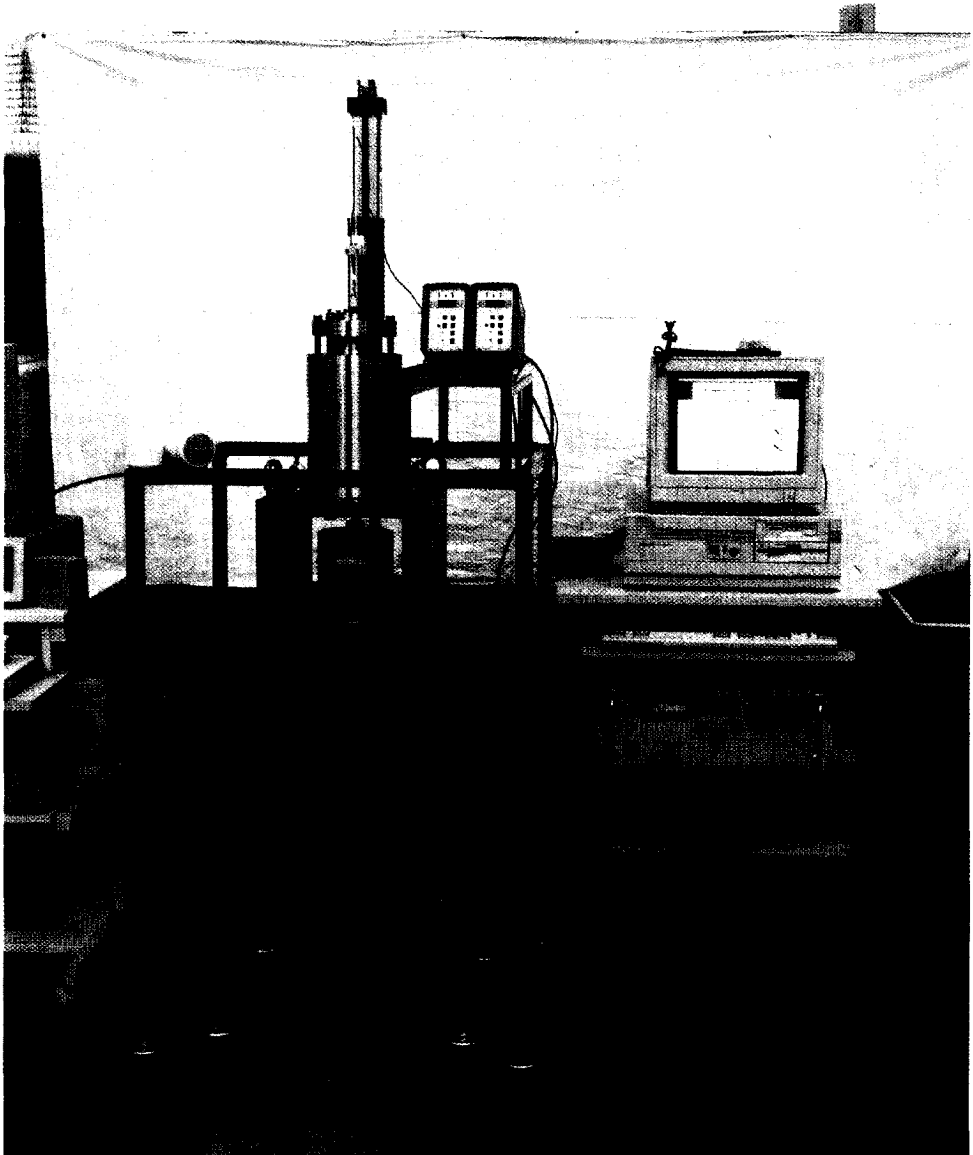


Figure 6.5: *Photo of Dynamic Darcy Cell and data-acquisition system.*

Obviously, the experimental data for the fused glass bead samples show excellent agreement with the scaling function for dynamic permeability for $M = 1$. Note that M is the similarity parameter as defined in Equation (3.12). In this way, the measurements supports the suggestion of Johnson et al. (1987) that M is equal to 1 for all porous media, or at least approximately. In contrast to the experimental data of Charlaix et al. (1988) and Smeulders et al. (1992), our experimental results were not affected by persistent set-up resonance.

A tendency to deviate from the $M = 1$ curve was observed for the dynamic permeability data for the Asst3 material. Both the absolute values and the phase values tend to coincide with the $M = 5$ curve. This supports the conclusion by Smeulders et al. (1994) that M might deviate from the value 1 for a porous medium with a sharp-edged pore structure ($M = 10$ to 100). However, our measurements indicated that the deviation is less pronounced than was predicted by Smeulders et al. (1994). From the photomicrograph of the Asst3 sample (see Figure 6.8) it seems plausible that this material has a sharp-edged pore structure. Sintered glass beads and natural rock samples show more smooth pore structures (see Figures 6.8 and 6.9). Therefore, extremely high M -values are not likely to occur for sintered glass bead and natural rock samples.

We will now continue with the discussion of the experimental determination of the rock parameters for the artificial and natural sandstone samples used for velocity and attenuation measurements (Chapter 7).

6.4 Porosity and grain density

Porosities of all porous samples were measured by using the standard two-weight (dry and buoyant) method. This implies that we first determined the dry weight G_0 of the porous sample, and then the weight G_1 of the same sample when it was fully water-saturated and fully immersed in water. For these porosity measurements we used four cores of each sample type to determine whether the measurements are reproducible. Typical core thickness was in the order of 20 mm. Core diameter ranged from 26 mm to 80 mm. From these experiments both porosity ϕ and particle density ρ_s were derived:

$$(1 - \phi)V_b = \frac{G_0 - G_1}{g\rho_f}, \quad (6.5a)$$

$$1 - \frac{\rho_f}{\rho_s} = \frac{G_1}{G_0}, \quad (6.5b)$$

where V_b is the bulk volume of the core, g is the constant of gravity and ρ_f the water density. Measured average porosities and particle densities for all porous samples are listed in Table (6.2).

Sample	ϕ	ρ_s (kg/m ³)
Asst1	0.34 ± 0.01	2230 ± 20
Asst2	0.40 ± 0.01	2750 ± 20
Nsst1	0.36 ± 0.01	2640 ± 20
Nsst2	0.31 ± 0.01	2640 ± 20
Nsst3	0.23 ± 0.01	2640 ± 20
Nsst4	0.25 ± 0.01	2640 ± 20
Bsst	0.23 ± 0.01	2640 ± 20

Table 6.2: Porosity and grain density.

6.5 Tortuosity

The tortuosity was determined in an electrical resistivity experiment. The analogy between the acceleration of an inviscid incompressible fluid within a rigid porous medium, and the electrical current density within an electrolyte filled porous insulator, was first demonstrated by Brown (1980). This was experimentally verified by Johnson et al. (1982). We may write

$$\frac{\alpha_\infty}{\phi} = \frac{r_s}{r_f}, \quad (6.6)$$

where r_s is the intrinsic resistivity (in Ωm) of the fluid-filled porous insulator, and r_f is the intrinsic fluid resistivity. The α_∞/ϕ ratio is known as the formation factor F . The set-up is drawn in Figure (6.6). A small cylindrical core sample was clamped between two permeable electrodes, covered with a rubber sleeve and placed inside the measurement cell. All porous core samples had a thickness and a diameter of 25 mm. Non-conducting PVC plugs were used to avoid any contact between the hollow electrodes and the cell. The sample was fully saturated with a 0.086 mol/l NaCl solution. The resistance R_c (in Ω) of the core sample was measured with a Wayne-Kerr resistance bridge. Measurement accuracy was better than 0.2%. For

the fluid resistivity measurements, the core sample was replaced by a piece of thin-walled perspex tubing of the same dimensions. The results of the tortuosity measurements are listed in Table (6.4).

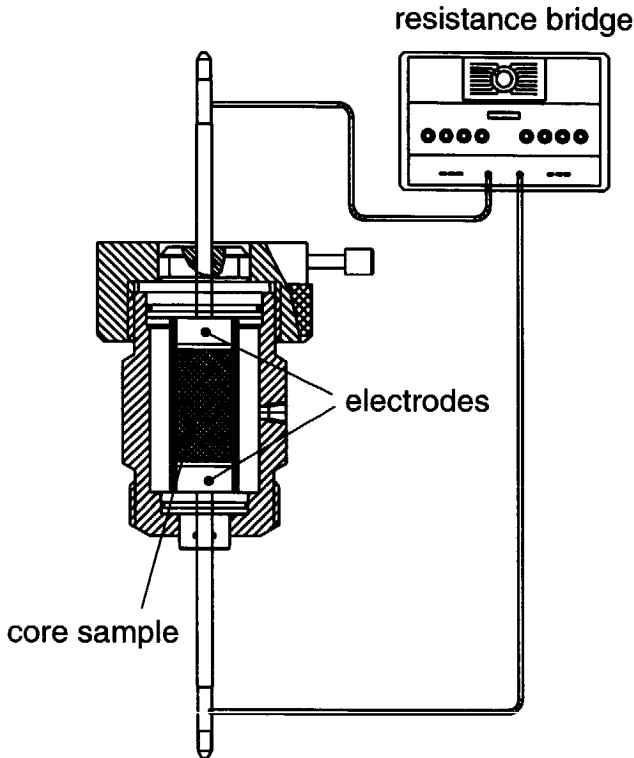


Figure 6.6: *Experimental set-up for tortuosity measurements.*

Sample	F	α_{∞}
Asst1	6.2 ± 0.2	2.1 ± 0.1
Asst2	4.8 ± 0.2	1.9 ± 0.1
Nsst1	5.0 ± 0.2	1.8 ± 0.1
Nsst2	6.6 ± 0.2	2.0 ± 0.1
Nsst3	12.1 ± 0.2	2.8 ± 0.1
Nsst4	9.1 ± 0.2	2.3 ± 0.1
Bsst	11.3 ± 0.2	2.6 ± 0.1

Table 6.3: *Formation factor and tortuosity values.*

6.6 Steady-state permeability

Figure (6.7a) shows the experimental set-up used for the steady-state permeability measurements. The same cylindrical core sample as described in the previous section was jacketed between two plungers, and placed in a stainless steel coreholder. A confining stress of approximately two bars was applied to the sample. The system was evacuated and fully saturated with water. During the measurements, water flows from the container vertically upwards through the core sample. The height of the container above the coreholder can easily be adjusted, so the flow can be measured as a function of the height of the driving head h (in m). The flow from the outlet of the coreholder was measured by a computer controlled balance. The volume flow Q (in m^3/s) through the sample is given by Darcy's law:

$$Q = \frac{k_0 A_c}{\mu} \frac{gh\rho_f}{L_c}, \quad (6.7)$$

where g is the constant of gravity. In Figure (6.7b) we plotted the volume flow against the driving head for three different core samples. For all samples

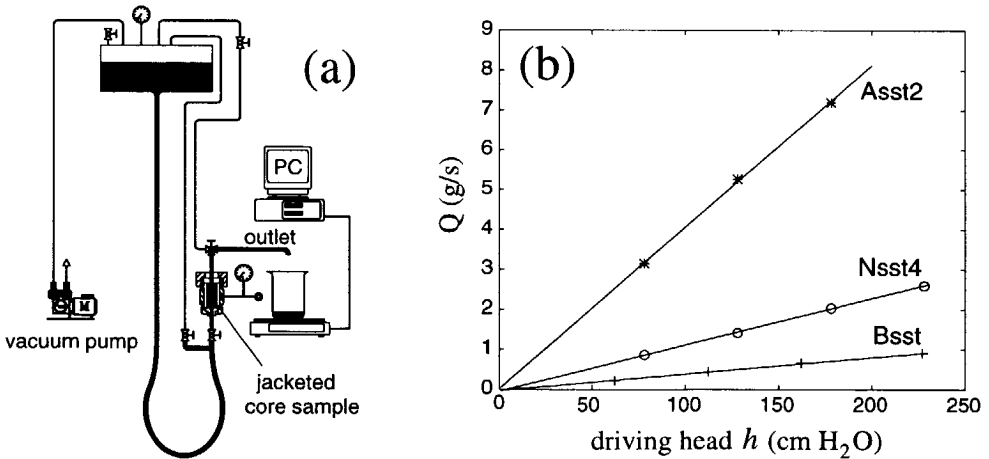


Figure 6.7: (a) *Experimental set-up for water flow steady-state permeability measurements.* (b) *Results for samples Asst2, Nsst4, and Bsst. The volume flow Q against the driving head h is plotted.*

we found a linear relationship between Q and h . The steady-state permeability can now easily be calculated by means of Equation (6.7). Results are shown in Table (6.4).

Sample	k_0 (Darcy)
Asst1	3.5 ± 0.2
Asst2	16.3 ± 0.5
Nsst1	27.0 ± 1.0
Nsst2	9.7 ± 0.5
Nsst3	3.7 ± 0.2
Nsst4	4.7 ± 0.2
Bsst	1.3 ± 0.1

Table 6.4: *Steady-state permeability values.*

6.7 Elastic properties

The values of the elastic bulk moduli K_b and G were deduced from acoustic transmission measurements in a water-filled tank on a dry sample of porous material, enclosed in a thin impermeable jacket. From the inverse squared velocities in Equations (4.22) and (4.35) the nondispersive shear and compressional wave speeds in dry material are, respectively (Johnson et al., 1982),

$$c_s(\text{dry}) = \sqrt{\frac{G}{(1-\phi)\rho_s}}, \quad (6.8a)$$

$$c_p(\text{dry}) = \sqrt{\frac{K_b + (4/3)G}{(1-\phi)\rho_s}}. \quad (6.8b)$$

The same experimental set-up was to determine the acoustic bulk properties of the saturated porous material. The results are shown in Table (6.5). It is

Sample	$c_s(\text{dry})$ (m/s)	$c_p(\text{dry})$ (m/s)	K_b (GPa)	G (GPa)
Asst1	1760 ± 20	3280 ± 20	9.8 ± 0.2	4.6 ± 0.2
Asst2	2160 ± 20	3580 ± 10	10.9 ± 0.2	7.7 ± 0.2
Nsst1	1340 ± 20	2310 ± 30	5.0 ± 0.2	3.0 ± 0.2
Nsst2	1710 ± 20	2850 ± 15	7.7 ± 0.2	5.3 ± 0.2
Nsst3	2180 ± 25	3540 ± 20	12.6 ± 0.2	9.7 ± 0.2
Nsst4	2120 ± 25	3450 ± 20	11.7 ± 0.2	8.9 ± 0.2
Bsst	1510 ± 25	2410 ± 30	5.6 ± 0.2	4.6 ± 0.2

Table 6.5: *Elastic properties.*

noteworthy that for all Nivelsteiner sandstone samples the contrast between

the grain and composite bulk moduli, K_s/K_b and K_s/G , correlate with the rock production parameters (see Table 6.6). A decrease in K_s/K_b and K_s/G ratios correlates with a decrease in porosity and permeability, and with an increase in tortuosity. This ratio is also a measure for the consolidation of the material. The samples Nsst1 and Nsst2 with relatively high grain composite ratios are unconsolidated samples, and the samples Nsst3 and Nsst4 are consolidated.

Sample	K_s/K_b	K_s/G	ϕ	k_0 (D)	α_∞
Nsst1	10	16.6	0.36	27.0	1.8
Nsst2	6.5	9.4	0.31	9.7	2.0
Nsst4	4.3	5.6	0.25	4.7	2.3
Nsst3	4.0	5.1	0.23	3.7	2.8

Table 6.6: *Correlation between K_s/K_b and K_s/G ratios and rock production properties for all Nivelsteiner sandstone samples.*

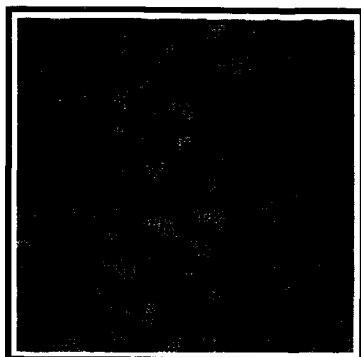
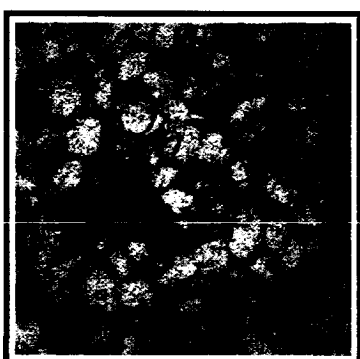
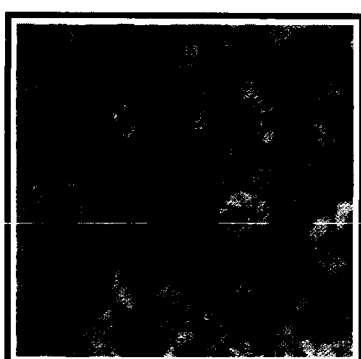
Asst1500 μm **Asst2**500 μm **Bsst**500 μm **Asst3**500 μm

Figure 6.8: *Photomicrographs of thin sections of the fused glass bead sample Asst1, the ceramic material Asst2, the Bentheimer sandstone sample Bsst, and the ceramic material Asst3. Blue indicates pore space.*

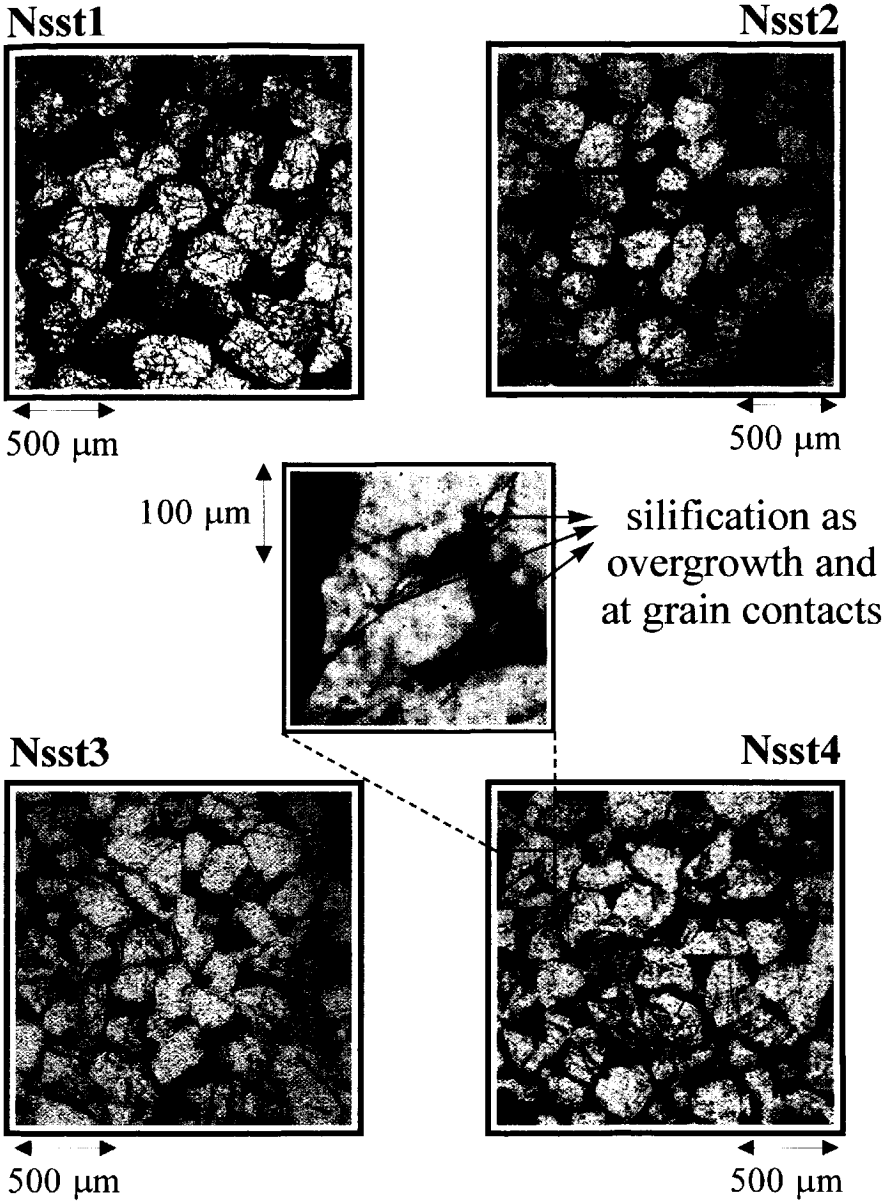


Figure 6.9: Photomicrographs of thin sections of four Nivelsteiner sandstone samples. The samples from the Nivelstein quarry are labelled Nsst1, Nsst2, Nsst3. The sample from the Heerenweg quarry is labelled Nsst4. Blue indicates pore space.

Chapter 7

Measurements of acoustic bulk properties

7.1 Introduction

This chapter discusses measuring the acoustic bulk properties of artificial and natural water-saturated porous samples. For all samples, we measured the phase speeds, attenuations, and specific attenuations as a function of frequency. We compared the experimental results with theoretical computations. The Biot slow wave was observed experimentally in natural water-saturated sandstone. To our knowledge, it is the first time that this observation was reported in such a medium. This enabled us to verify the Biot theory experimentally in natural water-saturated sandstone for all three bulk waves. All input parameters needed to calculate the theoretical values of the bulk properties were measured separately on all samples. This means that the comparison between experiments and theory does not involve any parameter adjustments.

7.2 Experimental set-up

For the experiments we used a transmission configuration similar to the ones used by Plona (1980) and Kelder and Smeulders (1995, 1996a). The experimental set-up is shown schematically in Figure (7.1). A photo is shown in Figure (7.6). A sample slab was carefully saturated with water. A CO₂ procedure was used for this (Smeulders et al., 1992). Subsequently, the slab was mounted on a rotation table in a water-filled tank to perform acous-

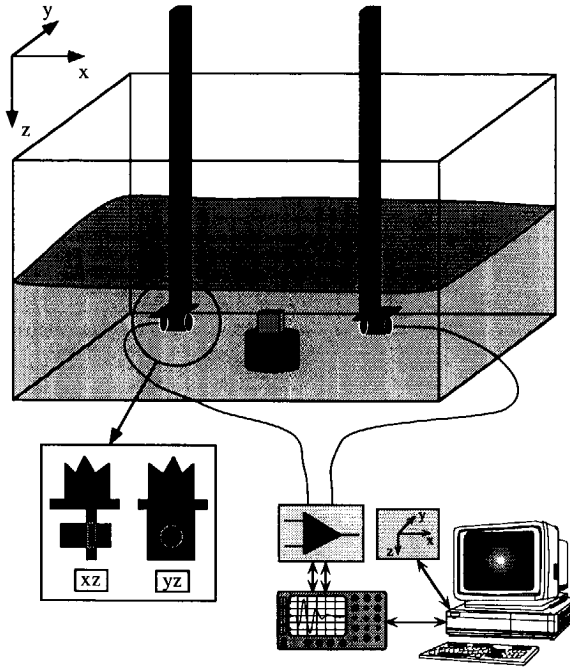


Figure 7.1: Configuration of the experimental set-up.

tic measurements at different angles of incidence. A single pair of identical piezo-electric ultrasonic transducers was used to generate and detect short duration acoustic pulses. Because of mode conversion at the interfaces between the saturated sample and the surrounding fluid, all three bulk waves were generated in the sample. Because of the different velocities of these wave modes, they were separated in time. Recorded signals were displayed on an oscilloscope and stored in a computer. Figure (7.2) shows a diagram of the various components of the data-acquisition system. The central part of the data acquisition set-up is a LeCroy 9400 digital oscilloscope (transient recorder). This oscilloscope contains two channels and an 8-bit A/D-converter. A signal averaging processing option was used to reduce the noise level in the recorded data. Pre-programmed acoustic pulses were supplied by a programmable waveform generator. The pulse was amplified by a broadband power amplifier before it was passed on to the emitting transducer. For extremely low amplitude levels of recorded signals a conditioning amplifier was used before data acquisition by the oscilloscope. The transduc-

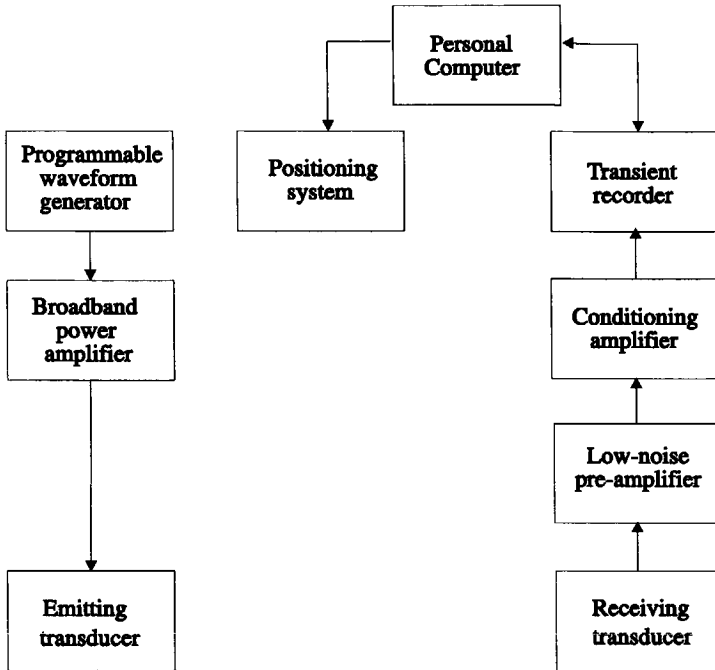


Figure 7.2: *Diagram of the data acquisition set-up.*

ers used for our laboratory measurements are commercially available, flat, circular, piezoelectric transducers with different centre frequencies and diameters. We used three pairs of transducers, manufactured by Panametrics and Rhosonics. The centre frequencies of these transducer pairs are 200, 500, and 800 kHz, respectively. In this way a total bandwidth of 100 kHz to 1 MHz was covered. An elaborate description of the transmitted wavefield of these transducers was given by Hylkema (1996). A *XYZ*-positioning system was used to control all transducer movements. The transducers were mounted on two vertical poles which were both attached to two horizontal bars. The distance between the transducers in the *X*-direction was controlled by sliding the two horizontal bars along a stiff frame from which they were suspended. The vertical poles were both able to slide in the vertical and horizontal direction along the horizontal bars. The transducers, placed at the bottom of the vertical poles, were able to rotate in the *XY*-plane. All movements were performed by six Stepper motors with a smallest step distance in each direction of $25.0 \pm 0.5 \mu\text{m}$. The rotation table was also controlled by the po-

sitioning system. A PC was used to guide the positioning system, control the oscilloscope, and store the recorded data during the measurements.

7.3 Water measurements

We used a short duration acoustic pulse for the transmission experiments. Figures (7.3a) and (7.3b) show an example of a recorded pulse and the corresponding frequency amplitude spectrum when no sample was placed on the rotary table. In Figure (7.3b) we observe the 500 kHz centre frequency. For

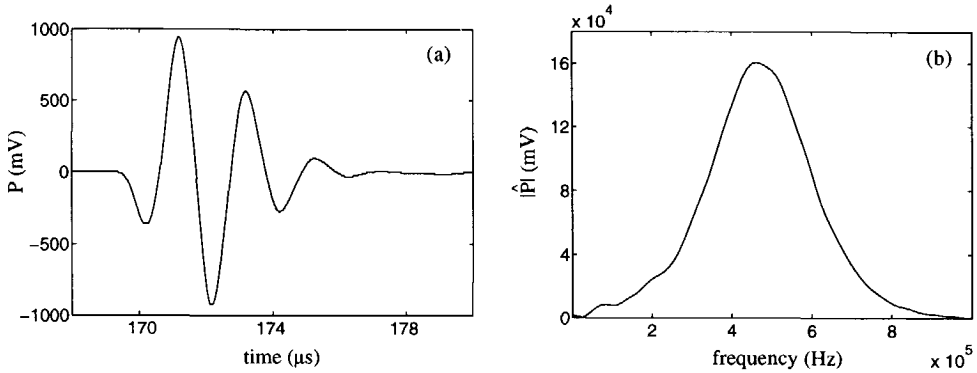


Figure 7.3: (a) Recorded time trace and (b) absolute values of frequency spectrum.

plane wave propagation in the positive x_3 -direction, the pressure response in the frequency domain for a transmitter-receiver distance d can be written as

$$\tilde{p}(\omega) = \tilde{Q}(\omega) \exp[ik_f d]. \quad (7.1)$$

$\tilde{Q}(\omega)$ is the source amplitude for a specific frequency, and $k_f = k_{3,f} = \omega/c_f$ is the fluid wavenumber. Combining recorded signals for distances d_1 and d_2 results in

$$\frac{\tilde{p}(d_2, \omega)}{\tilde{p}(d_1, \omega)} = \exp[ik_f(d_2 - d_1)]. \quad (7.2)$$

Fluid damping is ignored, which means that the fluid wave number k_f is real-valued. The phase angle of the pressure ratio in Equation (7.2) may be written as

$$\text{phase} \left\{ \frac{\tilde{p}(d_2, \omega)}{\tilde{p}(d_1, \omega)} \right\} = k_f(d_2 - d_1). \quad (7.3)$$

In Figures (7.4a) and (7.4b) results for the wavenumber $k_f = \omega/c_f$ are plotted as a function of frequency. The corresponding velocities follow as $c_f = 1477 \pm 2$ m/s and $c_f = 1476 \pm 2$ m/s, respectively. These are good approxi-

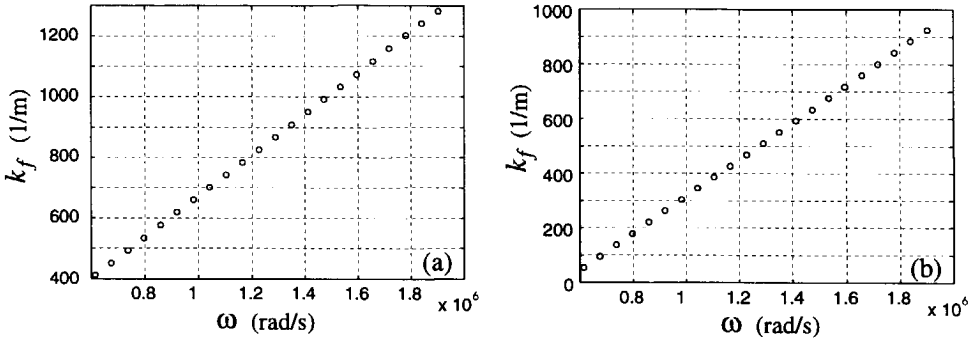


Figure 7.4: Wavenumber k_f as function of the frequency ω for (a) $d_1=0.11$ m; $d_2=0.12$ m, and (b) $d_1=0.11$ m; $d_2=0.18$ m.

mations of the theoretical phase velocity in water, which is 1480 m/s (Del Grosso & Mader 1972).

7.4 Microseismograms

Acoustic transmission measurements through slabs of water-saturated porous materials were performed for different angles of incidence θ (Figure 7.5 and 7.6). As it may be difficult to identify the arrivals of the different bulk waves at one single θ , it was convenient to perform measurements at several angles of incidence and plot the recorded traces in one single so-called microseismogram.

Artificial sandstone

In Figures (7.7) we plotted the microseismograms of the three transducer pairs. Results are shown for the fused glass bead sample Asst1. Effective noise reduction in the recorded traces was obtained by signal averaging procedures. The recorded acoustic traces are plotted against the angle of incidence at increments of 3° for the 200 kHz transducers and at increments

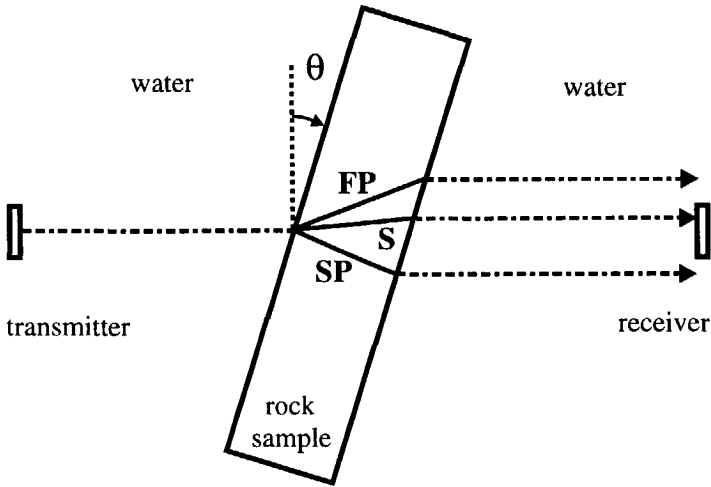


Figure 7.5: *Measurement configuration for ultrasonic detection of different wave modes. Reflected waves are not shown. The angle of incidence is indicated by θ .*

of 2° for the 500 and 800 kHz transducers. The different waves can be identified clearly. For normal incidence and $f_c = 800$ kHz, the fast compressional wave (FP) is recorded at $t = 0.0161 \mu\text{s}$, followed by its first multiple FFP at $0.0173 \mu\text{s}$. This first multiple interferes with the slow compressional wave SP, which arrives at $t = 0.0175 \mu\text{s}$. At $t = 0.0185 \mu\text{s}$ and $t = 0.0196 \mu\text{s}$ the second (FFFP) and third (FFFFP) multiples of the FP wave are visible. The FP wave disappears after the critical angle of incidence of about 34° is reached, which is slightly higher than the calculated critical angle of incidence according to Snell's law ($31^\circ \pm 1^\circ$). At increasing angles of incidence, this FP wave shows a time shift toward an earlier arrival time because the distance travelled through the sample becomes longer, while the velocity of this wave is higher than the wave speed in water. The shear wave arrival (S) is visible at an angle of 12° at $t = 0.0168 \mu\text{s}$ and is generated strongly at angles over 34° . Its velocity is of the same order as the velocity in water, so only a minor curvature of the arrivals at increasing angles of incidence is observed. As mentioned before, at small angles the arrival of the slow wave (SP) is drowned by the strong arrival of the first multiple reflection of the

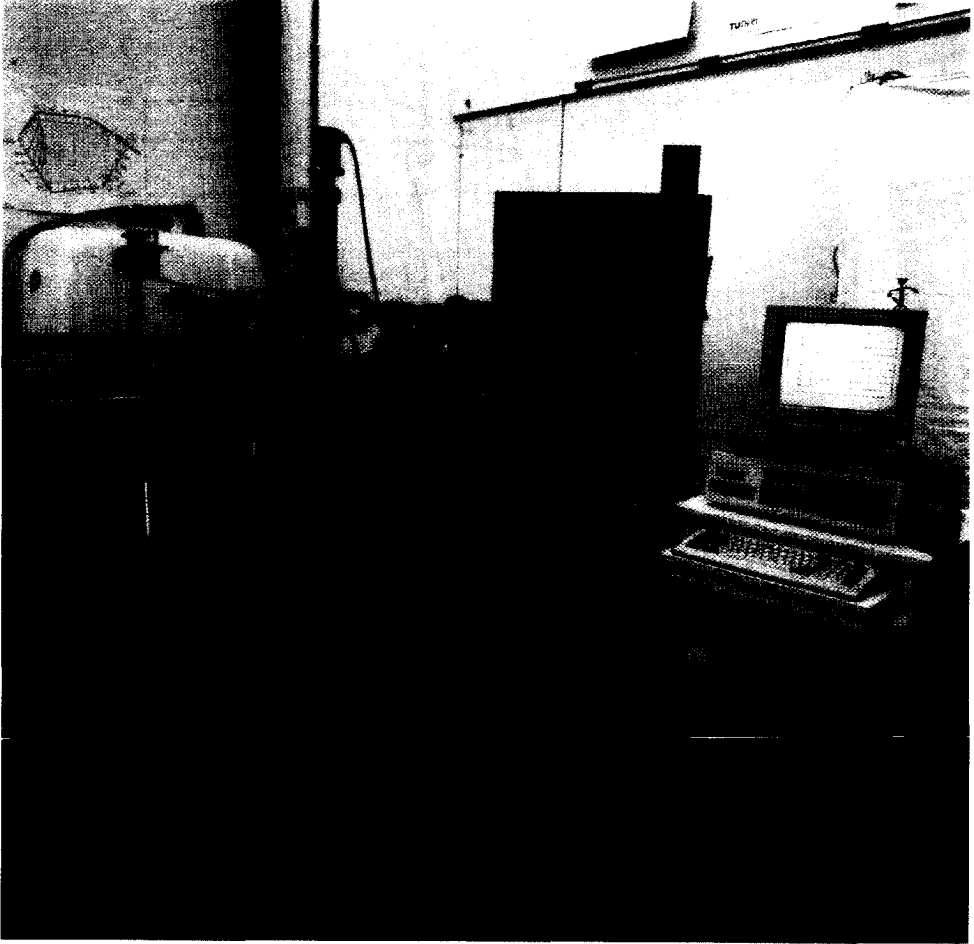


Figure 7.6: *Photo of water-filled tank for acoustic transmission experiments and data-acquisition system.*

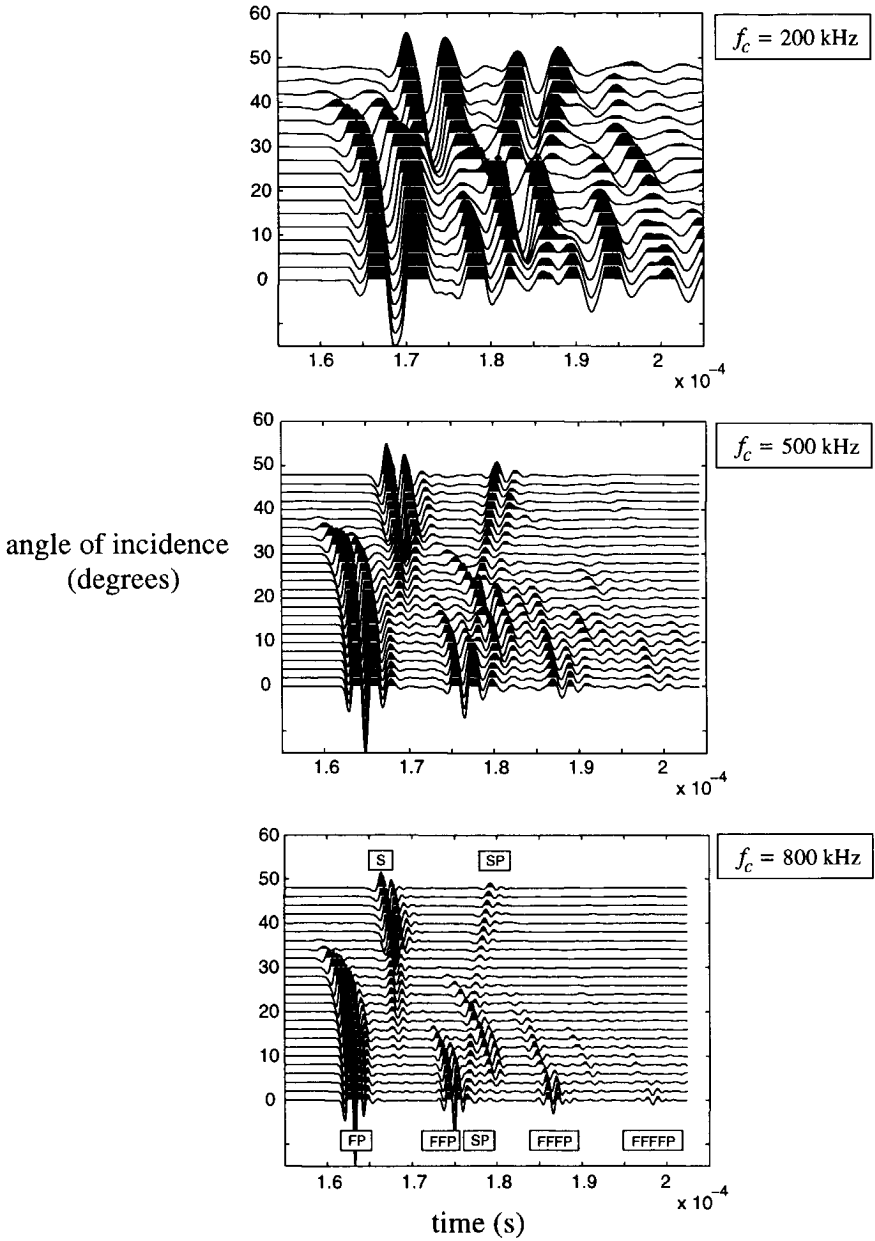


Figure 7.7: Microseismograms of recorded time traces in fused glass bead sample *Asst1* as a function of the angle of incidence. Results are plotted for three different transducer pairs with centre frequencies $f_c = 200$, $f_c = 500$, and $f_c = 800$ kHz, respectively.

fast wave (FFP). At an increased angle of incidence, this multiple reflection is no longer detected. This is due to the fact that the receiving transducer is in a fixed position, and the multiples have obtained significant displacement in the Y -direction. The distinction between the multiple reflections and the slow wave is easily made because of the curvature of the arrivals in the microseismogram. The arrivals of the multiple reflections bend to the left, while the slow wave arrivals curve to the right. From these seismograms it is also possible to extract qualitative information about frequency-dependent attenuation. The maximum amplitude of the FP wave at normal incidence is scaled to unity. The resulting scaling factor is used for all recorded traces. The same procedure is used for each single transducer pair. In Figures (7.7) we note that the damping of the shear wave becomes more pronounced with respect to the damping of the FP wave when the centre frequency increases. For the slow wave (SP) this increasing attenuation is even more pronounced. Considering one single microseismogram, we also note an increasing attenuation of the multiple reflections of the fast wave (FFP, FFFP, FFFFP) because of the longer travelpath of these multiples through the porous material. All this is in agreement with the Biot prediction for attenuation, as depicted in Figure (4.2).

Nivelsteiner sandstone

In Figures (7.8) the microseismograms of the Nivelsteiner sandstone sample Nsst4 are depicted. All three types of bulk waves are beautifully visible. We claim that it is the first time that the slow compressional wave is measured in a natural water-saturated rock (Kelder and Smeulders, 1997). Following Plona's observation of the slow wave in water-saturated sintered glass beads (Plona, 1980), up to now the slow wave was only detected in thin slabs of air-filled sandstone (Nagy et al., 1990), and in water-saturated, unconsolidated sand (Boyle and Chotiros, 1992). The Biot slow wave observation enabled us to simultaneously study all three wave types in natural sandstones.

Bentheimer sandstone

The microseismograms of the Bentheimer sandstone sample Bsst are depicted in Figures (7.9). In this case, a minimum of transmitted acoustic energy is observed for the shear wave, as well as for the multiple reflections of the fast compressional wave. The slow compressional wave was not detected at all.

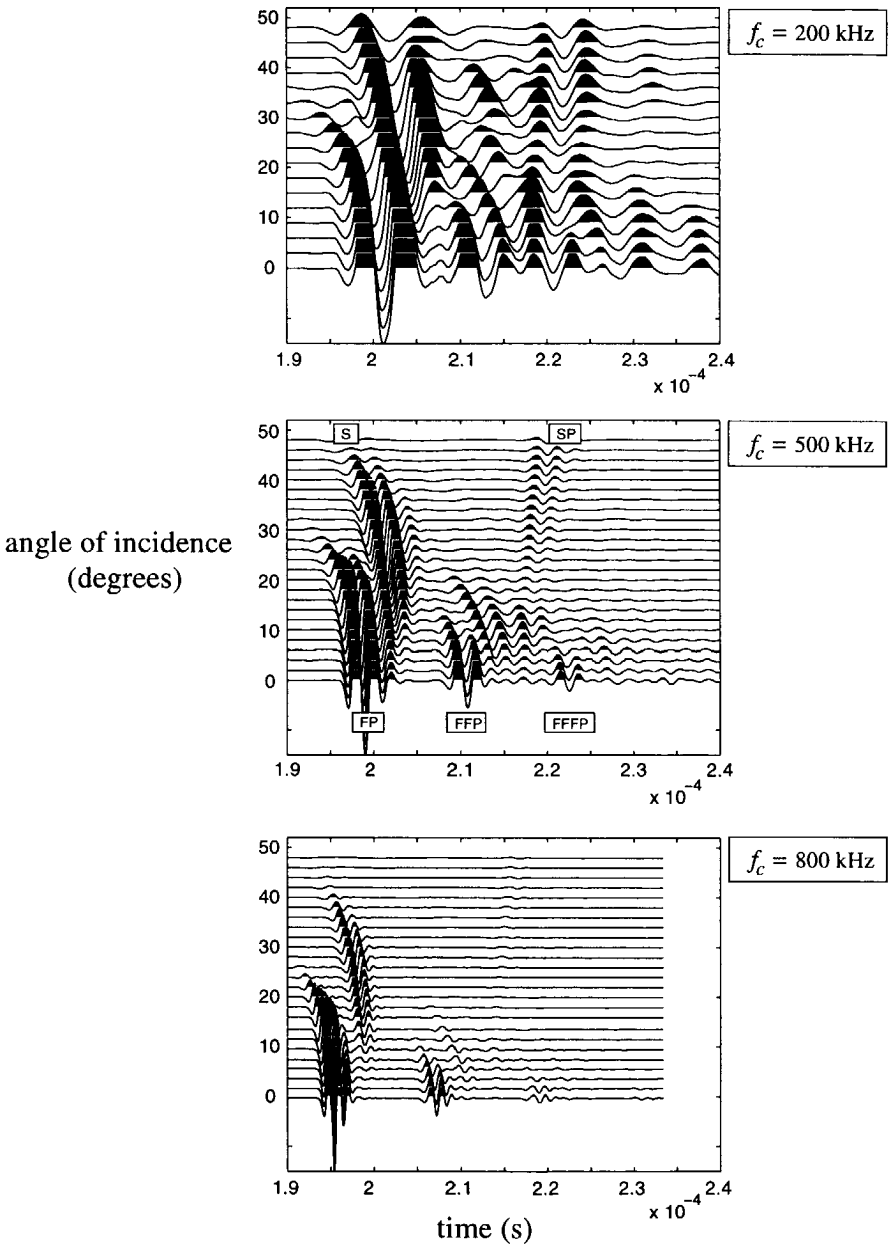


Figure 7.8: *Microseismograms of recorded time traces in the Nivelsteiner sandstone sample Nsst4 as a function of the angle of incidence. Results are plotted for three different transducer pairs with centre frequencies $f_c = 200$, $f_c = 500$, and $f_c = 800$ kHz, respectively.*

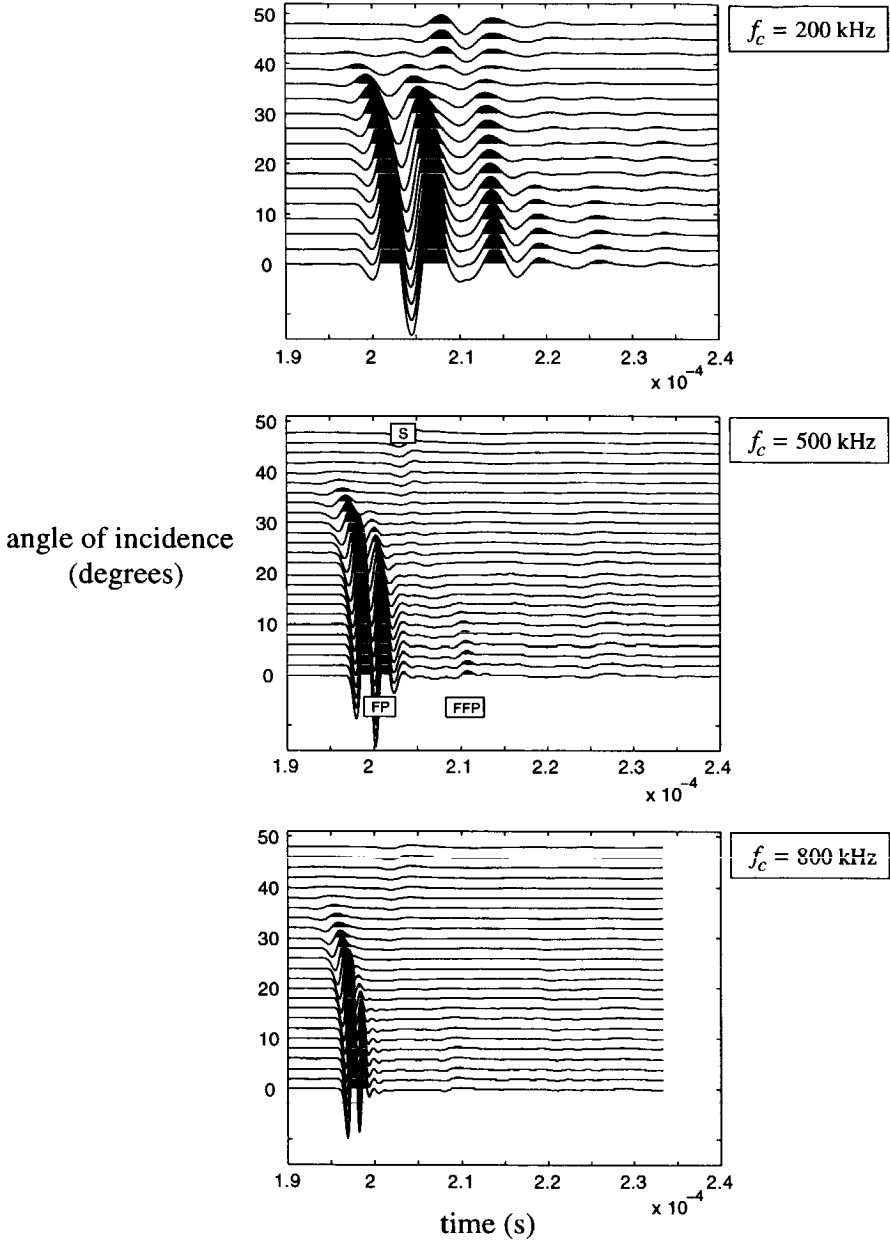


Figure 7.9: Microseismograms of recorded time traces in the Bentheimer sandstone sample *Bsst* as a function of the angle of incidence. Results are plotted for three different transducer pairs with centre frequencies $f_c = 200$, $f_c = 500$, and $f_c = 800$ kHz, respectively.

In Table (7.1) the measured wave velocities in all samples at 500 kHz are listed. They are obtained from first arrivals. In the next section, a spectral ratio technique is introduced to obtain these wave velocities as a function of frequency. Moreover, this technique allows accurate damping measurements of the recorded wavetrains.

Sample	c_{p1} (m/s)	c_s (m/s)	c_{p2} (m/s)
Asst1	3350 ± 30	1770 ± 30	960 ± 20
Asst2	3420 ± 30	2020 ± 30	990 ± 20
Nsst1	2440 ± 30	1350 ± 30	-
Nsst2	2810 ± 30	1510 ± 30	860 ± 20
Nsst3	3850 ± 30	2450 ± 30	810 ± 20
Nsst4	3690 ± 30	2290 ± 30	870 ± 20
Bsst	2910 ± 30	1450 ± 30	-

Table 7.1: Measured bulk wave velocity values for the 500 kHz centre frequency pulse.

7.5 Spectral ratio technique

It is possible to obtain frequency-dependent bulk properties from the ratio of the transmission amplitudes of the measured pulses through two slabs of different thicknesses (d_1 and d_2) of the same material (Toksöz et al., 1979; Sears and Bonner, 1981; Johnson et al., 1994). For a sample with thickness d_1 the configuration for an arbitrary angle of incidence θ is shown in Figure (7.10). The complex pressure amplitude \tilde{p}_{p1} of each Fourier component of an isolated fast wave can be written as

$$\tilde{p}_{p1}(\omega, d_1) = \tilde{Q} T_{p1,p}(\omega) \exp[ik_{p1}l_1] T_{p,p1}(\omega) \exp[ik_f(l_0 - l_1^*)], \quad (7.4)$$

where \tilde{Q} is the source characteristic, $T_{p1,p}$ is the transmission coefficient of the compressional wave in the fluid converted to the fast wave in the porous medium, $T_{p,p1}$ is the transmission coefficient of the fast wave converted to the compressional wave in the fluid, l_0 is the travelpath of the wave from the transmitter to the receiver, k_{p1} is the complex wavenumber of the fast wave, and k_f the real-valued wavenumber of the fluid. Furthermore, l_1 and l_1^* are length parameters depending on the angle of incidence θ (see Figure 7.10).

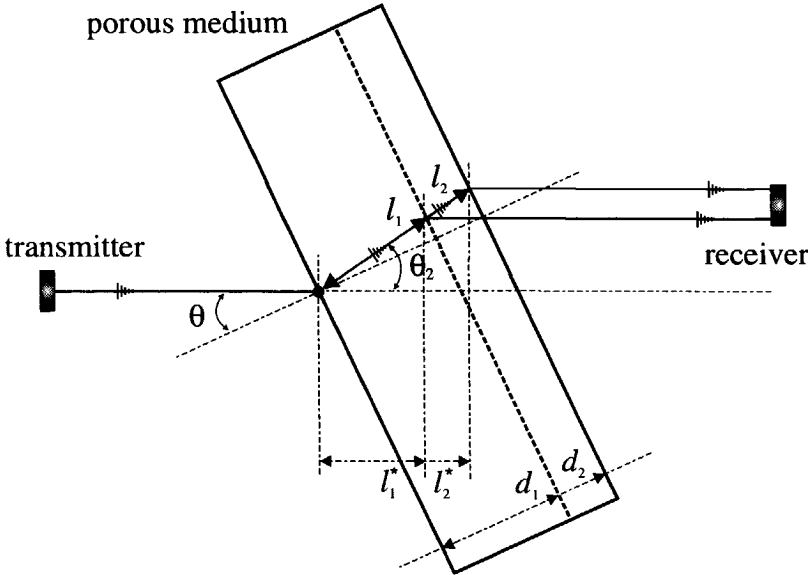


Figure 7.10: *Diagram of the experimental technique for measuring acoustic bulk properties of a fluid-saturated porous medium. Note that we have used two different thicknesses (d_1 and d_2) of the same material.*

For an isolated slow wave we find a similar expression:

$$\tilde{p}_{p2}(\omega, d_1) = \tilde{Q} T_{p2,p}(\omega) \exp[ik_{p2}l_1] T_{p,p2}(\omega) \exp[ik_f(l_0 - l_1^*)]. \quad (7.5)$$

The expression for the complex pressure amplitude of each Fourier component of an isolated shear wave can be written as

$$\tilde{p}_s(\omega, d_1) = \tilde{Q} T_{s,p}(\omega) \exp[ik_s l_1] T_{p,s}(\omega) \exp[ik_f(l_0 - l_1^*)]. \quad (7.6)$$

From Equations (7.4)-(7.6), the ratio of the pressure amplitudes for two different sample thicknesses (d_1 and d_2) gives an explicit expression for the complex wavenumber at any angle of incidence. This is due to the fact that this ratio separates bulk characteristics from source characteristics and transmission coefficients:

$$\frac{\tilde{p}_j(\omega, d_2)}{\tilde{p}_j(\omega, d_1)} = \exp[ik_j(l_2 - l_1)] \exp[-ik_f(l_2^* - l_1^*)]. \quad (7.7)$$

All relevant length parameters are shown in Figure (7.10). It can be seen that for normal incidence we have $l_1 = l_1^* = d_1$, and $l_2 = l_2^* = d_2$. Equation

(7.7) can now be written as

$$\frac{\tilde{p}_j(\omega, d_2)}{\tilde{p}_j(\omega, d_1)} = \exp \left[\frac{i(d_2 - d_1) (\Re\{k_j\} - k_f \cos(\theta_2 - \theta))}{\cos \theta_2} \right] \times \exp \left[\frac{-\Im\{k_j\}(d_2 - d_1)}{\cos \theta_2} \right]. \quad (7.8)$$

Subsequently, it can be seen that the real part of the complex wavenumber follows from

$$\text{phase} \left\{ \frac{\tilde{p}_j(\omega, d_2)}{\tilde{p}_j(\omega, d_1)} \right\} = \frac{i(d_2 - d_1) (\Re\{k_j\} - k_f \cos(\theta_2 - \theta))}{\cos \theta_2}. \quad (7.9)$$

According to Snell's Law, the angle θ_2 is a function of the measured phase speed

$$\frac{\sin(\theta)}{c_f} = \frac{\sin(\theta_2)}{c_j}, \quad (7.10)$$

for $j = p1, p2, s$. An iteration process (function `fzero` MATLAB) with the measured phase speeds c_j (see Table 7.1) as starting values was used to solve Equation (7.10).

The absolute values of the pressure ratio in Equation (7.8) yield the imaginary part of the complex wavenumber:

$$\left| \frac{\tilde{p}_j(\omega, d_2)}{\tilde{p}_j(\omega, d_1)} \right| = \exp \left[\frac{-\Im\{k_j\}(d_2 - d_1)}{\cos \theta_2} \right]. \quad (7.11)$$

Following the definitions of the acoustic bulk properties in Chapter 4, Equations (7.9) and (7.11) can now be used to determine the phase speed, attenuation, and specific attenuation for arbitrary angle of incidence θ . The spectral ratio technique requires the signals of corresponding bulk waves or reflections to be completely separated in time. Since we windowed out the isolated bulk wave arrivals and then Fourier analyzed them, any overlap of the signals may cause errors in the spectral data. The experimental results for each single bulk wave were obtained for that specific angle of incidence at which the bulk wave under consideration has its strongest arrival (see microseismograms). The receiver was displaced sideways for optimal recording of this strongest arrival. Repeated measurements at different angles of incidence in the vicinity of the strongest arrival were used to determine the accuracy of the measurements. Using the spectral ratio technique, we will now describe the measurements of the acoustic bulk properties for all types of rock samples.

7.6 Phase speed and attenuation measurements

Artificial sandstone samples

In Figures (7.11) the measured and theoretical values for the acoustic bulk properties of the Asst1 sample are shown. Results are obtained for all three transducer pairs covering a total bandwidth of 100 kHz to 1 MHz. For the

Fused glass bead sample Asst1

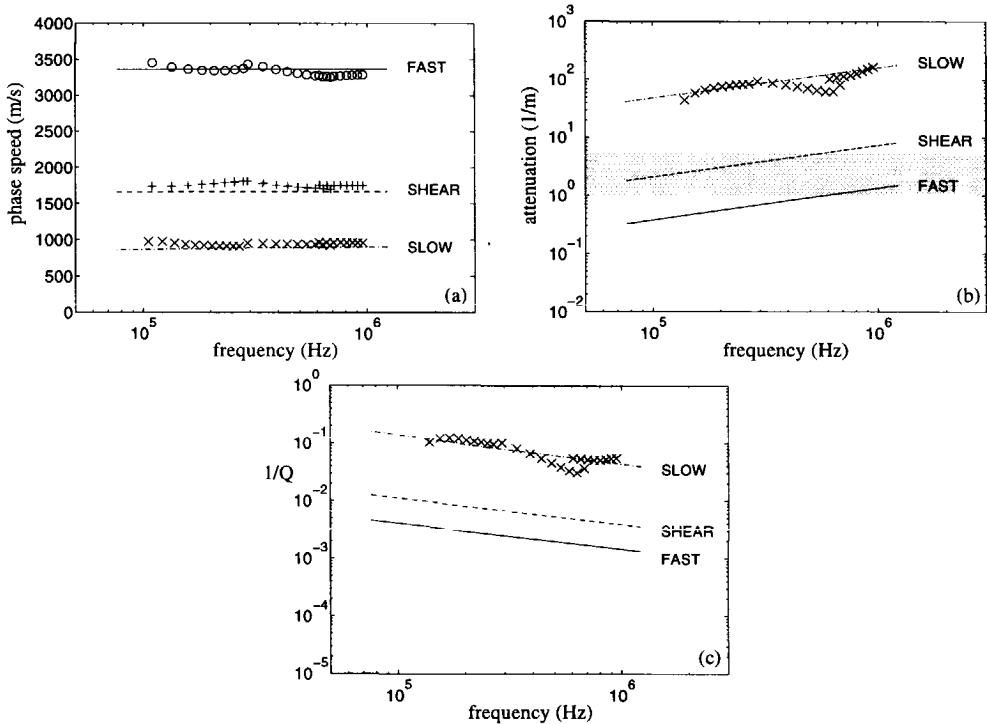


Figure 7.11: (a) Phase speed, (b) attenuation, and (c) specific attenuation $1/Q$ for the fused glass bead sample Asst1. The curves represent the theoretical predictions. The experiments are indicated by (o) fast wave, (+) shear wave, and (x) slow wave. The shaded region represents minimum detectable attenuation values. Errors are indicated by the size of the data symbols.

phase speeds in Figure (7.11a) and the (specific) attenuations in Figures (7.11b) and (7.11c), all measurements are in excellent agreement with predictions on the basis of the linear Biot theory. This means that the measured

phase speeds show non-dispersive behaviour but that the measured (specific) attenuations do show a distinct frequency dependence. As we noted before, all input parameters needed for the Biot predictions were measured independently. Maximum errors in our measurements were estimated by repeating the spectral ratio technique for different angles of incidence. Typically, the variation of the phase speed was within 5 % of the measured value, and the variation of the attenuation within 15 % of the measured value. These errors are indicated by the size of the data symbols. The transmission measurements were performed on thin slabs of porous material ranging from 2 cm to 4 cm. Whereas a typical attenuation value for the slow wave is 50 m^{-1} (40 % signal loss per cm), the shear wave attenuates by 5 m^{-1} (5 % signal loss per cm) and the fast wave by only 0.5 m^{-1} (0.5 % signal loss per cm). For these low attenuation values we had to take into account the minimum level of attenuation that could be measured with our equipment. From the 8-bit A/D-conversion it can be shown that the minimum detectable attenuation value ranges between 1 and 5 m^{-1} . This region is shaded in Figure (7.11b). The minimum detectable attenuation is the reason why we were not able to observe the very small bulk attenuation of the shear and fast waves in sample Asst1.

The results for the permeable ceramic sample Asst2 are depicted in Figures (7.12). Also for this sample, excellent agreement was found for the phase speed measurements. The attenuation of the slow wave is slightly underestimated at low ultrasonic frequencies but the deviation becomes progressively more significant for increasing frequencies (see Figure 7.12b). This is probably due to the onset of Rayleigh scattering, which becomes important in the ultrasonic frequency range (Schwartz and Plona, 1984). Scattering occurs whenever velocity or density heterogeneities occur on the same length scale as the acoustic wavelength. Winkler (1983) presented experimental results showing scattering effects in sandstones at ultrasonic frequencies, where the scatterers are the grains and the pores of the rock. This grainsize dependence is the reason why scattering was hardly observed in the fused glass bead sample Asst1 (see photomicrographs in Figure 6.8). Scattering results in dramatic signal loss. Typical Rayleigh scattering at high frequencies should follow a f^4 dependence, whereas the Biot theory shows an $f^{1/2}$ dependence. Another interesting result is that we were able to measure attenuation values for the shear wave in the Asst2 sample (see Figure 7.12b). From the 8-bit A/D-conversion it can be shown that the absolute accuracy for the attenuation measurements is 2 m^{-1} . This is represented by the error

Permeable ceramic material Asst2

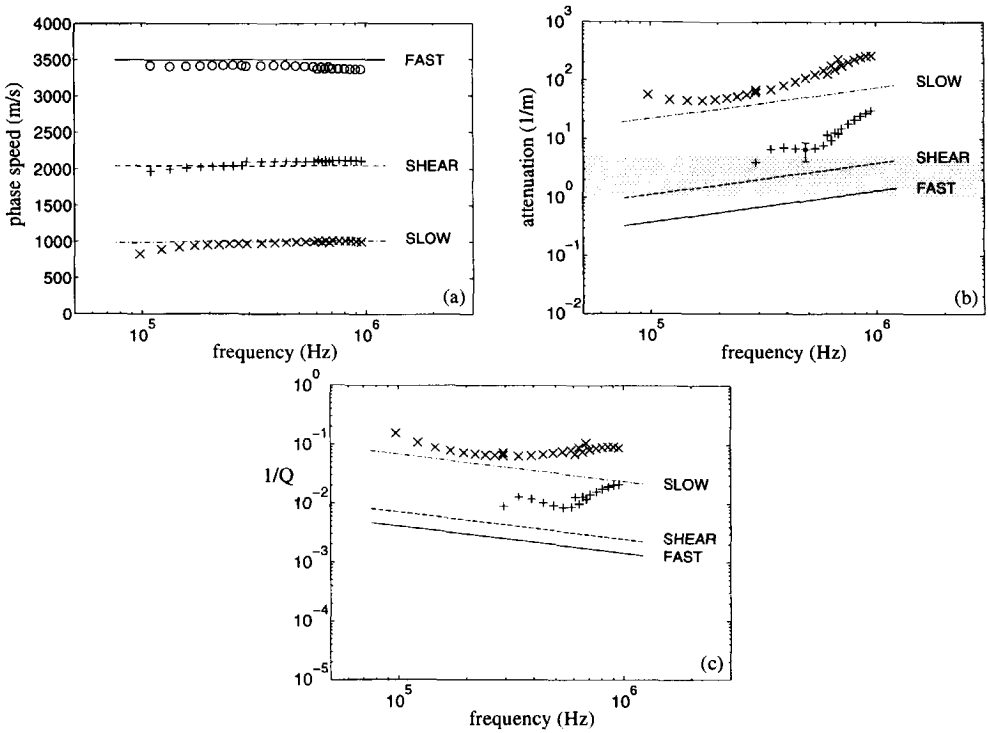


Figure 7.12: Theory versus experiments for the permeable ceramic sample Asst2. Legend identical to Figure (7.11). The error bar indicates the absolute accuracy of the data-acquisition set-up ($2 m^{-1}$).

bar in Figure (7.12b). Also in this case the attenuation is slightly underestimated for low ultrasonic frequencies, but for increasing frequencies the f^4 dependence becomes clearly visible. The fast wave attenuation was too small to detect. Similar results for artificial sandstone samples were found by Hovem and Ingram (1979); Berryman (1980); Johnson and Plona (1982); Johnson et al. (1994); Kelder and Smeulders (1995, 1996a).

Nivelsteiner sandstone samples

In Figures (7.13), the results from the spectral ratio technique for the sample Nsst4 are shown. The measured phase speeds are in excellent agreement with the theoretical predictions. This is also the case for the newly observed

slow wave. In this sample, we were able to measure even the attenuation of the fast compressional wave (see Figures 7.13 b and c). Despite the onset

Nivelsteiner sandstone sample Nsst4

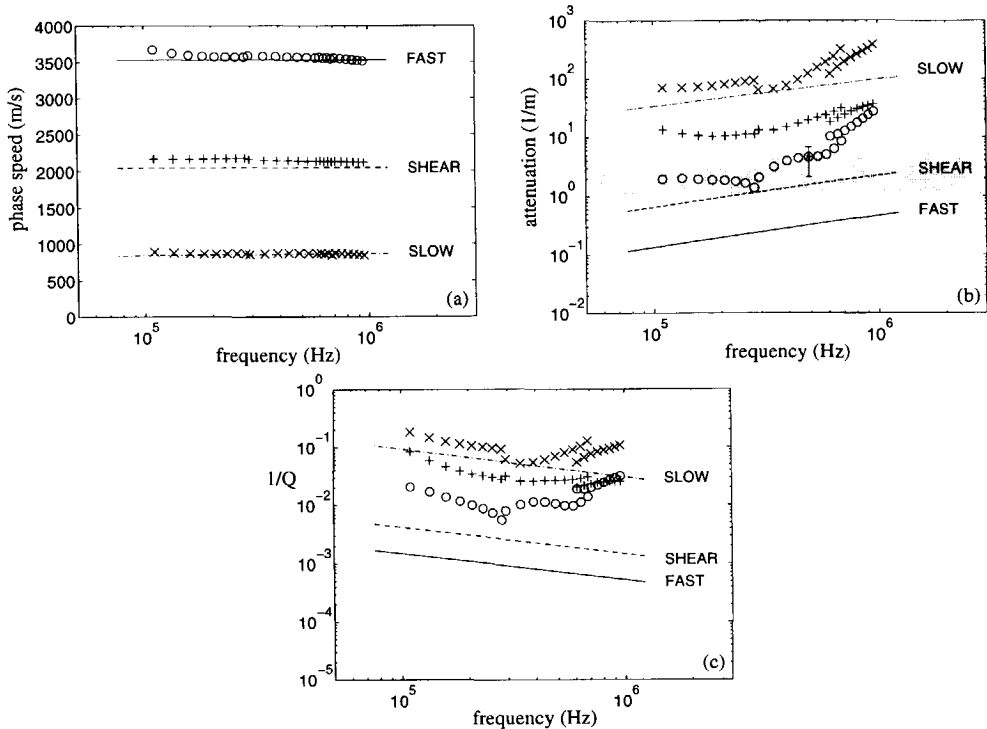


Figure 7.13: *Theory versus experiments for Nivelsteiner sandstone sample Nsst4. Legend identical to Figure (7.11). The error bar indicates measurement accuracy of the data-acquisition set-up (2 m^{-1}).*

of Rayleigh scattering at high ultrasonic frequencies, the attenuation of the slow wave is only slightly underestimated by the Biot theory. This underestimation is greater for the shear and fast waves. Similar results were found for the Nivelsteiner sandstone sample Nsst3, as depicted in Figures (7.14). The phase speed measurements in Figure (7.14a) are in good agreement with the theoretical predictions. Only the measurements of the shear wave show a maximum discrepancy of 10 % from the theory. The comparison between theory and experiments for the slow wave attenuation is quite good and discrepancies for the shear and fast wave attenuation are similar to the results for sample Nsst4. In the literature, several non-Biot attenuation mechanisms

Nivelsteiner sandstone sample Nsst3

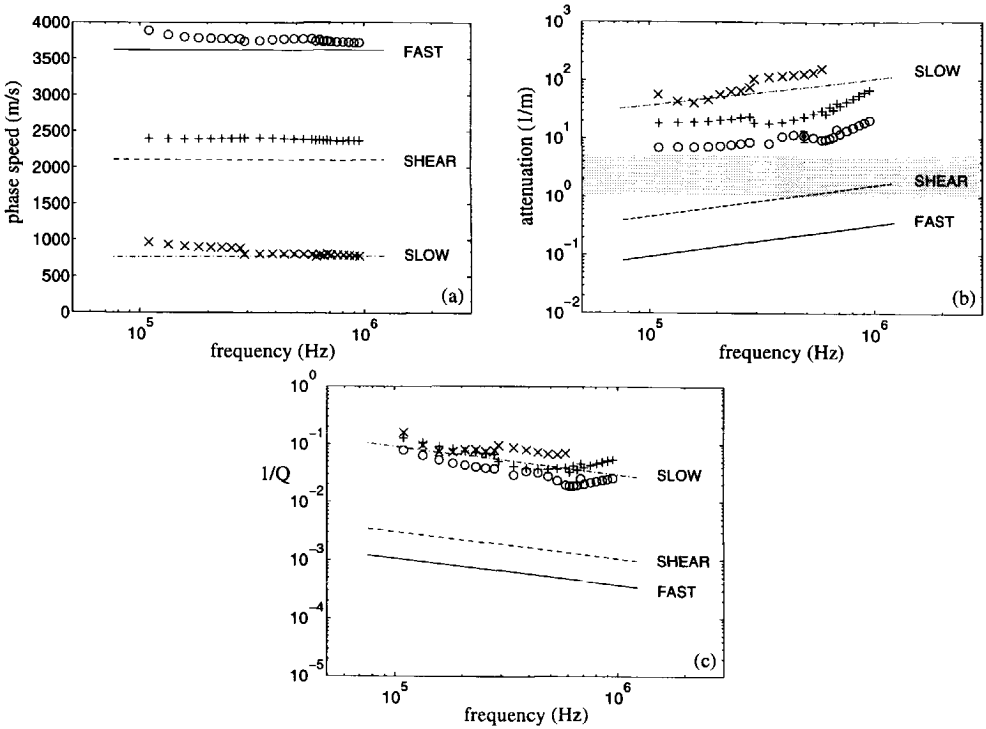


Figure 7.14: Theory versus experiments for Nivelsteiner sandstone sample Nsst3. Legend identical to Figure (7.11). The error bar indicates measurement accuracy of the data-acquisition set-up ($2 m^{-1}$).

were proposed which may play a role in the additional attenuation of waves in natural sandstones. One of these mechanisms is the so-called 'local flow', which is based on small aspect-ratio microcracks along grain boundaries, generating local fluid flow at the grain scale. If pores are isolated from one another, then the fluid pressure created in each pore by the passage of an elastic wave depends on the pore aspect ratio. Because pores in sandstones are interconnected, the fluid pressure in pores with different aspect ratios will attempt to equilibrate by local flow. Viscous dissipation driven by this local flow increases the wave attenuation (O'Connell and Budsonsky, 1977; Murphy et al., 1986). The origin of this dissipation is in fact the same as in the Biot theory: viscous losses in the pore fluid from motion of the fluid relative to the solid skeleton. However, whereas the 'local flow' mechanism is based

on microscopic fluid motion, the Biot theory is concerned with macroscopic fluid flow controlled by the interconnected pore geometry. Despite the fact that most of the local flow models can be fitted to experimental data, none of them can be used as an independent theory for attenuation prediction. This is because they all depend strongly on details of the microstructure that cannot yet be adequately quantified (Winkler and Murphy III, 1995). The driving force for the local flow mechanism is the compression of solid grains, which induces local flow from microcracks. For the slow wave, only a small part of the wave motion is governed by the solid phase, which makes this wave ineffective at generating local flow attenuation (Gist, 1994). Besides the Biot fluid flow attenuation, the local flow mechanism might contribute to the attenuation in samples Nsst4 and Nsst3. However, for sample Nsst4 it should be noted that the results were obtained close to or within the limits for detectable attenuation values (shaded region). Obviously, for increasing frequencies we note for both samples that scattering occurs.

In Figures (7.15) and (7.16), results for the samples Nsst2 and Nsst1 are plotted. In contrast to the Nsst3 and Nsst4 samples, which were consolidated ones, the samples Nsst1 and Nsst2 are unconsolidated (see the photomicrographs in Figure 6.9). We found in Chapter 6 that the measure for consolidation can be derived from the ratios of the bulk moduli of the matrix and the grains K_s/K_b and K_s/G . For all Nivelsteiner sandstone samples these ratios are given in Table 7.2. The unconsolidated Nsst1 and Nsst2

Sample	K_s/K_b	K_s/G
Nsst1	10	16.6
Nsst2	6.5	9.4
Nsst3	4.0	5.1
Nsst4	4.3	5.6

Table 7.2: K_s/K_b and K_s/G values for all Nivelsteiner sandstone samples.

samples have higher K_s/K_b and K_s/G ratios than the consolidated Nsst3 and Nsst4 samples. The Nsst2 sample was used by Kelder and Smeulders (1997) in their paper on the first experimental observation of the Biot slow wave in water-saturated natural sandstone. In both the Nsst2 and Nsst1 samples, the phase speeds are in good to excellent agreement with the Biot theory. The attenuation of the slow wave of sample Nsst2 is slightly underestimated by the Biot theory. For sample Nsst1, we were not able to record the slow compressional wave. Also in these samples, the attenuation of the shear

Nivelsteiner sandstone sample Nsst2

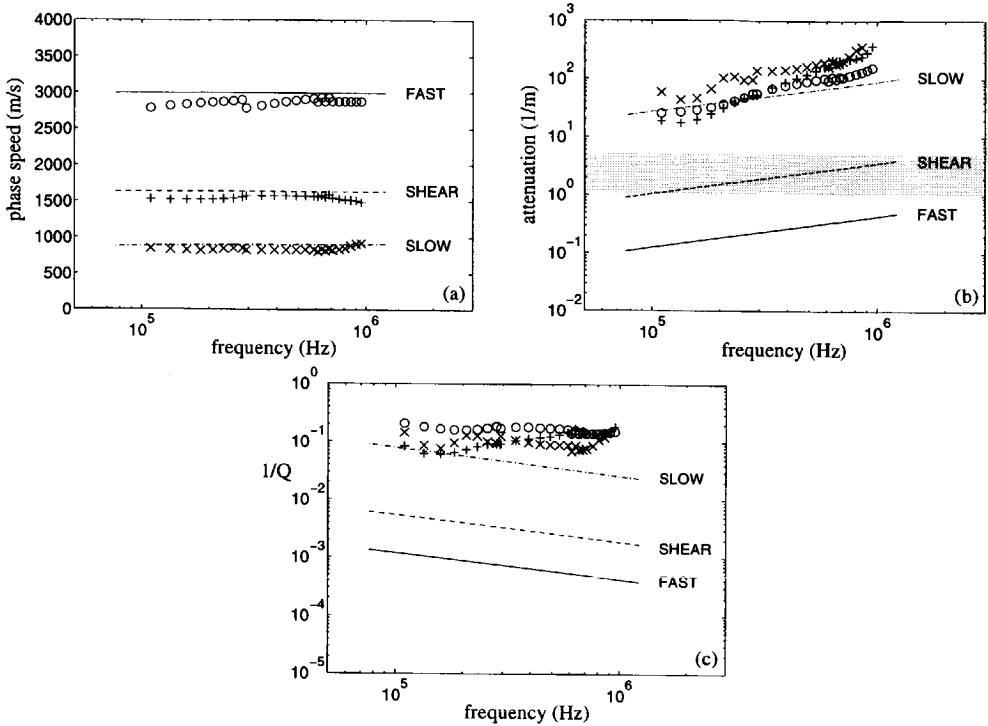


Figure 7.15: *Theory versus experiments for Nivelsteiner sandstone sample Nsst2. Legend identical to Figure (7.11)*

and fast wave are underestimated by Biot's theory. We also find that the underestimation of the shear and fast wave attenuation in these unconsolidated samples is much greater than the underestimation in the consolidated samples Nsst3 and Nsst4. Because local flow is very unlikely to occur in the unconsolidated samples (Murphy et al., 1986), our observations strongly suggest the existence of an additional non-Biot type of attenuation in unconsolidated material. Plona and Winkler (1985) mentioned the possibility of a type II scattering mechanism related to the interactions between grains ('connected solid space'). They observed a qualitative correlation between this scattering loss and the contrast between the grain and matrix bulk moduli, as calculated in Table 7.2. In their experiments, a pressure increase tends to reduce this scattering loss while also reducing the grain/matrix bulk moduli ratios. Taking into account this correlation, type II scattering loss,

Nivelsteiner sandstone sample Nsst1

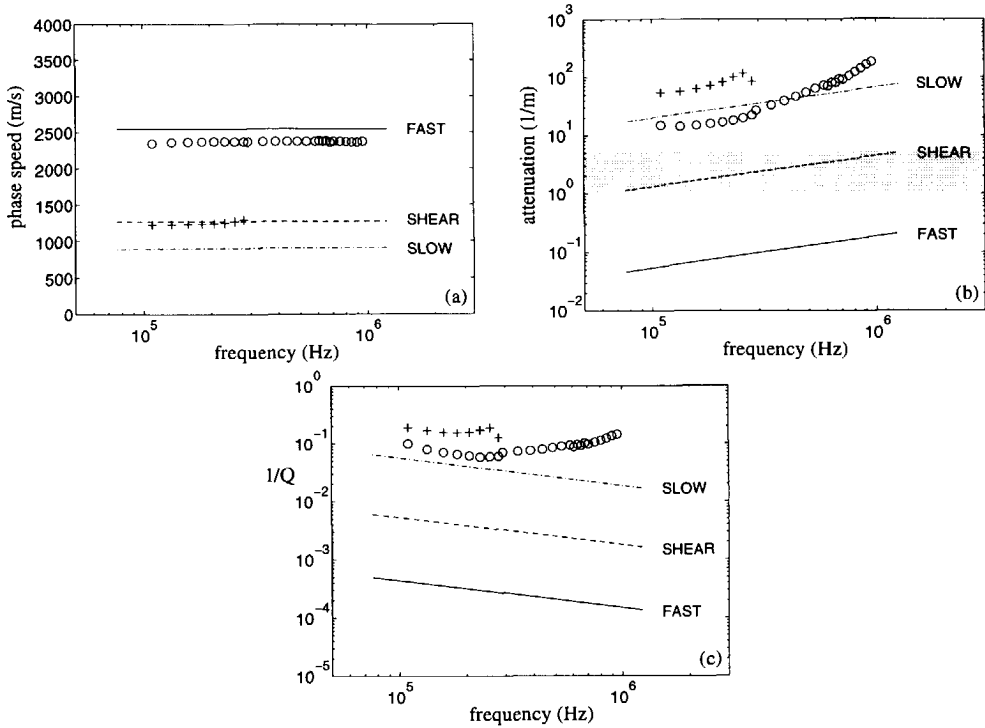


Figure 7.16: Theory versus experiments for Nivelsteiner sandstone sample Nsst1. Legend identical to Figure (7.11)

related to the relatively high K_s/K_b and K_s/μ ratios for our unconsolidated samples, might cause the high attenuation values of the shear and fast waves.

Bentheimer sandstone sample

Results for the Bentheimer sandstone sample Bsst are shown in Figures (7.17). The slow wave could not be detected. The phase speeds of the fast and shear waves are in excellent agreement with the Biot theory, as depicted in Figure (7.17a). The measured attenuation of the shear and fast waves in the Bsst sample was, respectively, a hundred and a thousand times greater than predicted. Another attenuation mechanism may explain why the slow wave was not detected in Bentheimer sandstone. Klimentos and McCann (1988) demonstrated that the attenuation of the slow wave increases strongly

by adding clay suspensions inside the pores of artificial cemented sandstones, which finally resulted in the complete disappearance of this wave. Therefore, it is possible that the absence of the slow wave in the Bsst sample is explained by kaolinite (clay) particles present in this sandstone (see photomicrograph in Figure 6.8). Consequently, the pureness of the Nivelsteiner sandstone (over 95% grained quartz) is probably the reason why we observed the slow wave in this sandstone without any problem. The great discrepancy in measured and predicted attenuation for the shear and fast waves in the Bsst sample is probably due to a combination of these clay particles and the local flow mechanism.

Bentheimer sandstone sample Bsst1

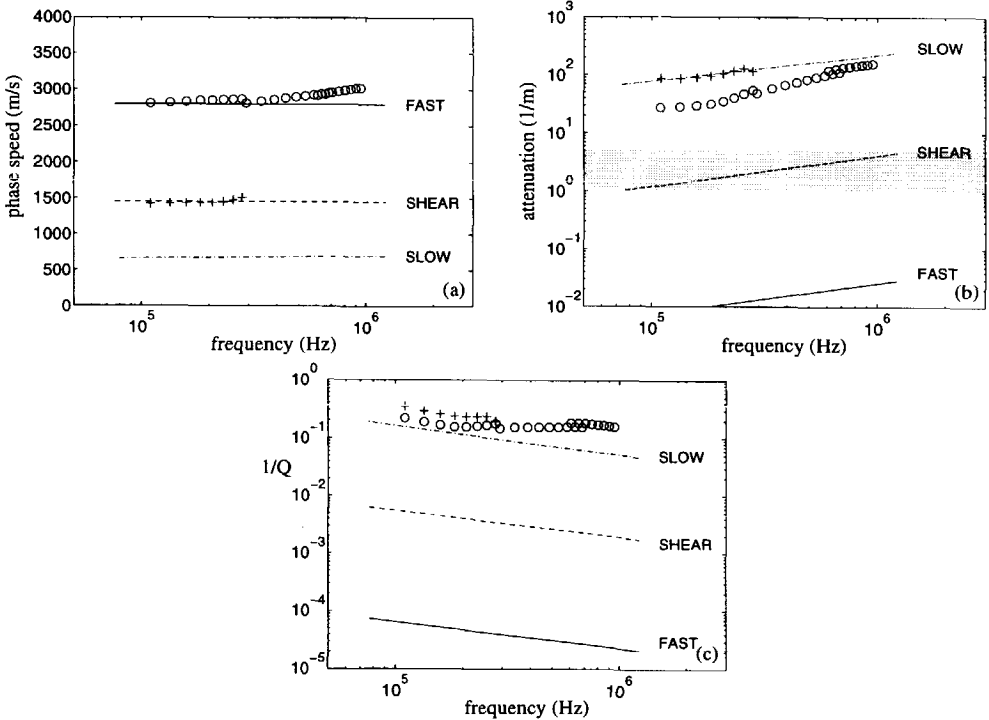


Figure 7.17: Theory versus experiments for Bentheimer sandstone sample Bsst. Legend identical to Figure (7.11)

7.7 Discussion and conclusions

This chapter showed a large number of ultrasonic experiments on artificial and natural water-saturated sandstones. Measured microseismograms, showing the recorded time traces as a function of the angle of incidence, were used to obtain qualitative attenuation behaviour of propagating waves in the rock samples. Frequency-dependent phase speed and attenuation measurements were compared with calculations based on the Biot theory. All input parameters for the Biot theory were obtained by independent experiments and thus the theory represents a purely predictive set of results. The Biot theory, without any adjustable parameters, gave a very accurate description of all three phase speed measurements in both water-saturated artificial and natural sandstones. This predictive power of the Biot theory is truly a major strength. Measurements of slow wave attenuation in the fused glass bead sample conformed excellent to the Biot predictions. For all other artificial and natural sandstone samples the slow wave attenuation was underestimated only slightly. Most samples showed a steep increase in slow wave attenuation at higher frequencies. This is indicative for Rayleigh scattering. The Biot theory strongly underestimated the attenuation behaviour of the fast and shear wave in natural sandstones. Scattering, local flow, and clay-related damping most likely account for the differences between the measured attenuation and Biot predictions. In the unconsolidated Nivelsteiner sandstone samples we found higher attenuation values than in the consolidated samples. A type II scattering mechanism related to the contrast between the grain and matrix bulk moduli K_s/K_b and K_s/G may have caused this additional attenuation in the unconsolidated samples. A review of attenuation mechanisms known from literature for all bulk waves in the rock samples is given in Table 7.3.

Sample	fast P – wave	shear wave	slow P – wave
Asst1	· attenuation not measurable	· attenuation not measurable	· Biot fluid flow*
Asst2	· attenuation not measurable	· Biot fluid flow* · type I scattering for increasing frequencies	· Biot fluid flow* · type I scattering for increasing frequencies
Nsst1	· Biot fluid flow · type I/II scattering	· Biot fluid flow · type I/II scattering	· wave mode not observed
Nsst2	· Biot fluid flow · type I/II scattering	· Biot fluid flow · type I/II scattering	· Biot fluid flow · type I/II scattering
Nsst3	· Biot fluid flow · type I scattering for increasing frequencies · local fluid flow	· Biot fluid flow · type I scattering for increasing frequencies · local fluid flow	· Biot fluid flow* · type I scattering for increasing frequencies
Nsst4	· Biot fluid flow · type I scattering for increasing frequencies · local fluid flow	· Biot fluid flow · type I scattering for increasing frequencies · local fluid flow	· Biot fluid flow* · type I scattering for increasing frequencies
Bsst	· Biot fluid flow · local fluid flow · clay-related damping	· Biot fluid flow · local fluid flow · clay-related damping	· wave mode not observed

Table 7.3: *Review of attenuation mechanisms from literature for all bulk waves in the various rock samples. For type I scattering, the individual grains and pores are the scattering objects. In type II the scattering strength is related to the contrast between grain and matrix bulk moduli. The superscript * indicates a good agreement between Biot theory and experiments.*

Chapter 8

Conclusions

1. Based on straightforward continuity and constitutive equations we showed that the generalized elastic coefficients appearing in the Biot theory for wave propagation in porous media can be related to measurable rock and fluid parameters such as porosity and bulk moduli. These relations were required to obtain a purely predictive set of results, which was used to verify the theory with experiments.
2. At low frequencies wave propagation is dominated by viscous forces, and at high frequencies inertia effects prevail. The viscous effects are characterized by the steady-state permeability and the inertial effects by the tortuosity parameter.
3. The transition at intermediate frequencies can be described by the dynamic permeability model of Johnson et al. (1987). This model only depends on the rollover frequency and a similarity parameter M . By modelling, we demonstrated that under normal conditions M has values close to 1, as originally suggested by Johnson et al.
4. Solving the Biot equations leads to a shear wave, a fast compressional wave in which fluid and solid move in-phase, and a highly dissipative slow compressional wave in which fluid and solid move out-of-phase. The influence of the frequency-dependent dynamic permeability is limited to the phase speed of the slow wave and the higher frequency range attenuation coefficients of all wave types.
5. For relevant ratios of grain/matrix moduli, the high-frequency limits of the fast and slow wave velocities normalized by the corresponding

velocities for incompressible grains varied by less than 10%. For increasing compressibility of the grains we noted that the normalized fast wave velocity is less than 1, whereas the normalized slow wave velocity behaves in the opposite way.

6. We developed a numerical model for wave propagation from which we derived the reflection and transmission coefficients of plane waves at oblique incidence on an interface between a fluid and a fluid-saturated porous medium. Clear angular dependence and critical angle phenomena were produced for all three wave types. The results were also used to calculate the total transmission coefficients through a layer of porous medium with fluid on either side.
7. Low frequency oscillating pressure gradients were used for the experimental verification of the dynamic permeability model. Results for artificial porous samples demonstrated that the ratio of dynamic over steady-state permeability can be described adequately by the rollover frequency and a similarity parameter close to 1.
8. High frequency wave experiments confirmed that the Biot theory gives a very accurate description of all three phase speed measurements for both artificial and natural sandstone samples. Moreover the slow compressional wave was detected in a natural water-saturated sandstone (Nivelsteiner sandstone) for the first time.
9. The Biot theory predicted excellent the measured attenuation of the slow wave in the fused glass bead sample. For all other samples, the measured slow wave attenuation was underestimated only slightly. However, the theory failed to predict the fast wave and shear wave attenuation, especially in natural sandstones. This discrepancy is probably due to the absence of scattering, micro-cracks and clay effects in the theoretical model.
10. In the unconsolidated Nivelsteiner sandstone samples we found higher attenuation values than in the consolidated samples. A scattering mechanism related to the contrast between the grain and matrix bulk moduli K_s/K_b and K_s/G may have caused this additional attenuation in the unconsolidated samples.

Appendix A

De Vries-Geerits approach for non-viscous fluid

Geerits recently published a macroscopic theory for wave propagation through fluid-saturated porous media (Geerits, 1996). The results are closely linked to work by De Vries (1989), who originally started to investigate the scope of a linear acoustic theory for impulsive wave propagation in a porous medium with the aid of a spatial volume averaging technique. To this end, the microscopic field equations of a non-viscous fluid and a perfectly elastic solid were spatially averaged over a representative elementary domain of the fluid-solid composite. In this appendix we will briefly review the derivation of the macroscopic field equations of the original theory proposed by De Vries and discuss the similarity of the resulting equations to the Biot equations. In the following, the formulation of De Vries and Geerits will be referred to as the DVG approach.

In the DVG approach, a non-viscous fluid is considered. The basic idea behind the averaging technique is the following. Assume that on the scale of the geometry of the pores, the continuum equations for perfectly elastic solids and non-viscous fluids hold. These microscopic continuum equations are then spatially averaged over a representative elementary domain of the fluid-solid composite. The size of this representative elementary domain should be both sufficiently small and sufficiently large, such that both the macroscopic and the microscopic inhomogeneities will not affect the results of the averaging procedure. After this averaging procedure and some fundamental assumptions about the coupling between fluid and solid field quantities, we end up with the basic equations which describe the acoustic wave

motion in a porous medium on a macroscopic scale.

The description of this DVG model starts with the momentum equations and stress-strain relations (i.e. the constitutive equations for deformation rate behaviour) for the constituents of the fluid-saturated porous medium, a non-viscous fluid and a perfectly elastic solid, respectively. For the equations of motion we have

$$\partial_i \sigma - \rho_f \partial_t v_i^f = 0, \quad (\text{A.1})$$

$$\partial_i \tau_{ij}^s - \rho_s \partial_t v_j^s = 0. \quad (\text{A.2})$$

Here the superscripts f and s denote the non-viscous fluid and the perfectly elastic solid, respectively. Furthermore, σ is the omnidirectional fluid traction, which is the exact opposite of the fluid pressure, τ_{ij}^s is the solid stress tensor, \mathbf{v}^f and \mathbf{v}^s are the particle velocities of both phases, and ρ_f and ρ_s are the densities. For the stress-strain relations we have

$$\partial_t \sigma - K_f \partial_k v_k^f = 0, \quad (\text{A.3})$$

$$\partial_t \tau_{ij}^s - C_{ijrs} \dot{e}_{rs} = 0, \quad (\text{A.4})$$

where K_f is the fluid bulk modulus, C_{ijrs} the solid stiffness tensor, and \dot{e}_{rs} the time derivative of the solid strain tensor defined by

$$\dot{e}_{rs} = 1/2(\partial_s v_r^s + \partial_r v_s^s). \quad (\text{A.5})$$

Next, the macroscopic equations for a porous medium follow from a procedure of spatial averaging applied to the local solid and fluid quantities over a so-called representative elementary domain D , as depicted in Figure (2.1). For this, we distinguish two types of field quantities on a microscopic scale in the porous medium: one for the fluid phase, $\psi^f(\mathbf{x}, t)$, and one for the solid phase, $\psi^s(\mathbf{x}, t)$. In the spatial averaging theorems two kinds of averages show up. The first type are averages over the total volume V of the representative elementary spatial domain (denoted as total volume averages).

$$\langle \psi^{f,s} \rangle(\mathbf{x}, t) = \frac{1}{V} \int_{\mathbf{x}' \in D^{f,s}(\mathbf{x})} \psi^{f,s}(\mathbf{x}', t) dV \quad (\text{A.6})$$

where D^f is the subdomain of D where the fluid is present, and D^s the subdomain of D where the solid is present. The second type are averages over the volume of the single phases (denoted as intrinsic volume averages)

$$\langle \psi^{f,s} \rangle^{f,s}(\mathbf{x}, t) = \frac{1}{V^{f,s}} \int_{\mathbf{x}' \in D^{f,s}(\mathbf{x})} \psi^{f,s}(\mathbf{x}', t) dV \quad (\text{A.7})$$

where V^f and V^s are the volumes of the fluid and solid contained in the total volume V . Obviously, in Equations (A.6) and (A.7), the quantities $\langle \psi^f \rangle$ and $\langle \psi^s \rangle$ are total volume averages and $\langle \psi^f \rangle^f$ and $\langle \psi^s \rangle^s$ are intrinsic volume averages. In the DVG theory, the concept of total volume-averaging for all relevant field quantities was chosen. Biot defined the macroscopic particle displacements (and velocities) as intrinsically volume-averaged, and the macroscopic acoustic pressure and stresses as totally volume-averaged. From these definitions it then becomes clear that the relationship between these two types of volume averages follows from the straightforward definition of the volume fractions (porosity)

$$\phi^{f,s}(\mathbf{x}) = \frac{V^{f,s}(\mathbf{x})}{V} \quad (\text{A.8})$$

occupied by the fluid and solid, respectively. From Equation (A.8) it follows that

$$\langle \psi^f \rangle(\mathbf{x}, t) = \phi^f(\mathbf{x}) \langle \psi^f \rangle^f(\mathbf{x}, t) \quad (\text{A.9})$$

for a fluid-phase quantity and

$$\langle \psi^s \rangle(\mathbf{x}, t) = \phi^s(\mathbf{x}) \langle \psi^s \rangle^s(\mathbf{x}, t) \quad (\text{A.10})$$

for a solid-phase quantity.

Now, from Equations (A.1)-(A.4), we note that these continuum equations have the shape of partial differential equations. For the macroscopic partial differential equations of the porous medium we need partial derivatives of spatially averaged field quantities (fluid pressure and particle velocity in the fluid phase, stress and particle velocity in the solid phase). This poses the question of how the partial derivatives of a spatially averaged field quantity are related to the spatial average of the partial derivatives of this field quantity. From the volume-averaging theorems it is shown that the difference between the two is a surface interaction integral over the microscopic fluid/solid interface. The relevant relations are found to be

$$\langle \partial_i \psi^{f,s} \rangle(\mathbf{x}, t) = \partial_i \langle \psi^{f,s} \rangle(\mathbf{x}, t) + \frac{1}{V} \int_{\mathbf{x}' \in \Sigma(\mathbf{x})} v_i^{f,s} \psi^{f,s}(\mathbf{x}', t) dA \quad (\text{A.11})$$

and

$$\langle \partial_t \psi^{f,s} \rangle(\mathbf{x}, t) = \partial_t \langle \psi^{f,s} \rangle(\mathbf{x}, t) \quad (\text{A.12})$$

Note that $\Sigma(\mathbf{x})$ denotes the interface between the fluid and solid as far as this is located in the interior of the representative elementary domain D . Furthermore, v_i^f and v_i^s are the unit vectors along the normal to $\Sigma(\mathbf{x})$ pointing away from the respective phases.

If we now return to the surface interaction integrals of Equation (A.11), we note that the only fundamental assumption of the DVG theory is that this interaction term is linearly related to the volume averaged acoustic state quantities of the phases involved. For example, if we start the averaging procedure by applying the volume averaging operator as defined in Equation (A.6) to the equation of motion for a perfectly elastic solid (cf. Eq. (A.2)), and use the averaging properties in Equations (A.11) and (A.12) we obtain

$$\partial_i \langle \tau_{ij}^s \rangle(\mathbf{x}, t) - \rho_s \partial_t \langle v_j^s \rangle = \frac{1}{V} \int_{\mathbf{x}' \in \Sigma(\mathbf{x})} v_i^s \tau_{ij}^s(\mathbf{x}', t) dA \quad (\text{A.13})$$

The surface interaction integral in Equation (A.13) represents the total time rate of momentum transfer via $\Sigma(\mathbf{x})$, by which the fluid and solid phase are coupled. We now make the physically plausible assumption that the time rate of net momentum transfer through $\Sigma(\mathbf{x})$ is proportional to the total volume-averaged particle accelerations of the fluid and solid phases. Therefore, we may write

$$\frac{1}{V} \int_{\mathbf{x}' \in \Sigma(\mathbf{x})} v_i^s \tau_{ij}^s(\mathbf{x}', t) dA = m_{ij}^{fs} \partial_t \langle v_i^s \rangle - m_{ij}^{sf} \partial_t \langle v_i^f \rangle \quad (\text{A.14})$$

where

$$m_{ij}^{fs}, m_{ij}^{sf} = \text{mutually-induced tensorial volume densities of mass (kg/m}^3\text{)}.$$

This kind of reasoning can be used for all surface interaction integrals of the relevant field quantities which show up after applying the averaging theorems to the basic equations of the constituents of the porous medium (cf. Eqs. (A.1)-(A.4)). This will finally lead to a system of basic equations which can be used to describe the acoustic wave motion in a porous medium on a macroscopic scale. Upon following this procedure the homogeneous, isotropic poro-elastic momentum equations in absence of source terms follow as

$$\partial_i \langle \sigma \rangle = m^{ff} \partial_t \langle v_i^f \rangle + m^{fs} \partial_t \langle v_i^s \rangle, \quad (\text{A.15})$$

$$\partial_j \langle \tau_{ji}^s \rangle = m^{ss} \partial_t \langle v_i^s \rangle - m^{sf} \partial_t \langle v_i^f \rangle, \quad (\text{A.16})$$

for the fluid part and the solid part of the porous medium, respectively, in which

$$\begin{aligned} \langle \tau_{ji}^s \rangle &= \text{macroscopic solid stress tensor (Pa),} \\ \langle \sigma \rangle &= \text{omnidirectional macroscopic fluid traction (Pa),} \\ \langle v_i^s \rangle &= \text{macroscopic solid particle velocity (m/s),} \\ \langle v_i^f \rangle &= \text{macroscopic fluid particle velocity (m/s),} \end{aligned}$$

and where

$$m^{ff} = \rho_f - m^{sf} \quad (\text{A.17})$$

is the self-induced scalar fluid volume density of mass (kg/m^3), and

$$m^{ss} = \rho_s - m^{fs} \quad (\text{A.18})$$

is the self-induced scalar solid volume density of mass (kg/m^3). For the stress-strain relations of the fluid part and the solid part we obtain, respectively,

$$\partial_i \langle v_i^f \rangle = \kappa^{ff} \partial_t \langle \sigma \rangle + \frac{1}{3} \kappa^{fs} \partial_t \langle \tau_{kk}^s \rangle, \quad (\text{A.19})$$

$$\frac{1}{2} \left[\partial_j \langle v_i^s \rangle + \partial_i \langle v_j^s \rangle \right] = \kappa_{ijpq}^{ss} \partial_t \langle \tau_{pq}^s \rangle + \frac{1}{3} \delta_{ij} \kappa^{sf} \partial_t \langle \sigma \rangle, \quad (\text{A.20})$$

where

$$\kappa^{ff} = \kappa_f - \kappa^{fs} \quad (\text{A.21})$$

is the self-induced scalar fluid compressibility (Pa^{-1}), with κ_f the fluid compressibility. The rank four tensor κ_{ijpq}^{ss} is the self-induced solid compressibility (Pa^{-1}). For an isotropic porous medium, this becomes

$$\kappa_{ijpq}^{ss} \partial_t \langle \tau_{pq}^s \rangle = \Lambda^{ss} \delta_{ij} \partial_t \langle \tau_{kk}^s \rangle + 2M^{ss} \partial_t \langle \tau_{ij}^s \rangle, \quad (\text{A.22})$$

where M^{ss} and Λ^{ss} are Lamé-like compressibility coefficients and in which use has been made of the definition

$$\kappa_{iipp}^{ss} = \kappa^{ss} = 9\Lambda^{ss} + 6M^{ss}. \quad (\text{A.23})$$

Next, we will discuss the similarity between these macroscopic field equations and the Biot equations in terms of the coupling coefficients defined in both theories.

A.1 Similarity to Biot formulation

In the Biot theory, the fluid and solid velocities \mathbf{w} and \mathbf{v} are intrinsic variables, which means that the averaging takes place over the corresponding phase, and not over the bulk volume V . This means that $\langle \mathbf{v}^f \rangle = \phi \mathbf{w}$ and $\langle \mathbf{v}^s \rangle = (1 - \phi) \mathbf{v}$, where ϕ denotes the fluid volume fraction, usually called the porosity. For both the Biot theory and the DVG theory, the macroscopic fluid traction and solid stress are total volume-averaged variables. This means that $\partial_t \langle \sigma \rangle = \partial_t \tau$, and that $\partial_t \langle \tau_{kk}^s \rangle = \partial_t \tau_{kk}$. With this in mind, the momentum equations for the DVG theory can be rewritten as

$$\partial_i \tau = \phi m^{ff} \partial_t w_i + (1 - \phi) m^{fs} \partial_t v_i, \quad (\text{A.24})$$

$$\partial_j \tau_{ji} = (1 - \phi) m^{ss} \partial_t v_i + \phi m^{sf} \partial_t w_i. \quad (\text{A.25})$$

The momentum equations according to Biot for a non-viscous fluid follow as

$$\partial_i \tau = \rho_{22} \partial_t w_i + \rho_{12} \partial_t v_i, \quad (\text{A.26})$$

$$\partial_j \tau_{ji} = \rho_{11} \partial_t v_i + \rho_{12} \partial_t w_i. \quad (\text{A.27})$$

From Equations (A.24)-(A.27) it can easily be seen that

$$m^{ff} = \frac{\rho_{22}}{\phi}, \quad (\text{A.28a})$$

$$m^{fs} = \frac{\rho_{12}}{(1 - \phi)}, \quad (\text{A.28b})$$

$$m^{ss} = \frac{\rho_{11}}{(1 - \phi)}, \quad (\text{A.28c})$$

$$m^{sf} = \frac{\rho_{12}}{\phi}. \quad (\text{A.28d})$$

Next, the stress-strain relations for the DVG theory can be rewritten as

$$\phi \partial_i w_i = \kappa^{ff} \partial_t \tau + \frac{1}{3} \kappa^{fs} \partial_t \tau_{kk}, \quad (\text{A.29})$$

$$\frac{(1 - \phi)}{2} [\partial_j v_i + \partial_i v_j] = \kappa_{ijpq}^{ss} \partial_t \tau_{pq} + \frac{1}{3} \delta_{ij} \kappa^{sf} \partial_t \tau. \quad (\text{A.30})$$

The stress-strain relations according to Biot follow from Equations (2.11) and (2.12) as

$$\partial_t \tau = Q \partial_t e_{kk} + R \partial_t \varepsilon_{kk}, \quad (\text{A.31})$$

$$\partial_t \tau_{ij} = 2G \partial_t e_{ij} + A \partial_t e_{kk} \delta_{ij} + Q \partial_t \varepsilon_{kk} \delta_{ij}. \quad (\text{A.32})$$

From Equations (A.32) and (A.31) it can be derived that

$$\partial_t \varepsilon_{kk} = \frac{D}{DR - Q^2} \partial_t \tau - \frac{1}{3} \frac{Q}{DR - Q^2} \partial_t \tau_{kk}, \quad (\text{A.33})$$

where $3D = 2G + 3A$. Relation (A.33) can now be compared with Equation (A.29), where we notice that the LHS of (A.29) equals $\phi \partial_t \varepsilon_{kk}$. It then follows that

$$\kappa^{ff} = \frac{D\phi}{DR - Q^2}, \quad (\text{A.34a})$$

$$\kappa^{fs} = \frac{-Q\phi}{DR - Q^2}. \quad (\text{A.34b})$$

From Equations (A.32) and (A.31) it can also be derived that

$$2G \partial_t e_{ij} = \partial_t \tau_{ij} - \frac{Q(D - A)}{DR - Q^2} \delta_{ij} \partial_t \tau - \frac{1}{3} \frac{AR - Q^2}{DR - Q^2} \delta_{ij} \partial_t \tau_{kk}. \quad (\text{A.35})$$

Using Equation (A.22), Equation (A.35) can now be compared with Equation (A.30), where again we notice that the LHS of (A.30) equals $(1 - \phi) \partial_t e_{ij}$. It then follows that

$$2M^{ss} = \frac{(1 - \phi)}{2G}, \quad (\text{A.36a})$$

$$3\Lambda^{ss} = \frac{1}{3} \frac{R(1 - \phi)}{DR - Q^2} - \frac{(1 - \phi)}{2G}, \quad (\text{A.36b})$$

$$\kappa^{sf} = \frac{-Q(1 - \phi)}{DR - Q^2}. \quad (\text{A.36c})$$

A.2 Energy considerations

To continue our comparison of the Biot formulation with the DVG formulation, we investigate the exchange of acoustic energy between a certain portion of the porous medium and its surroundings. Multiplying Equations (A.24)-(A.25) and (A.29)-(A.30) by the macroscopic field quantities $-w_i$, $-v_i$, $-\tau$, and τ_{ij} , respectively, and adding the resulting equations we obtain

$$\dot{E}_{kin} + \dot{E}_{def} + \partial_i S_i = 0, \quad (\text{A.37})$$

in which

$$\begin{aligned} \dot{E}_{kin} = & \phi m^{ff} w_i \partial_t w_i + (1 - \phi) m^{fs} w_i \partial_t v_i \\ & + \phi m^{sf} v_i \partial_t w_i + (1 - \phi) m^{ss} v_i \partial_t v_i, \end{aligned} \quad (\text{A.38})$$

denotes the volume density of the time derivative of kinetic energy (SI-unit: $\text{J}/\text{m}^3\text{s}$),

$$\begin{aligned} \dot{E}_{def} = & \frac{\kappa^{ff}}{\phi} \tau \partial_t \tau + \frac{\kappa^{fs}}{\phi} \tau \partial_t \frac{\tau_{kk}}{3} + \frac{\kappa^{sf}}{(1 - \phi)} \frac{\tau_{kk}}{3} \partial_t \tau \\ & + \frac{\Lambda^{ss}}{(1 - \phi)} \tau_{ii} \partial_t \tau_{pp} + \frac{2M^{ss}}{(1 - \phi)} \tau_{pq} \partial_t \tau_{pq}, \end{aligned} \quad (\text{A.39})$$

the volume density of the time derivative of deformation energy (SI-unit: $\text{J}/\text{m}^3\text{s}$), and

$$S_i = -w_i \tau - v_j \tau_{ij} \quad (\text{A.40})$$

denotes the area density of acoustic power flow (acoustic Poynting vector: SI-unit: $\text{W}/\text{m}^3\text{s}$). Equation (A.37) is the local form of the acoustic power balance in a porous medium.

Next, we mention the condition under which the volume density of the time derivative of deformation energy, cf. Equation (A.39), can be written as a time derivative of the deformation energy density, where the latter is a state quantity, i.e. a quantity that only depends on the instantaneous values of the macroscopic fluid traction and the macroscopic solid stress. The relevant condition is

$$\frac{\kappa^{fs}}{\phi} = \frac{\kappa^{sf}}{1 - \phi}. \quad (\text{A.41})$$

In this way Equation (A.39) can be rewritten as

$$\dot{E}_{def} = \partial_t E_{def}, \quad (\text{A.42})$$

in which

$$E_{def} = \frac{\kappa^{ff}}{2\phi} \tau \tau + \frac{\kappa^{fs} \kappa^{sf}}{\phi(1 - \phi)} \tau \frac{\tau_{kk}}{3} + \frac{\Lambda^{ss}}{2(1 - \phi)} \tau_{ii} \tau_{pp} + \frac{M^{ss}}{(1 - \phi)} \tau_{pq} \tau_{pq}, \quad (\text{A.43})$$

where E_{def} denotes the volume density of the deformation energy (SI-unit: J/m^3).

Equations (A.34) and (A.36) give the relationships between the DVG coefficients and the Biot coefficients. The Biot coefficients in terms of measurable quantities are mentioned in Equations (2.36) and (2.37). To prove that both theories are completely identical, it is necessary to investigate the DVG definitions for consistency with the Biot theory. Starting with condition (A.41), we notice from Equations (A.34b) and (A.36c) that this condition also holds for the Biot coefficients. Furthermore, it turns out that the DVG definitions for κ^{ff} (cf. Equation A.21) and κ^{ss} (cf. Equation A.23) are also applicable to the Biot theory. This can be shown after substituting Equations (A.34) and (A.36), and using the relationships between the elastic coefficients and the measurable quantities formulated in Equation (2.36). For the case of incompressible grains, cf. Equation (2.37), the DVG definition of κ^{ss} results in $1/\kappa^s = 0$. Obviously, Equation (2.37) is based on this assumption.

Similarly, we mention the condition under which the volume density of the time derivative of kinetic energy, cf. Equation (A.38) can be written as the time derivative of the kinetic energy density, where the latter is a state quantity, i.e. a quantity that only depends on the instantaneous values of the macroscopic fluid and solid velocities. The relevant condition is

$$\phi m^{sf} = (1 - \phi) m^{fs}. \quad (\text{A.44})$$

In this way Equation (A.38) can be rewritten as

$$\dot{E}_{kin} = \partial_t E_{kin}, \quad (\text{A.45})$$

in which

$$E_{kin} = \frac{\phi}{2} m^{ff} w_i w_i + \phi(1 - \phi) m^{sf} m^{fs} w_i v_i + \frac{(1 - \phi)}{2} m^{ss} v_i v_i, \quad (\text{A.46})$$

where E_{kin} denotes the volume density of the kinetic energy (SI-unit: J/m³).

Equation (A.28) gives the relationships between the DVG coefficients and the Biot coefficients. The Biot coefficients in terms of measurable quantities are mentioned in Equations (2.40)-(2.42). Again, to demonstrate that the two theories are completely identical, it is necessary to investigate the DVG definitions for consistency with the Biot theory. Starting with condition (A.44), we note from Equations (A.28b) and (A.28d) that this condition also holds for the Biot coefficients. Finally, it turns out that the DVG definitions for m^{ff} (cf. Equation A.17) and m^{ss} (cf. Equation A.18) are also

applicable to the Biot theory. This can be shown after substituting Equation (A.28), and using the relationships between the density coefficients and the measurable quantities, formulated in Equations (2.40)-(2.42).

Bibliography

- K. Aki and P.G. Richards. *Quantitative Seismology*, volume 1. W.H. Freeman and Company, 1980.
- J.F. Allard. *Propagation of sound in porous media: Modelling sound absorbing materials*. Elsevier, 1993.
- A.J. Berkhout. *Applied Seismic Wave Theory*, volume 1 of *Advances in Exploration Geophysics 1*. Elsevier, Amsterdam, 1987.
- J.G. Berryman. Confirmation of biot's theory. *Appl. Phys. Lett.*, 37:382-384, 1980.
- J.G. Berryman. Elastic wave propagation in fluid-saturated porous media. *J. Acoust. Soc. Am.*, 69:416-424, 1981.
- M.A. Biot. General theory of three-dimensional consolidation. *J. Appl. Phys.*, 12:155-164, 1941.
- M.A. Biot. Theory of elasticity and consolidation for a porous anisotropic solid. *J. Appl. Phys.*, 61:182-185, 1955.
- M.A. Biot. Theory of propagation of elastic waves in a fluid-saturated solid. I. Low frequency range. *J. Acoust. Soc. Am.*, 28:168-178, 1956a.
- M.A. Biot. Theory of propagation of elastic waves in a fluid-saturated solid. II. Higher frequency range. *J. Acoust. Soc. Am.*, 28:179-191, 1956b.
- M.A. Biot. Generalized theory of acoustic propagation in porous dissipative media. *J. Acoust. Soc. Am.*, 34:1254-1264, 1962.
- M.A. Biot and Willis. The elastic coefficients of the theory of consolidation. *J. Appl. Mech.*, 24:594-601, 1957.

- F.A. Boyle and H.P. Chotiros. Experimental detection of a slow acoustic wave in sediment at shallow grazing angles. *J. Acoust. Soc. Am.*, 91: 2615-2619, 1992.
- R.J.S. Brown. Connection between formation factor for electrical resistivity and fluid-solid coupling factor in Biot's equation for acoustic waves in fluid-filled porous media. *Geophysics*, 45:1269-1275, 1980.
- R.J.S. Brown and J. Korringa. On the dependence of the elastic properties of a porous rock on the compressibility of the pore fluid. *Geophysics*, 40: 608-616, 1975.
- R. Burridge and J.B. Keller. Poroelasticity equations derived from microstructure. *J. Acoust. Soc. Am.*, 70:1140-1146, 1981.
- R.N. Chandler. Transient streaming potential measurements on fluid-saturated porous structures: An experimental verification of biot's slow wave in the quasi-static limit. *J. Acoust. Soc. Am.*, 70:116-121, 1981.
- R.N. Chandler and D.L. Johnson. The equivalence of quasistatic flow in fluid-saturated porous media and biot's slow wave in the limit of zero frequency. *J. Appl. Phys.*, 52:3391-3395, 1981.
- A.M. Chapman and J.J.L. Higdon. Oscillatory stokes flow in periodic porous media. *Phys. Fluids A*, 4:2099-2116, 1992.
- E. Charlaix, A.P. Kushnick, and J.P. Stokes. Experimental study of dynamic permeability in porous media. *Phys. Rev. Lett*, 61:1595-1598, 1988.
- R.C.Y. Chin, J.G. Berryman, and G.W. Hedstrom. Generalized ray expansion for pulse propagation and attenuation in fluid-saturated porous media. *Wave Motion*, 7:43-65, 1985.
- L. De Gijzel. *Modelling of acoustic wave propagation in porous media: theory and experiments*. MSc thesis, Delft University of Technology, 1996.
- C. De Josselin de Jong. What happens in soil during pile driving? *De Ingenieur*, 68:B77-B88, 1956.
- S.M. De Vries. *Propagation of transient acoustic waves in porous media*. PhD thesis, Delft University of Technology, 1989.

- H. Deresiewicz. The effect of boundaries on wave propagation in a liquid-filled porous solid: I. Reflection of plane waves at a free plane boundary (non-dissipative case). *Bull. Seism. Soc. Am.*, 50:599-607, 1960.
- H. Deresiewicz and A. Levy. The effect of boundaries on wave propagation in a liquid-filled porous solid: X. Transmission through a stratified medium. *Bull. Seism. Soc. Am.*, 57:381-392, 1967.
- H. Deresiewicz and J.T. Rice. The effect of boundaries on wave propagation in a liquid-filled porous solid: III. Reflection of plane waves at a free plane boundary (general case). *Bull. Seism. Soc. Am.*, 52:595-625, 1962.
- H. Deresiewicz and R. Skalak. On uniqueness in dynamic poroelasticity. *Bull. Seism. Soc. Am.*, 53:783-788, 1963.
- F. Gassmann. Elastic waves through a packing of spheres. *Geophysics*, 16: 673-685, 1951.
- T.W. Geerits. Acoustic wave propagation through porous media, revisited. *J. Acoust. Soc. Am.*, 100:2949-2959, 1996.
- T.W. Geerits and O. Kelder. Acoustic wave propagation through porous media: Theory and experiments. *J. Acoust. Soc. Am.*, 102:2495-2510, 1997.
- T. Geertsma and D.C. Smit. Some aspects of elastic wave propagation in fluid-saturated porous solids. *Geophysics*, 26:169-181, 1961.
- G.A. Gist. Fluid effects on velocity and attenuation in sandstones. *J. Acoust. Soc. Am.*, 96:1158-1173, 1994.
- S. Hajra and A. Mukhopadhyay. Reflection and refraction of seismic waves incident obliquely at the boundary of a liquid-saturated porous solid. *Bull. Seismol. Soc. Am.*, 72:1509-1533, 1982.
- J.M. Hovem and G.D. Ingram. Viscous attenuation of sound in saturated sand. *J. Acoust. Soc. Am.*, 66:1807-1812, 1979.
- H.B.E. Hylkema. *The wavefield of a planar circular radiator*. MSc thesis, Delft University of Technology, 1996.
- D.L. Johnson. *Recent developments in the acoustic properties of porous media*, in *Frontiers of Physical Acoustics*, International School of Physics

- 'Enrico Fermi', edited by D. Sette. North Holland Publishing Company, Amsterdam, 1986.
- D.L. Johnson, D.L. Hemmick, and H. Kojima. Probing porous media with first and second sound. I. Dynamic permeability. *J. Appl. Phys.*, 76:104-114, 1994.
- D.L. Johnson, J. Koplik, and R. Dashen. Theory of dynamic permeability and tortuosity in fluid-saturated porous media. *J. Fluid Mech.*, 176:379-402, 1987.
- D.L. Johnson and T.J. Plona. Acoustic slow waves and the consolidation transition. *J. Acoust. Soc. Am.*, 72:556-565, 1982.
- D.L. Johnson, T.J. Plona, and H. Kojima. Probing porous media with first and second sound. II. Acoustic properties of water-saturated porous media. *J. Appl. Phys.*, 76:115-125, 1994.
- D.L. Johnson, T.J. Plona, C. Scala, F. Pasierb, and H. Kojima. Tortuosity and acoustic slow waves. *Phys. Rev. Lett.*, 49:1840-1844, 1982.
- D.H. Johnston, M.N. Toksöz, and A. Timur. Attenuation of seismic waves in dry and saturated rocks: I Mechanics. *Geophysics*, 44:691-711, 1979.
- O. Kelder and D.M.J. Smeulders. Propagation and damping of compressional waves in porous rocks: Theory and experiments. In *Expanded Abstracts, 65th SEG Ann. Mtg.*, pages 675-678, Houston TX, USA, 1995.
- O. Kelder and D.M.J. Smeulders. Measurement of ultrasonic bulk properties of water-saturated porous media. In *Extended Abstracts, 58th EAGE Mtg.*, page C025, Amsterdam, 1996a.
- O. Kelder and D.M.J. Smeulders. New experimental data of dynamic permeability in water-saturated porous media. In *SEG/EAGE Summer Research Workshop, Wave Propagation in Rocks*, Big Sky MT, USA, 1996b.
- O. Kelder and D.M.J. Smeulders. Observation of the Biot slow compressional wave in water-saturated Nivelsteiner sandstone. *Geophysics*, 62: 1794-1796, 1997.
- E. Kemper. *Geologischer führer durch die Grafschaft Bentheim und die angrenzenden gebiete*. Nordhorn-Bentheim, Bentheim, Germany, 1976.

- T. Klimentos and C. McCann. Why is the Biot slow compressional wave not observed in real rocks? *Geophysics*, 53:1605–1609, 1988.
- O.S. Kuyl. Pure Miocene quartz sands in Southern Limburg, The Netherlands, stratigraphical occurrence and regional distribution. *Verh. Kon. Ned. Geol. Mijnbouwk. Gen.*, 29:73–80, 1973.
- A.E.H. Love. *A treatise on the mathematical theory of elasticity*. Dover Publications, New York, 1944.
- W.F. Murphy, K.W. Winkler, and R.L. Kleinberg. Acoustic relaxation in sedimentary rocks: Dependence on grain contacts and fluid saturation. *Geophysics*, 51:757–766, 1986.
- P.B. Nagy, L. Adler, and B.P. Bonner. Slow wave propagation in air-filled porous materials and natural rocks. *Appl. Phys. Lett.*, 56:2504–2506, 1990.
- R.J. O'Connell and B. Budiansky. Viscoelastic properties of fluid-saturated cracked solids. *J. Geophys. Res.*, 82:5719–5735, 1977.
- T.J. Plona. Observation of a second bulk compressional wave in a porous medium at ultrasonic frequencies. *Appl. Phys. Lett.*, 36:259–261, 1980.
- T.J. Plona and K.W. Winkler. Scattering of fast and slow compressional waves in fluid saturated porous media. In proceedings of *Multiple scattering of waves in random media and random rough surfaces*, pages 341–356. The Pennsylvania State University, 1985.
- S.R. Pride, A.F. Gangi, and F.D. Morgan. Deriving the equations of motion for porous isotropic media. *J. Acoust. Soc. Am.*, 6:3278–3290, 1992.
- S.R. Pride, F.D. Morgan, and A.F. Gangi. Drag forces of porous-medium acoustics. *Phys. Rev. B*, 47:4964–4978, 1993.
- L. Schwartz and T.J. Plona. Ultrasonic propagation in close-packed disordered suspensions. *J. Appl. Phys.*, 55:3971–3977, 1984.
- F.M. Sears and B.P. Bonner. Ultrasonic attenuation measurements by spectral ratios utilizing signal processing techniques. *Transactions on Geoscience and Remote Sensing*, GE-19:95–99, 1981.
- P. Sheng and M.Y. Zhou. Dynamic permeability in porous media. *Phys. Rev. Lett.*, 61:1591–1594, 1988.

- D.M.J. Smeulders, J.P.M. De la Rosette, and M.E.H. Van Dongen. Waves in partially saturated porous media. *Transport in Porous Media*, 9:25-37, 1992.
- D.M.J. Smeulders, R.L.G.M. Eggels, and M.E.H. Van Dongen. Dynamic permeability: reformulation of theory and new experimental and numerical data. *J. Fluid. Mech.*, 245:211-227, 1992.
- D.M.J. Smeulders, R.R. Van Hassel, M.E.H. Van Dongen, and J.K.M. Jansen. Similarity of sharp-edged porous media. *Int. J. Engng Sci.*, 32: 979-990, 1994.
- R.D. Stoll. *Acoustic waves in saturated sediments*, in *Physics of sound in marine sediments*, pages 19-39, edited by L.D. Hampton. Plenum, New York, 1974.
- M.N. Toksöz, D.H. Johnston, and A. Timur. Attenuation of seismic waves in dry and saturated rocks: I Laboratory measurements. *Geophysics*, 44: 681-690, 1979.
- J.G. Van der Grinten, M.E.H. Van Dongen, and H. Van der Kogel. Strain and pore pressure propagation in a water-saturated porous medium. *J. Appl. Phys.*, 62:4682-4687, 1987.
- A. Verruijt. The theory of consolidation. In proceedings of *NATO Advanced Study Institute on Mechanics of Fluids in Porous Media*, pages 349-368. Nijhoff, 1982.
- S. Whitaker. Flow in porous media I. A technical derivation of Darcy's law. *Transport in Porous Media*, 1:3-25, 1986.
- K.W. Winkler. Frequency dependent ultrasonic properties of high-porosity sandstones. *J. Geophys. Res.*, 88:9493-9499, 1983.
- K.W. Winkler and W.F. Murphy III. *Acoustic velocity and attenuation in porous rocks*, in *Rock Physics and Phase Relations, A Handbook of Physical Constants*. American Geophysical Union, 1995.
- K. Wu, Q. Xue, and L. Adler. Reflection and transmission of elastic waves from a fluid-saturated porous solid boundary. *J. Acoust. Soc. Am.*, 87: 2349-2358, 1990.

- B. Yavari and A. Bedford. The Biot drag and virtual mass coefficient for face centered cubic granular materials. *Int. J. Multiph. Flow*, 16:885–897, 1990.
- F. Yazir. *Dynamic permeability of fluid-saturated porous media: theory and experiments*. MSc thesis, Delft University of Technology, 1995.
- C. Zwikker and C.W. Kosten. *Sound Absorbing Materials*. American Elsevier, New York, 1949.

Samenvatting

Akoestische signalen uit oppervlakteseismiek en boorgatmetingen kunnen worden gebruikt om informatie te verkrijgen over gesteente- en vloeistofeigenschappen. Metingen die een directe indicatie geven van olie of gas worden veel gebruikt maar zijn voornamelijk gebaseerd op empirische relaties tussen de karakteristieken van het golfveld en de gesteenteëigenschappen. In dit proefschrift proberen wij een meer fundamentele basis te leggen voor het afleiden van gesteente- en vloeistofeigenschappen uit akoestische signalen. Hiertoe werd een tweeledige aanpak gebruikt. Ten eerste werden bestaande theoretische beschrijvingen voor de voorplanting van golven in poreuze media beschreven en uitgebreid. Ten tweede werden de berekeningen gebaseerd op deze theoretische formuleringen experimenteel geverifieerd.

Het theoretische gedeelte van dit proefschrift is gebaseerd op de golfpropagatievergelijkingen voor homogeen en isotroop poreus materiaal geformuleerd door Biot (1956, 1962). We toonden aan dat, door middel van continuïteits- en constitutieve vergelijkingen, de gegeneraliseerde elasticiteitscoëfficiënten uit de Biot theorie rechtstreeks gerelateerd kunnen worden aan de porositeit en elasticiteitsmoduli. Met behulp van een alternatieve afleiding voor de gekoppelde bewegingsvergelijkingen uit de Biot theorie werd aangetoond dat bij lage frequenties de visceuze krachten domineren, terwijl bij hoge frequenties traagheidskrachten domineren. De visceuze effecten worden gekarakteriseerd door de stationaire permeabiliteit en de traagheidskrachten door de tortuositeit. Het model voor de dynamische permeabiliteit, geformuleerd door Johnson et al. (1987), beschreef de overgang in het tussenliggende frequentiegebied. De schalingsfunctie voor de dynamische permeabiliteit van een poreus medium hangt alleen af van de zogenaamde omslagfrequentie en de evenredigheidsparameter M . Door middel van modellering toonden we aan dat onder normale condities M min of meer gelijk is aan 1. Oorspronkelijk werd dit ook al gesuggereerd door Johnson et al.

Het oplossen van de Biot vergelijkingen leidt zowel tot een schuifgolf als tot een snelle en een langzame drukgolf. Bij de snelle drukgolf bewegen de porievloeistof en de matrix in fase en bij de langzame drukgolf uit fase. Dit uit-fase gedrag verklaart de grote demping van de langzame drukgolf. Waar de snelheid van de langzame drukgolf nog wordt beïnvloed door de frequentieafhankelijke dynamische permeabiliteit, zijn de snelheden van de schuifgolf en de snelle drukgolf frequentieonafhankelijk. De invloed van de dynamische permeabiliteit op de demping voor alledrie de bulkgolven wordt significant bij hoge frequenties. Klaarblijkelijk vertoont de dynamische permeabiliteit bij lage frequenties een gedrag identiek aan de stationaire permeabiliteit. Het effect van de korrelcompressibiliteit op de drukgolfsnelheden in de hoge frequentielimiet werd ook onderzocht. Het bleek dat voor relevante verhoudingen tussen korrel- en matrixmoduli, de snelheden van de twee drukgolven, genormaliseerd met de corresponderende snelheden voor incompressibele korrels, minder dan 10% varieerden. Tenslotte hebben we de frequentieafhankelijke reflectie- en transmissiecoëfficiënten van vlakke golven, invallend op een grensvlak tussen een vloeistof en een vloeistof-verzadigd poreus medium, bepaald. Voor alledrie de golftypen werden duidelijke hoekafhankelijkheden en kritische hoekarakteristieken waargenomen.

Voor het experimenteel verifiëren van deze theoretische beschouwingen hebben we twee laboratoriumopstellingen gebruikt. Voorts hebben we gebruik gemaakt van verscheidene exemplaren van kunstmatig en natuurlijk poreus materiaal. Alle inputparameters die nodig zijn voor het voorspellen van de metingen zijn voor alle exemplaren apart en onafhankelijk van elkaar bepaald. De eerste opstelling is speciaal ontworpen voor het meten van de dynamische permeabiliteit. In deze zogenaamde Darcy Cel genereren en meten we de transmissie van laagfrequente oscillerende drukgradiënten (20-200 Hz) door een star bevestigd poreuze kolom. Aan een kant van deze kolom bevindt zich een trilpot en aan beide kanten van de kolom zijn drukopnemers gemonteerd. Alle resultaten toonden aan dat de verhouding tussen de dynamische en stationaire permeabiliteit correct beschreven kan worden door de omslagfrequentie en een evenredigheidsparameter ongeveer gelijk aan 1. In de tweede opstelling werden ultrasone (0.1-1 MHz) golftransmissie-experimenten uitgevoerd met behulp van piëzo-elektrische transducenten. De transducenten bevinden zich aan beide kanten van een in water ondergedompelde schijf van poreus materiaal. Voor schijven van zowel de kunstmatige als de natuurlijke Nivelsteiner en Bentheimer zandsteen bleek dat de Biot theorie een zeer nauwkeurige voorspelling gaf voor de gemeten snel-

heid van alledrie de bulkgolven. Bovendien hebben we voor het eerst de langzame drukgolf in een natuurlijk materiaal gemeten (Nivelsteiner zandsteen). De Biot theorie gaf verder voor bijna alle zandsteenexemplaren een zo goed als correcte voorspelling van de demping van de langzame drukgolf. De voorspelling van de demping van de schuifgolf en de snelle drukgolf was echter incorrect. Deze afwijking tussen gemeten demping en de Biot voorspelling werd waarschijnlijk veroorzaakt door verstrooiing, microscheuren, en klei-gerelateerde demping. Verder stelden we in de ongeconsolideerde Nivelsteiner zandsteen exemplaren een grotere demping vast dan in de geconsolideerde exemplaren. Toekomstig onderzoek zou zich moeten concentreren op een kwantitatieve analyse van alle niet-Biot dempingsmechanismen en op de invloed van kleinschalige inhomogeniteiten en dungelaagde media.

Dankwoord

Als afsluiting wil ik in dit dankwoord alle mensen noemen die in belangrijke mate hebben bijgedragen tot de totstandkoming van dit proefschrift.

Mijn grootste dank gaat uit naar David Smeulders. De afgelopen vier jaar heeft hij met veel inzet, betrokkenheid en kritische toetsing de voortgang van het promotie-onderzoek begeleid. Voorts wil ik mijn promotor Max Peeters bedanken voor zijn commentaar en aanwijzingen tijdens het schrijven en afronden van het proefschrift. Met enige trots kan ik vermelden dat ik voor hen beiden de eerste promovendus was die zij hebben begeleid. Bij deze wil ook nog mijn vroegere afstudeerbegeleider Tim Geerits noemen die tijdens de voortgang van het promotie-onderzoek altijd zijn interesse heeft getoond en waardevolle suggesties heeft gedaan.

Tijdens het onderzoek heb ik veel tijd besteed aan het uitvoeren van experimenten. Dit was niet gelukt zonder de inzet en hulpvaardigheid van Karel Heller. Zijn bijdrage aan het experimentele gedeelte van dit proefschrift was onmisbaar. Op dit gebied gaat ook veel dank uit naar Andre Hoving en Jan Etienne. Naast alle ondersteuning die ik van hen alledrie gekregen heb was ook de uitermate gezellige manier van omgang zowel tijdens als buiten werktijden onvergetelijk. Verder wil ik ook Jan Webbink en Ruud Ephraim bedanken voor hun bijdrage aan de experimenten.

Met veel plezier heb ik de afgelopen jaren de dagelijkse begeleiding van de afstudeerders Ferry Yazir, Hidde Hylkema en Luc de Gijzel op mij genomen. Veel experimentele en theoretische resultaten van dit onderzoek zijn mede tot stand gekomen door hun inzet. Hiervoor mijn dank.

Naast onderzoek heeft voetbal altijd een belangrijke plaats in mijn leven ingenomen. Met heel veel plezier denk ik dan ook terug aan de vele pieken en dalen die wij met het Real Dietz voetbalteam (Mark van der Zande, David Smeulders, Marc Hettema, Dirkjan van Dam, Robert van de Ketterij, Simon

Knight, Paul Janssen, Pacelli Zitha en Karl Denys) hebben meegemaakt. Ook wil ik hierbij mijn collega Robert van de Ketterij noemen met wie het delen van een kamer altijd een zeer aparte ervaring is geweest.

Voorts gaat mijn dank uit naar alle leden van de promotiecommissie Prof.ir. M. Peeters, Prof.dr.ir. M.E.H. van Dongen, Prof.dr.ir. A. Verruijt, Prof.dr.ir. J.T. Fokkema, Prof.dr. P.K. Currie en Dr.rer.nat. B.C. Lehr voor hun bereidheid zitting te nemen in de commissie en voor hun commentaar op het conceptproefschrift.

Tenslotte wil ik mijn familie en Anita noemen die altijd vol interesse, steun en trots de promotie hebben gevolgd. Samenleven met Anita was voor mij van groot belang voor het afronden van dit proefschrift. Ondanks haar eigen drukke leven was zij met haar positieve instelling, goede humeur, geduld en vertrouwen een constante bron van inspiratie.

Curriculum vitae

- 10 oktober 1966 Geboren te Uerkheim (Zwitserland)
- 1986 Diploma VWO
Ludger College, Doetinchem
- 1992 Ingenieursdiploma Petroleumwinning (MSc.)
Technische Universiteit Delft
Faculteit Mijnbouwkunde en Petroleumwinning
- 1993-1997 Promotieonderzoek als AIO
Technische Universiteit Delft
Faculteit Technische Aardwetenschappen
Sectie Petrofysica
- heden Petrofysicus
Den norske stats oljeselskap a.s (Statoil)
Stavanger, Noorwegen